NON-TRIVIAL INITIAL STATE ANISOTROPIES AND THEIR EFFECTS ON OBSERVABLES IN THE IP-GLASMA FRAMEWORK

NICOLAS MIRÓ FORTIER

Supervisor: Sangyong Jeon
Department of Physics
McGill University
Montreal, Québec

August 2020

A thesis submitted to McGill University in partial fulfillment of the requirements for the degree of Master of Science

ABSTRACT

IP-Glasma is a QCD-based initial state model for Heavy-Ion Collisions that can reproduce a wide range of observables both on average and in event-by-event distributions when used to initialize hydrodynamic simulations. The model incorporates small-x gluon saturation via the Impact Parameter Dependent Saturation Model (IPSAT) [1] and introduces sub-nucleonic colour charge fluctuations by stochastically sampling the colour charge density for each nucleon, before ultimately evolving the gluon field configuration via a classical Yang-Mills evolution. On the back of its general phenomenological success, this thesis generalizes the 2+1 dimensional IP-Glasma to deformed systems. We attempt to determine how initial state anisotropies affect end-state observables by initializing simulations with deformed nuclei instead of regular spherically symmetric nuclei. The objective is to reproduce the results of the highly successful IP-Glasma model applied to deformed systems [2] and extend them to guide new experimental strides and further constrain the properties of the Quark Gluon Plasma. Comparisons to currently available STAR data [3] will also be presented and discussed, in the hopes of generating enthusiasm around these seldom-chosen collision systems.

RÉSUMÉ

IP-Glasma est un modèle de conditions initiales pour collisions d'ions lourds, basé sur la chromodynamique quantique, capable de décrire un large éventail d?observations, lorsqu'utilisé en combinaison avec une simulation hydrodynamique. Le modèle inclus la saturation des gluons de très basses énergies à l'aide du Modèle de Saturation avec Dépendance au Paramétre d'Impact ("Impact Parameter Dependent Saturation Mode" IPSAT) [1], et introduit des fluctuations de charges subnucléoniques en échantillonnant stochastiquement la densité de charges de couleur de chaque nucléon, pour ensuite évoluer les configurations du champ de gluon à l'aide d'une évolution Yang-Mills classique. En s'appuyant sur son succès phénoménologique, cette thèse généralise le modèle 2+1 dimensionnel IP-Glasma aux systèmes déformés. Nous essaierons de quantifier les effets mesurables d'anisotropies dans l'état initial en initialisant le modèle avec des noyaux atomiques déformés. Les effets mesurables sont déterminés par ce qui est expérimentalement évaluable de nos jours. Notre objectif premier est de reproduire les résultats obtenus á partir du modéle IP-Glasma pour des systèmes déformés [2], ainsi que d'ajouter à ceux-ci en vue de guider des expériences futures et de contraindre á nouveau les différentes propriétés du Plasma de Quark-Gluon. Nous analyserons aussi nos résultats contre les données publiées par la collaboration STAR, au RHIC, en espérant pouvoir générer l'enthousiasme nécessaire autour de ces systèmes de collision rarement employés.

ACKNOWLEDGEMENTS

First and foremost, I would like to thank my advisor, Sangyong Jeon, for his never-ending patience and guidance as I oriented myself in my research and made progress. His patience and dedication to making sure I understood things on a fundamental level have been invaluable to my development as a physicist. I would also like to sincerely thank Charles Gale for answering many of my weekly group meeting questions, and for his unwavering patience.

Special thanks are due to Scott McDonald for innumerable useful discussions and insights as well as his constant willingness to lend a hand where it was needed. Without Scott to develop McGill's version of IP-Glasma and explain it to me, this work would have been much more tiring. Scott deserves much of the credit for this thesis' work. I am unbelievably grateful to have been able to join this research group at a time when he was still a member.

Thanks are also due to Jessica Churchill, Roozbeh Yazdi and Matt Heffernan. Their camaraderie, encouragement, and help, along with their good mood and joy in our office, have made this challenging path a less scary one.

I would also like to thank Mayank Singh for his presence and reassurance when I felt like I would not be capable of accomplishing what needed to be accomplished.

Beyond specifics am grateful to my fellow graduate students in the nuclear theory group at McGill, whose expertise and general friendliness taught me a great deal about how to be a successful graduate student. I am also grateful to many other students in the McGill Physics Department for their support and interest in my work, which often led to progress in this thesis.

Finally, I would like to thank my parents, brothers and sisters (all six of them!), and my girlfriend Gabrielle and my friends outside of physics. You have all heard me talk about my passion - at times, intelligibly while at others, not - so often, and without your love and support through the years, I would not be here.

CONTENTS

LIST OF FIGURES

Part I

INTRODUCTION AND MOTIVATIONS

1

INTRODUCTION

1.1 QUANTUM CHROMODYNAMICS

There are four independent forces that exist in nature; gravitation, electromagnetism, and the weak and strong nuclear forces. Contemporary nuclear physicists collide heavy ions at relativistic speeds to learn about the Quantum Chromodynamics (QCD), a prominent and successful nuclear theory which aims to describe the strong nuclear force.

The strong nuclear force binds particles that carry colour charge together to form hadrons, much in the same way that the electromagnetic force tethers electrons (negatively charged) to nuclei (positively charged). Quarks are the building blocks of hadrons, and are therefore subject to the strong nuclear force, and, therefore, the laws of QCD. A hadron is, at any given time, a sea of quark-antiquark pairs, which is why its valence quarks classify it. Much like valence electrons point to the number of electrons an atom has which are free to interact with other atoms, valence quarks are the quarks which do not form a quark-antiquark pair and are therefore on the outer banks of the quark-antiquark sea, allowing them to interact cohesively with quarks outside of "their" hadron.

Baryons have three valence quarks, and mesons have a valence quark-antiquark pair: these makeup hadrons. There are six different quarks to choose from, which form 3 families of 2 quarks: the up and down quarks, which form stable hadronic matter like protons and neutrons; the charm and strange quarks; and the top and bottom quarks.

Quarks are only part of the story, however. The Standard Model (SM) of particle physics describes forces as being "mediated" (or carried) by particles known as gauge bosons. QCD falls under the SM umbrella, and must, therefore, itself have gauge bosons. These are analogous to the photon in Quantum Electrodynamics (QED). However, because QCD and QED are two different theories, there must exist critical differences

between their respective mediating particles. Instead of being monolithic like the QED photons, there are eight different particles designated as gluons, all acting as QCD gauge bosons. These carry different colour content, which determines which interactions they mediate. Quarks are permeated by both electric and colour charges, which means they can interact via both forces.

Looking at the QCD Lagrangian in equation (1.1), we see that it includes both chromodynamic and electromagnetic quantities:

$$\begin{aligned} \mathcal{L}_{QCD} &= \sum_q \bar{\psi}_{q,a} \left(i\gamma^\mu \partial_\mu \delta_{ab} - g_s \gamma^\mu t^C_{ab} \mathcal{A}^C_\mu - m_q \delta_{ab} - q_q A_\mu \right) \psi_{q,b} \qquad (1.1) \\ &\quad - \frac{1}{4} F^A_{\mu\nu} F^{A\mu\nu} - \frac{1}{4} F_{\mu\nu} F^{\mu\nu} \\ F^A_{\mu\nu} &= \partial_\mu \mathcal{A}^A_\nu - \partial_\nu \mathcal{A}^A_\mu - g_s f_{ABC} \mathcal{A}^B_\mu \mathcal{A}^C_\nu \qquad (1.2) \\ F_{\mu\nu} &= \partial_\mu A_\nu - \partial_\nu A_\mu \qquad (1.3) \end{aligned}$$

Colour indices a, b, gluon indices A, B and C as well as the generators of the SU(3) group, t^i, riddle the $\mathcal{L}_{QCD}$. Each quark has a colour charge state, which a, b label as as red, green and blue. These colour states form a basis in a 3-D vector space, which can then be rotated using 3x3 unitary matrices (the SU(3) matrices). These new indices lead to more intricate and complex solutions than those of QED. Also important to note is the fact that the gluon field strength tensor $F^A_{\mu\nu}$ contains an additional term that represents interactions between colour-charged gluons. We also have $F_{\mu\nu}$ and A_μ, which represent the electromagnetic field strength tensor and gauge field, respectively. Contrarily to photons that cannot interact directly with other photons because of their electric charge neutrality, gluons can interact with other gluons of the right colour charge, as showcased by $g_s f_{ABC} \mathcal{A}^B_\mu \mathcal{A}^C_\nu$. Gluons, consequently, produce considerable colour fields, given their intrinsic colour charge.

QCD's coupling also behaves differently than that of QED. In electromagnetism, the coupling is weak relative to the strong force and increases in strength with increasing energy. However, the strong force is comparatively strong at low energies and decreases in strength at progressively higher energies, which is why it is called *asymptotically free*. Consequently, to apply perturbation theory to QCD calculations, one must move to extremely high energies, as the strong force cannot be treated perturbatively at low ener-

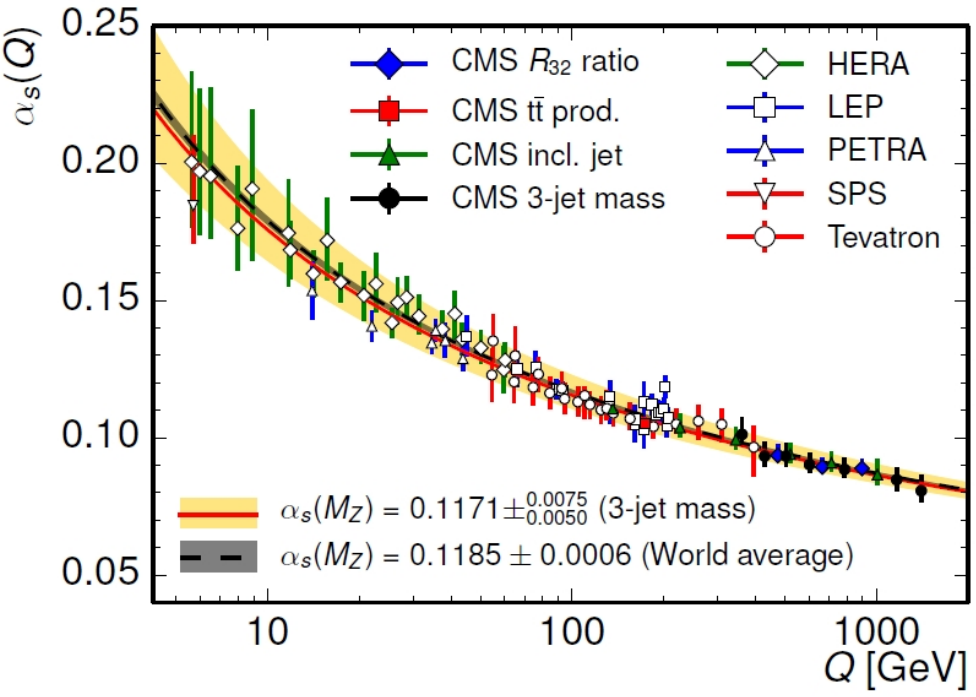

Figure 1: Evolution of the QCD coupling constant with increase in energy, from [4].

gies. Fig. 1 shows the decrease in coupling. Asymptotic freedom, in turn, explains the importance and relevance of heavy-ion collisions (HIC) in studying the strong nuclear force. By moving to such energetic regimes, we can apply QCD perturbatively and make calculations and predictions which are not possible at lower energies.

An essential consequence of asymptotic freedom is *colour confinement*, which dictates that in order to separate two colour charge-carrying particles, one would need more energy than is required to create a new quark-antiquark pair simply. This analogy can be thought of as a set of rubber bands keeping the first pair together. As we would increase the energy input to separate them, more and more bands would be added to solidify the particles' bond. If and when one of these figurative "elastic bands" breaks, a new quark-antiquark spawns from the vacuum. Therefore, it is impossible to measure free colour charged particles under normal conditions (which adds to the importance of HICs).

However, it can be extrapolated that, at high enough energies, these "elastic bands" become irrelevant, leading to the deconfinement of strong matter. This means that, at such energies, the bound states that makeup "ordinary" matter are no more, and de-

confined quarks and gluons are free to roam in a scalding and volatile fluid known as Quark-Gluon Plasma (QGP).

1.2 QGP (AND WHY HEAVY-ION COLLISIONS MATTER)

QCD poses clear challenges to physicists, which have, through the years, developed a myriad of methods for studying strong matter such as Ads/CFT and lattice QCD. However, Heavy-Ion Collisions (HICs) provided a unique path to studying QCD. They are sufficiently energetic to form and probe QGP, offering a window into the rare and exotic world of unbound quarks and gluons. Fig. 2 shows the QCD phase diagram. At low temperature and baryon density are the usual hadrons (represented as a hadronic gas), or "ordinary" matter. As we move to hotter and denser states, we first find deconfinement, then QGP. This thesis's scope will be limited, but one can notice how intricate, complex, and vast the QCD phase diagram is, begging for further investigation of some of its most extreme regions.

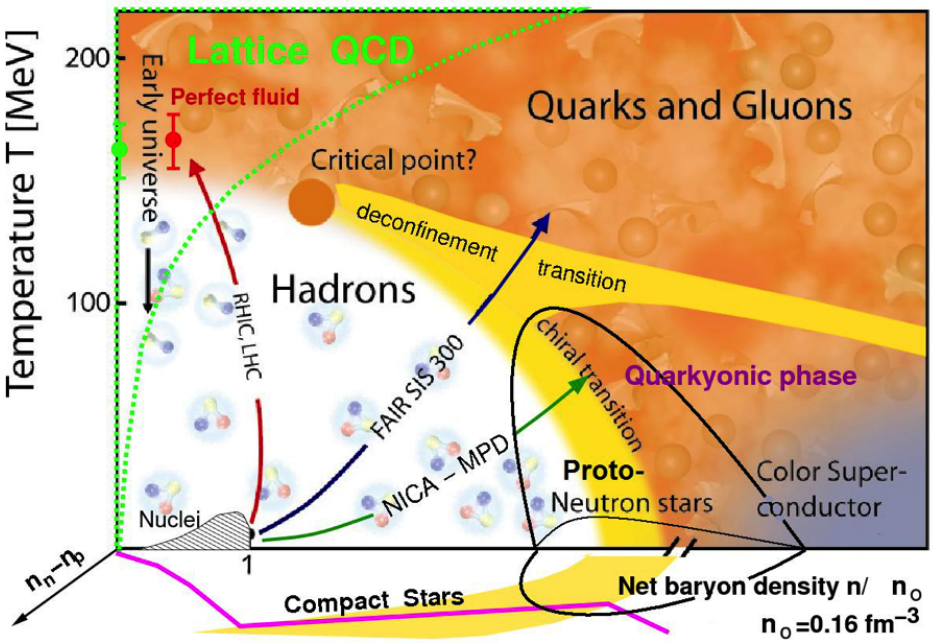

Figure 2: The QCD phase diagram where the net baryon density has been normalized such that ordinary nuclear matter (density $n_0 = 0.16 fm^{-3}$) is located at 1, from [5].

While important to study in its own right (say, to gain insight into the QCD phase diagram), QGP is also relevant in cosmology and astrophysics, as it has been theorized to have existed mere moments after the Big Bang, in the very early universe. QGP also is unusual in that it is an almost perfect fluid. Fig. 3 shows that QGP stands orders of magnitude less viscous than water and helium at relevant (critical) temperatures and pressures.

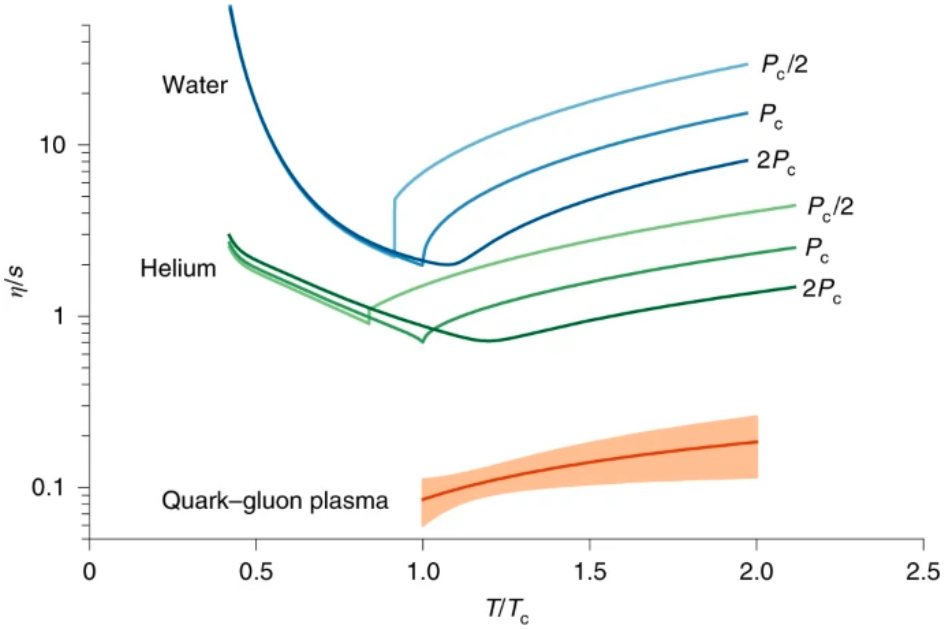

Figure 3: Estimated temperature-dependent specific shear viscosity of the QGP compared with common fluids, from [6].

A glaring question remains, though: if QGP arises in specific and extreme conditions (and is hence volatile), how can we know that colliders such as the Relativistic Heavy-Ion Collider (RHIC) or the Large Hadron Collider (LHC) generate QGP? What experimental evidence do we have that QGP is not merely a mathematical artifact of incomplete descriptions of QCD?

It turns out that elliptic flow, which is calculated through the Fourier expansion of the azimuthal distribution of particles, is a good indicator of the presence and effects of QGP. Elliptic flow measures the uniformity (or lack, thereof) of the flow of particles in all directions when viewed along the beam-axis. Anisotropic flow is calculated as follows:

$$\frac{dN}{d\phi} = \frac{N}{2\pi}\left(1 + \sum_n 2v_n \cos\left[n\left(\phi - \psi_n\right)\right]\right) \tag{1.4}$$

Here, ϕ is the azimuthal angle and ψ_n is the reaction plane angle, which orients the event along the impact parameter axis. The sine terms of the expansion are included within the cosine terms by way of the reaction plane angle. That is, we can use

$$\cos(\alpha - \beta) = \cos(\alpha)\cos(\beta) + \sin(\alpha)\sin(\beta) \tag{1.5}$$

a known trigonometric identity, to recover our sine terms.. In fig. 4, one can notice the elliptical shape of the overlap region, which leads to pressure gradients between the long and short axis.

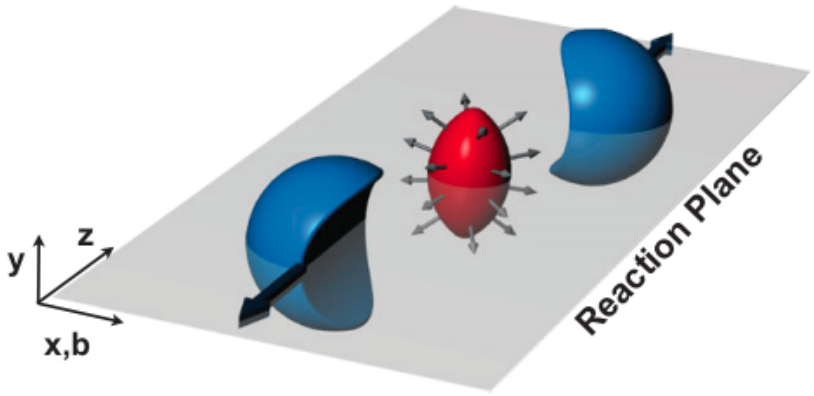

Figure 4: Two spherical nuclei collide (with non-zero impact parameter), leaving an elliptical, almond-like overlap region, from [7].

These gradients lead to elliptical flow, which equation (1.4) calculates. The elliptical nature of the overlap region means that the $\cos(2\phi)$ term, v_2, dominates the anisotropic flow calculation. Other terms, such as v_3 (or *triangular* flow), remain relevant and important. The experimental data used for comparison in this thesis, however, shows v_2 onlu. Fig. 5 shows examples of particle flows (represented by arrows emanating from the "center" of the event-plane) and their associated v_2 values, as well as their two-particle correlations $v_2\{2\}$ (which are a simple yet useful expansion of the usual v_2 calculation that look at how pairs of particles behave).

However, given our theoretical framework, we also use tools that are not available to experimentalists. One such tool is closely tied to v_n: the initial state energy anisotropy ϵ_n. To quantify the energy anisotropy of the initial state (i.e. after the collision, but before QGP formation), we use ϵ_2. Such anisotropies inevitably lead to momentum anisotropies,

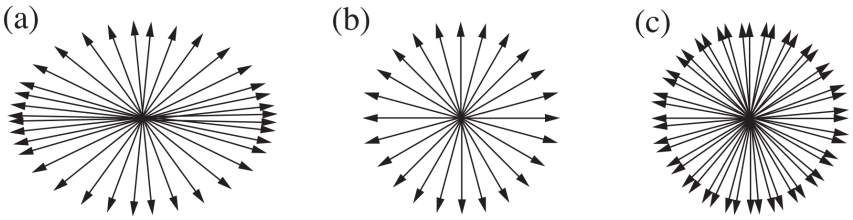

Figure 5: a) $v_2 \geq 0$, $v_2\{2\} \geq 0$, b) $v_2 = 0$, $v_2\{2\} = 0$, and c) $v_2 = 0$, $v_2\{2\} \geq 0$, from [7].

which in turn, lead to flow anisotropies, which are currently observable experimentally. Hence, initial state anisotropy is causally related to particle flow, and the expectation is that their respective distributions should look qualitatively similar for a given group of events. ϵ_n is quantified in the following way:

$$\epsilon_n = \frac{\sqrt{\langle r^n \cos(n\phi)\rangle^2 + \langle r^n \sin(n\phi)\rangle^2}}{\langle r^n \rangle} \tag{1.6}$$

where the quantities that are being averaged are the energy density weighted averages over the transverse plane, or

$$\langle * \rangle = \frac{\int d^2x * \epsilon(x)}{\int d^2x \epsilon(x)} \tag{1.7}$$

In equation (1.7), ϵ is the local energy density. These two quantities (ϵ_n & v_n) play an important role in the constant back-and-forth between the theorists and experimentalists of our field. As such, most of the results presented in this thesis will be in terms of these two values.

1.2.1 *Relativistic Hydrodynamics*

In HICs at RHIC and the LHC, signals emanating from an evolving, hydrodynamic medium were detected multiple times. As outlined in the previous section, elliptic flow is one of the tell-tale signs of hydrodynamic evolution (and, therefore, of QGP occurrence in such collisions). As such, these detections were amongst some of the most influential ever reported by RHIC. These reports culminated towards an effort to model relativistic

hydrodynamics numerically to simulate the fluid dynamics and reproduce the detected flow signatures. Our group at McGill has done significant work towards a definitive resolution of such questions, culminating in the MUSIC hydrodynamic simulation code's public release [8].

1.2.2 *HIC Theory*

When modelling HICs theoretically, it is important to consider the different phases of such events. Let t_0 be the time at which the collision occurs. Before the collision ($t \leq t_0$), the Colour Glass Condensate (CGC) framework describes the two nuclei, which assumes that the two nuclei are in the lab frame infinitely Lorentz contracted, likened to two crepes of quarks and gluons generating colour gauge fields. Immediately after the collision, and until a time inversely proportional to the saturation scale Q_S ($t_0 \leq t \leq \frac{1}{Q_S}$), we evolve the strong classical fields stemming from our sources, the large x partons (chapter 3). The saturation scale is the energy scale at which the gluon density ceases to grow, or saturates, within a high energy nucleus or hadron, which we will dive into in chapters 4 and 7. The evolution of these fields in the collision region leads to Glasma formation. The familiar thermalization stage occurs next and lasts until the system reaches equilibrium ($\frac{1}{Q_S} \leq t \leq t_{eq}$). This stage requires a mix of Glasma evolution, kinetic theory and hydrodynamics (chapter 5). Then, relativistic hydrodynamics take over, evolving the QGP until it reaches its freezeout temperature ($t_{eq} \leq t \leq t_{freezeout}$). After freezeout, the hadron gas and free streaming phases occur consecutively, the final part of which is equivalent to particles reaching the detectors at RHIC or the LHC after a run. These are, therefore, the final steps to our simulations.

Using three different numerical simulations, we are capable of systematically going through these six steps. From $t = 0$ to t_{eq}, we are in the initial state/pre-equilibrium physics portion of the simulation. IP-Glasma, which is the main driver for this thesis, handles this phase in its entirety. MUSIC, described in the previous section, handles the relativistic hydrodynamics until the QGP uniformly reaches freezeout temperature. Finally, UrQMD [9] generates the hadron gas and simulates the free streaming of particles towards the detectors.

Since this thesis is interested in quantifying the effects of known deformed nuclei on observables, it will be principally interested in outlining the specifics of IP-Glasma as a model. It will, therefore, mostly overlook MUSIC and UrQMD, both practically and theoretically. Fig. 6 shows a Minkowski diagram which outlines the major phases of HICs, and shows some of the complexities of simulating such complex systems at highly relativistic speeds. More on this later.

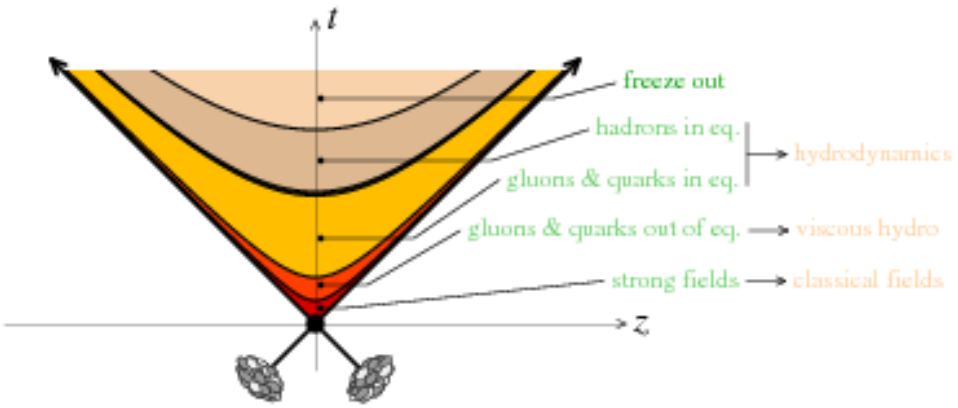

Figure 6: Schematic diagram showing the various stages of a heavy ion collision and the effective field theories by which they are governed. This thesis is focused very specifically on the the pre-collision and classical Yang-Mills dynamics represented as the two incoming nuclei, and the red strip in the light cone, respectively , from [10].

Historically, hydrodynamic models have been initialized with geometric initial conditions, such as the wounded nucleon model [11]. Therefore, simulations used to be much more simplistic in their assumptions regarding initial states. Now, the use of IP-Glasma as an initial state framework grounds these simulations further in reality, as IP-Glasma is a QCD-based model that includes geometric and sub-nucleonic fluctuations relating to the distribution of colour charge density within each nucleon, as well as saturation physics. It has become the standard in our field, reproducing flow anisotropies, multiplicity distributions, and fluctuation-based event-by-event observables.

In terms of procedure, IP-Glasma is a Monte-Carlo event generator that determines the saturation scale within the IP-Sat framework [1] and relates it to the colour charge density. Once the colour charge density calculated, IP-Glasma determines the gauge fields in the McLerran-Venugopalan (MV) [12] model and evolves them in time via the classical Yang-Mills equations. Finally, IP-Glasma computes the stress-energy tensor and diagonalizes

it to find the energy density and local velocity relevant to initializing hydrodynamical simulations. This thesis outlines the details of this process.

1.3 THESIS GOALS

As our experimental capabilities regarding HICs consistently get better, our need for a comprehensive framework to interpret new results becomes more and more critical. Thanks to Scott MacDonald's work, we now have a promising 3+1D initial conditions model, which successfully reproduces observables for a plethora of systems. A 2+1 dimensional approach to the problem of heavy-ion collisions means that we assume that each rapidity slice is the same as the most central rapidity slice. That is, we forgo any longitudinal analysis in favour of a quicker analysis which exclusively comprises the transverse plane dynamics at mid-rapidity. Scott MacDonald's intricate work has opened the door to a test of the 2+1 dimensional framework's limits (if they exist).This thesis is an effort to test such limits by colliding deformed nuclei together. By doing so, we hope to create unusual flow anisotropies and pre- and post-collision behaviour, which, we hope, will match experimental results.

However, since the most common projectile/target pairs are usually not deformed (i.e. are generally spherically symmetric), a lack in experimental results opens the door to a freer analysis of results and possibly expectations for future runs. This thesis' goal is therefore two-fold: firstly, to confirm the validity of our results against experiments [3] and published 2+1D results [2], and, secondly, to try and guide future analyses towards a common understanding of the specificities of deformed nuclei collisions. The relevant observables will be anisotropic flows v_n, while our comparison to previous 2+1D IP-Glasma results will employ initial state energy anisotropies ϵ_n.

1.3.1 *Organization*

The thesis is organized as follows: Part II contains background theory, ranging from the nucleus deformation to flow in the glasma. We will try to describe the entire underlying frameworks as accurately and concisely as possible, and further readings will be offered

along the way. Part III will discuss the relevant specifics of our simulation and numerical implementation, ranging from the organization of space to methods used for temporal evolution. It will also contain our results and conclusion. An appendix containing some calculations and relevant quantities will be found at the end.

1.3.2 *Note on conventions*

We use the mostly negative Minkowski metric signature $(+,-,-,-)$ as well as units where $\hbar = c = k_B = 1$ unless otherwise noted.

Part II

THEORETICAL FRAMEWORK

In this part, we provide detailed notes on the theory underpinning the IP-Glasma model. We will start by examining the Colour-Glass Condensate framework, its assumptions and its implications. We will then dive into the Classical Yang-Mills equations, which we will solve. We will then look at how the glasma flows before the relativistic hydrodynamics regime takes over.

2

NUCLEON POSITIONS

Heavy-Ion collisions start with system choice. That is, researchers must choose which type of systems they are looking to collide. After settling on a system, they determine the collision energy, and runs begin. In our theoretical framework, however, a more elaborate setup is required. While it also starts with system and collision energy choice, we must generate the involved nuclei. To do so, we sample from the Woods-Saxon distribution.

2.1 THE WOODS-SAXON DISTRIBUTION

For spherical nuclei, IP-Glasma samples nucleon positions according to the Woods-Saxon distribution [13, 14],

$$\rho(r) \quad = \quad = \frac{\rho_0}{1+\exp(\frac{r-R}{a})} \tag{2.1}$$

where ρ_0 is the nucleon density, R is the desired nuclear radius, and a is the nuclear skin depth. High-energy scattering experiments usually measure these parameters. This simple distribution is satisfactory for most systems, like ^{197}Au or ^{208}Pb. Using the accepted values of $R = 6.62$ fm and $a = 0.546$ fm, we obtain the plot shown in fig. 7. Note that these nuclei get their spherical nature from the lack of dependence of their nucleon density on the azimuthal and polar angles. Therefore, the radial distribution shown in fig. 7 holds in *every* direction. We sample the nucleons according to a weight

$$W(r) \quad = \quad r^2\rho(r) \tag{2.2}$$

which considers the relevant parts of the Jacobian required to sample in spherical coordinates. Intuitively, this weight function quantifies the amount of added space available as we increase r. That is, even though the Woods-Saxon distribution is a plateau for

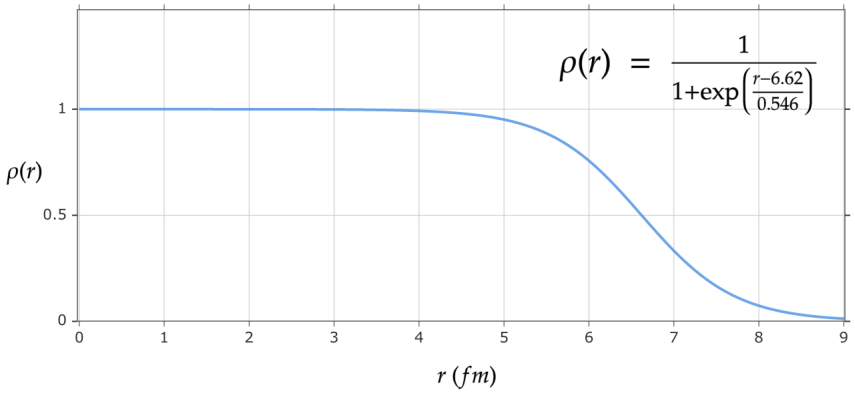

Figure 7: The Woods-Saxon distribution of a ^{208}Pb atom.

$r < R$, the lack of space close to 0 restricts our sampling to larger and larger values of r. Therefore, we find more nucleons further away from the center simply because there is extra space there - a simple fact that can be tricky. Fig. 8 shows the distribution of nucleons as one would find them (i.e. without adjusting with the Jacobian). It is clear what the effect of such considerations have on the nucleon density distribution.

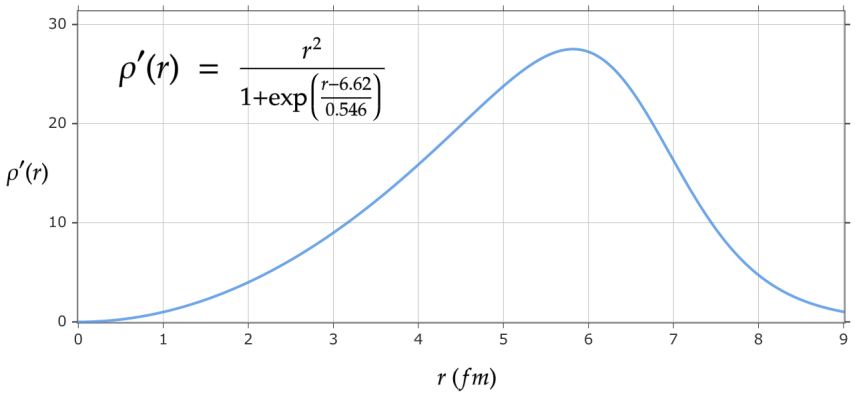

Figure 8: The Woods-Saxon distribution of a ^{208}Pb atom, multiplied by r^2, the only relevant part of its Jacobian.

Since we have established the spherical nature of the regular Woods-Saxon distribution, we can move to three dimensions. For a nucleus like ^{208}Pb, we sample r for a given nucleon, as outlined above. Then, we sample the azimuthal angle ϕ and $\cos(\theta)$, where θ is the polar angle, from uniform distributions. Using r, ϕ and θ, we can recreate the nucleon position (x, y, z). The last important step is to verify that our sampled nucleons do not overstep one another by setting a self-avoidance limit, which we check every time

a new nucleon is generated. For every new nucleon, we cycle through the list of existing nucleons and make sure that there are no nucleons within x fm of one another. In this thesis' work, we have set the self-avoidance limit to $x = 1$ fm.

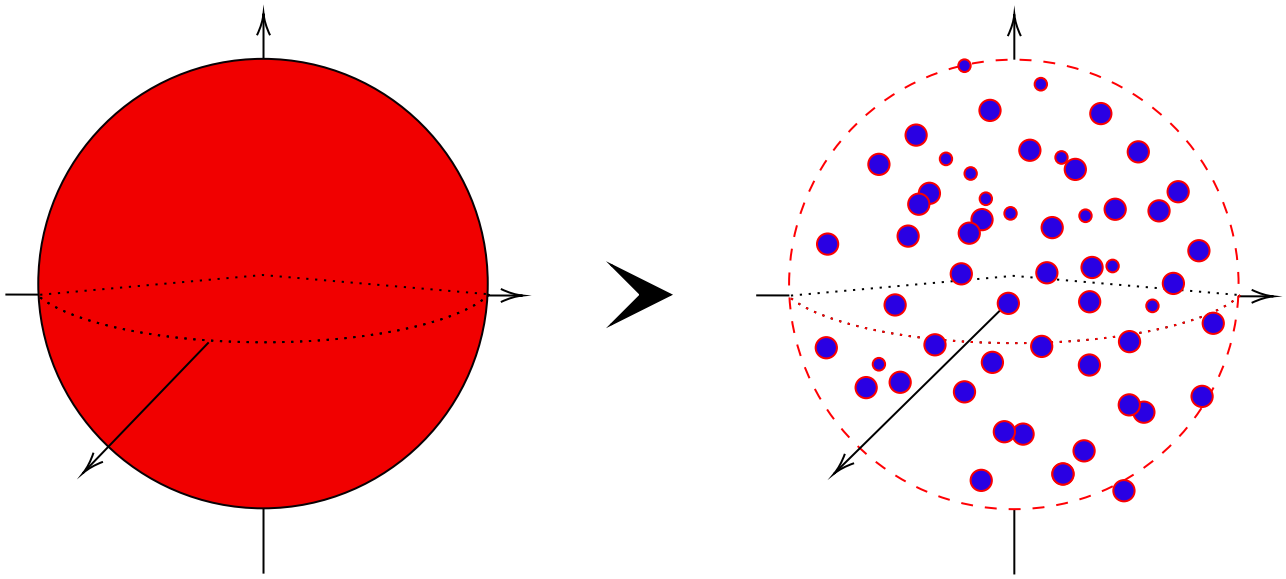

Figure 9: The spherical symmetry of the regular Woods-Saxon distribution, turned into a nucleus with specific nucleon positions. The smaller nucleons are meant to represent depth.

Fig. 9 shows, schematically, how multiple nucleon positions emerge from our perfectly spherical theoretical model. A given nucleus might have more-or-less of a spherical shape. However, once averaged, nuclei generated through Woods-Saxon samplings will produce a close-to-perfect sphere. However, this thesis concerns itself with so-called "deformed" nuclei, specifically ^{238}U.

2.2 THE DEFORMED WOODS-SAXON DISTRIBUTION

Some heavier nuclei exhibit prolate, elliptical shapes, reminiscent of an American football. How do we model such nuclei using a Woods-Saxon distribution?

A simple solution to this conundrum exists: insert some dependence on the polar angle, θ, into equation (2.1). To do so, we take the parameter R of our "regular" Woods-Saxon distribution and modify it,

$$R(\theta) = R_0(1 + \beta_2 Y_2^0(\theta) + \beta_4 Y_4^0(\theta)) \tag{2.3}$$

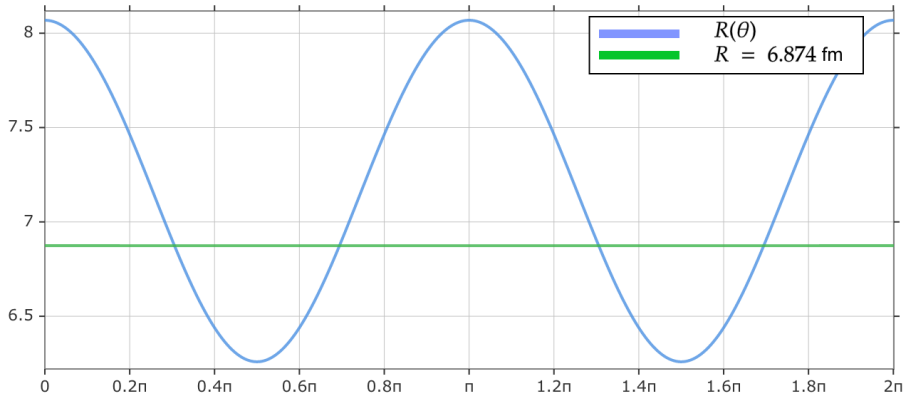

Figure 10: The R parameter's form, in the regular (constant) and deformed (equation (2.3)) Woods-Saxon distributions.

Here, our parameter R becomes R_0, and we introduce two new defining parameters to our deformed Woods-Saxon, β_2 and β_4. These multiply the spherical harmonics Y_l^m, which are familiar given their prominent place in the hydrogen atom's wavefunction, making them modulators of deformity. In other words, β_2 and β_4 control just how much deformation of the regular Woods-Saxon occurs. The spherical harmonics have the general form

$$Y_l^m(\theta,\phi) = \sqrt{\frac{2l+1}{4\pi}\frac{(l-m)!}{(l+m)!}}P_l^m(\cos(\theta))e^{im\phi} \tag{2.4}$$

$$P_l^m(x) = (-1)^m(1-x^2)^{\frac{m}{2}}\frac{d^m}{dx^m}P_l(x) \tag{2.5}$$

with $P_l(x)$ being your usual Legendre polynomial. Now, these may look unnecessarily complex. However, we are only using two specific iterations of these harmonics, namely Y_2^0 and Y_4^0, which are much simpler:

$$Y_2^0 = \sqrt{\frac{5}{16\pi}}(-1+3\cos^2(\theta)) \tag{2.6}$$

$$Y_4^0 = \frac{3}{16\sqrt{\pi}}(3-30\cos^2(\theta)+35\cos^4(\theta)) \tag{2.7}$$

These introduce the θ dependence we were seeking, in a relatively simple way. In this thesis, most of the work shown will have assumed ^{238}U's deformation parameters,

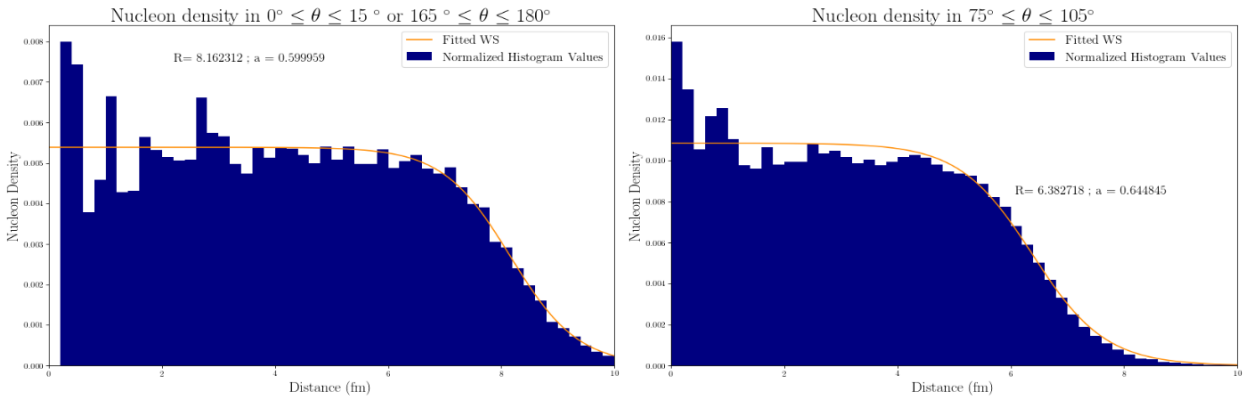

Figure 11: Directional nucleon density, averaged over 2000 nuclei. The nuclei had their long axes aligned to the z-axis beforehand.

namely $R_0 = 6.874$ fm, $a = 0.556$ fm, $\beta_2 = 0.2802$ & $\beta_4 = -0.0093$. Inserting these into equation (2.3) leads to

$$R(\theta) = 6.874(1 + 0.2802Y_2^0(\theta) - 0.0093Y_4^0(\theta)) \tag{2.8}$$

How do these spherical harmonics affect our new function $R(\theta)$? Fig. 10 shows how $R(\theta)$ varies over a full period of the polar angle.

We see how, depending on the sampled direction (polar angle) of our nucleon, the $R(\theta)$ parameter varies from $\approx$ 8 fm to $\approx$ 6 fm. This same plot, in polar coordinates, results in a prolate shape resembling an ellipse, which breaks the spherical symmetry of the Woods-Saxon distribution and therefore outputs deformed nuclei.

To further clarify the previous statement, we have added fig. 11. These two plots show the "directional" density of nucleons for a set of 2000 nuclei generated by our code, with their long axes aligned with the z-axis.

By considering only nucleons within a certain polar angle range, we can fit a new Woods-Saxon distribution on this subset of nucleons, which enables us to see just how different our nucleon distributions are in perpendicular directions. As fig. 11 shows, the long axis (which is contained within the polar angle range $\theta \in [0, \frac{\pi}{12}] \cup [\frac{11\pi}{12}, \pi]$) has a fitted Woods-Saxon R of $\approx$ 8 fm, just like in fig. 10, while the short-axis (which is contained within the polar angle range $\theta \in [\frac{5\pi}{12}, \frac{7\pi}{12}]$) has a fitted Woods-Saxon R of $\approx$ 6 fm. The full deformed Woods-Saxon for a ^{238}U nucleus is therefore

$$\rho(r,\theta) = \frac{1}{1+\exp(\frac{r-R(\theta)}{a})} \tag{2.9}$$

$$R(\theta) = 6.874(1+0.2802Y_2^0(\theta)-0.0093Y_4^0(\theta)) \tag{2.10}$$

The sampling procedure for a deformed nucleus' nucleons is, therefore, slightly different. We must first sample $\cos(\theta)$ from a uniform distribution (for $-1 \leq \cos(\theta) \leq 1$), which in turn determines that specific nucleon's $R(\theta)$ value, which then permits sampling from our Woods-Saxon distribution with $R(\theta)$ now determined.

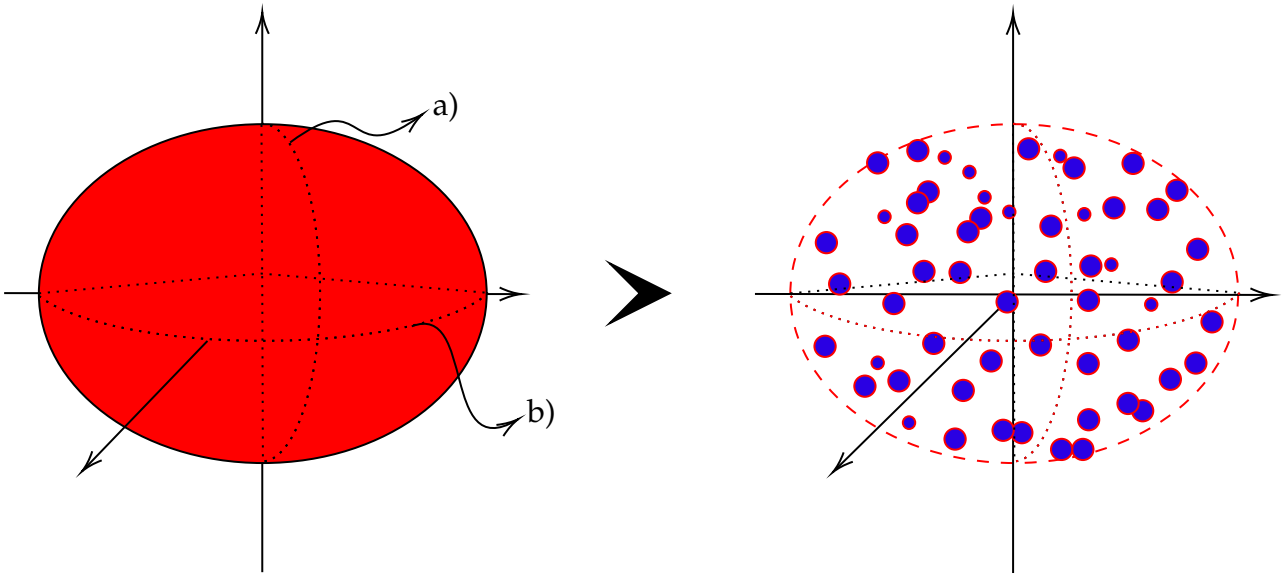

Figure 12: The clear asymmetry between the short and long axes is showcased here, schematically, where a) is the short axis and b) the long axis. This asymmetry then used to generate a nucleus with specific nucleon positions. The smaller nucleons are meant to represent depth.

The rest, including nucleon self-avoidance, proceeds as it did for regular nuclei. The final product of the process is shown schematically in fig. 12. The inherent asymmetry of these deformed nuclei leads to an extra parameter to our nucleus initialization: orientation.

2.3 NUCLEUS ORIENTATION

When the collision system includes spherical nuclei only, the overlap region's shape and properties are almost entirely defined by the impact parameter, as seen in 1, fig. 4. That is, given that the two colliding nuclei are spherically symmetric, their overlap region can range from a circle ($b = 0$ fm) to a small wedge ($b \approx R$, with R being the Woods-Saxon parameter). Of course, fluctuations in nucleon positions complicate these statements, but they remain true on average.

However, once we introduce asymmetry into the equation, the overlap region is not entirely determined by the impact parameter. Take the nucleus shown schematically in fig. 12, and assume that we set the impact parameter $b = 0$ fm. The beam axis is the z-axis. If we align the beam axis with our prolate nuclei's long axes, then the overlap, as seen in the transverse x-y plane, will be a circle. Now, take the same two nuclei, and align their small axes with the beam axis. Reiterating that our impact parameter, here, is set to 0 fm, we will observe an elliptic overlap region, closely following the outlines of both nuclei, which shows that we can create different overlap regions by simply reorienting our nuclei! Fig. 13 shows orientation conventions.

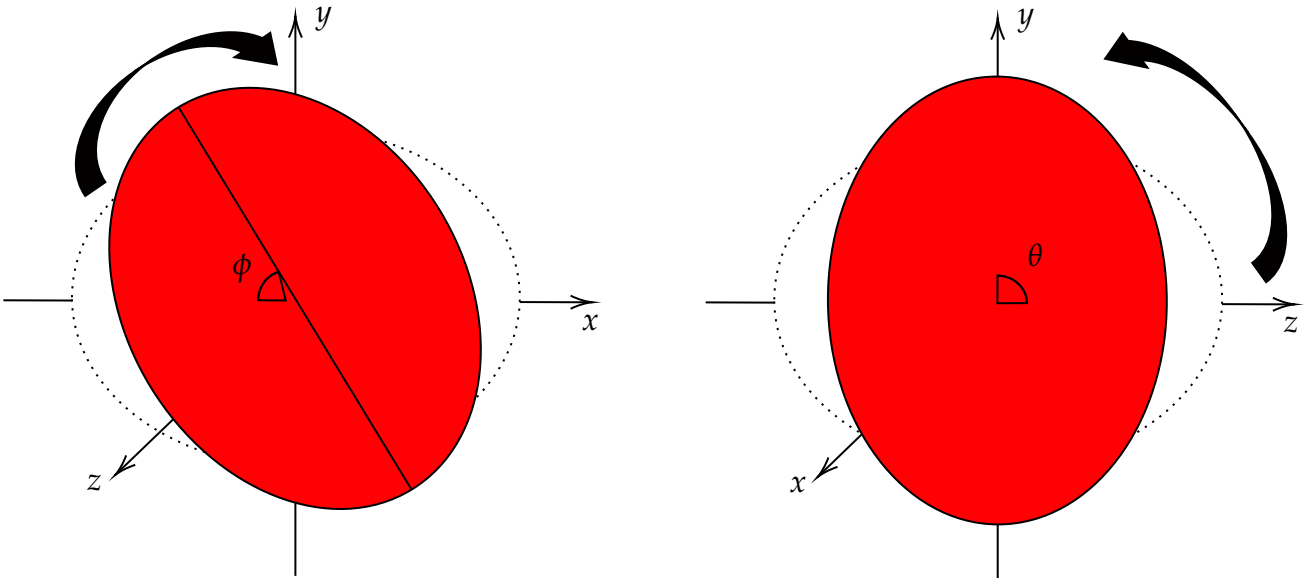

Figure 13: Orientation conventions for deformed nuclei shown schematically. Left: azimuthal angle rotation. Right: polar angle rotation.

The orientation of a deformed nucleus is set by the azimuthal and polar angles, as calculated from the nucleus' long axis. We give names to collision systems whose orientations form sought-after overlap regions. Let $\theta_1, \phi_1, \theta_2, \phi_2$ be the defining angles of our collision system's nuclei, as shown in fig. 13. Tip-tip collisions, which form circular overlap regions, occur when $\theta_1 = \theta_2 = 0$. Body-body collisions, which form oblong overlap regions, occur when $\theta_1 = \theta_2 = \frac{\pi}{2}$ and $\phi_1 = \phi_2$. While we will revisit these notions, it is important to note the following: for a given impact parameter and collision energy, tip-tip collisions produce greater particle multiplicities than body-body collisions, as the Colour-Glass Condensate, which we will dive into in Ch.3, dictates that the quark and gluon densities will be much higher for a nucleus travelling at speeds approaching the speed of light along its long axis. Therefore, the orientations of our nuclei do matter.

2.4 IMPACT PARAMETER

The impact parameter, which has already been mentioned a few times in this thesis, is defined as the separation of the centres of the incoming nuclei, as measured perpendicularly with respect to the beam axis. We sample this parameter from the distribution

$$P(b)db = \frac{2bdb}{b_{max}^2} \tag{2.11}$$

for each event. In this thesis, b_{max} will vary from dataset to dataset, and will be specified. It usually will be between 0 and 8 fm, however.

Fig 14 shows that the two nuclei, after being generated, are shifted by $\frac{b}{2}$ in opposite directions. In this thesis, this direction will be the x-axis, but it, in truth, has no effect, as long as we shift the two nuclei in opposite directions of the same axis.

For an example of what this looks like practically, fig. 15 shows two randomly oriented ^{238}U nuclei's overlap region. The colour mapping shows energy density at lattice points (which we will revisit later), while the red and green specs represent the nucleon positions of both nuclei, projected onto the transverse plane. The ellipses reproduce the approximate projections of each nuclei's Woods-Saxon distribution on the transverse plane. The figure on the right shows, in broad strokes, how the impact parameter helped

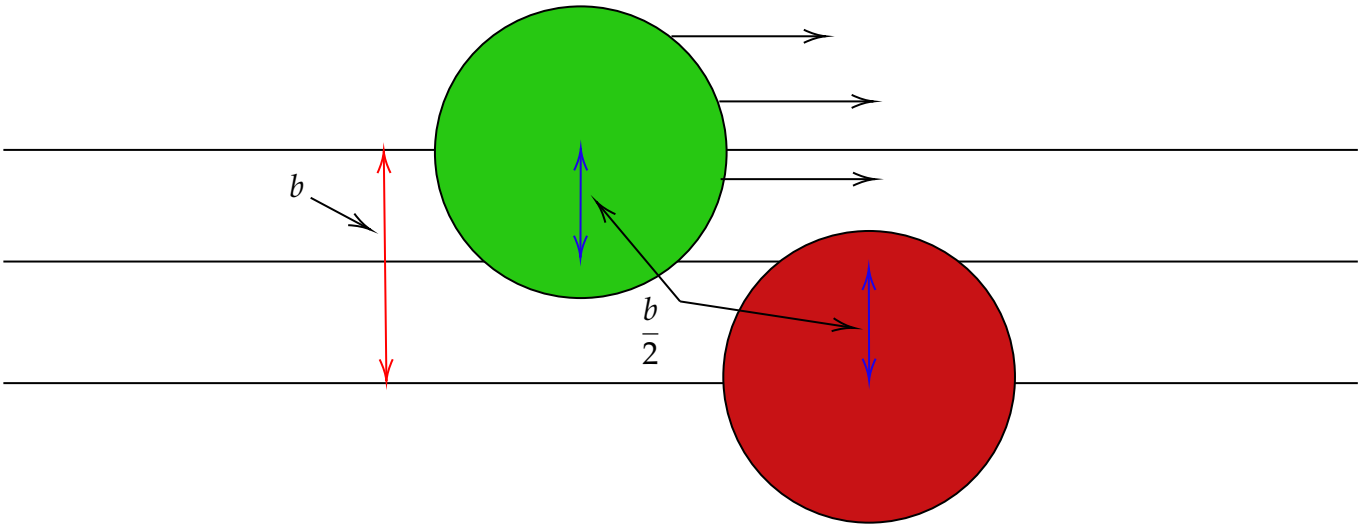

Figure 14: Schematic view of the impact parameter. In green, the projectile nucleus, and in red, the target. Each are shifted by $\frac{b}{2}$.

produce the overlap region from two elliptical nuclei, and how it affects their respective positions in the transverse plane in our simulations.

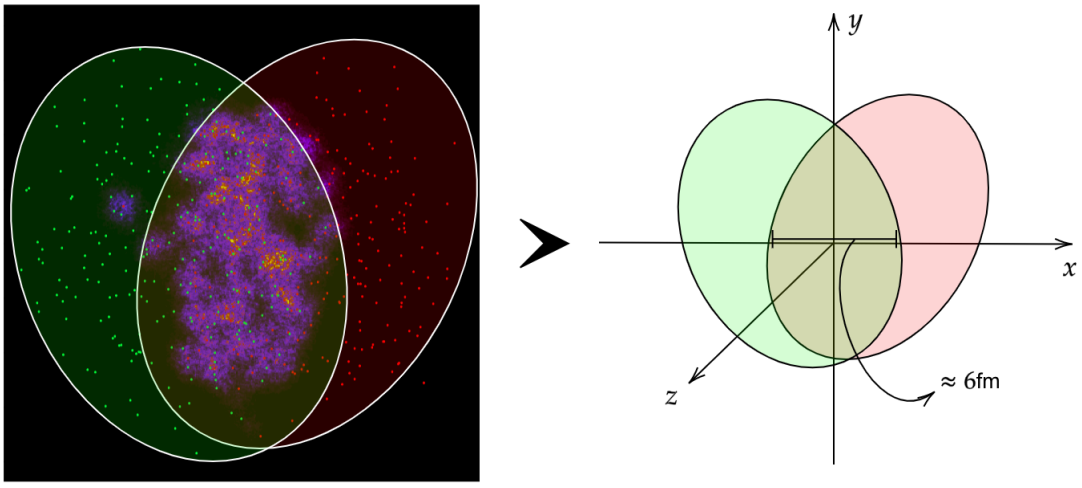

Figure 15: Left: A U-U collision system's overlap, at $\sqrt{s} = 193$ GeV, and $b = 6.1$ fm. Right: Schematic reproduction of the overlap region and of the impact parameter's role.

3

COLOUR-GLASS CONDENSATE

3.1 THE IDEA

The theoretical framework that governs the pre-collision dynamics of heavy-ion collisions is the Colour-Glass Condensate (CGC), an effective field theory. The name seems farfetched, but is actually quite evocative.

The "Colour" refers to the colour charges of QCD. As mentioned in ch. 1, nucleons are made of quarks and gluons, which all carry colour charge inherently. We have also outlined how a nucleon's valence quarks are used to classify it, in the presence of a "sea" of quarks coming into and out of existence in the background. This concept is central to CGC, as now, this sea of quarks is taken into consideration, and so are all of the gluons keeping it together. This means that our colliding nuclei are actually considered in terms of colour charges and colour gauge fields, and not their actual nucleons. Instead of the purely-geometric considerations of previous frameworks, we now implicate colour charge as the central driver for the formation of QGP.

The more eyebrow-raising term in the expression is "glass". Glass, as we know it, seems solid. However, it is actually an amorphous solid, which indicates that it is neither fully solid nor liquid. That is, on short time scales, glass behaves like a solid (as we see it, touch it and use it). On longer time scales, it acts as a fluid. Glass molecules flow slowly through its irregular structure all the time.Therefore, in physics, the term "glass" refers to any material exhibiting such properties. The "glass" in CGC refers to the boosted partons, which travel at highly relativistic velocities, and that act as sources for the colour gauge fields. This in turn creates a time dilation effect experienced by the partons in the lab frame. They are moving so fast that, as experienced by most of the interaction region and the lab, they are essentially "frozen" over the time scale of the interaction between

the two nuclei. In this approximation, the properties of the high-energy partons do not change, and they become static sources with respect to the interaction region.

Finally, the term "condensate" refers to the coherent behaviour of gluons in CGC. This coherent behaviour can be observed at length scales smaller than Q_s^{-1}, where Q_s is the saturation scale (more on that later), and is in large part due to the very high phase space density of gluons.

3.2 THE EFFECTIVE LAGRANGIAN

In ch. 1, we quickly dissected the QCD Lagrangian in order to expose the differences between gluons and photons, and more generally between the strong and electromagnetic forces. As a refresher, here it is again:

$$\mathcal{L}_{QCD} = \sum_q \bar{\psi}_{q,a} \left(i\gamma^\mu \partial_\mu \delta_{ab} - g_s \gamma^\mu t^C_{ab} \mathcal{A}^C_\mu - m_q \delta_{ab} \right) \psi_{q,b} - \frac{1}{4} F^A_{\mu\nu} F^{A\mu\nu} \tag{3.1}$$

$$F^A_{\mu\nu} = \partial_\mu \mathcal{A}^A_\nu - \partial_\nu \mathcal{A}^A_\mu - g_s f_{ABC} \mathcal{A}^B_\mu \mathcal{A}^C_\nu \tag{3.2}$$

This is the fundamental Lagrangian, which takes the different quark flavours and colour indices. Solving this for a specific system is no simple task, even when using powerful supercomputers. Therefore, we need a more concise and simple approach. CGC's answer to this problem is the *effective* Lagrangian,

$$\mathcal{L}_{CGC} = J^{\mu a} A^a_\mu - \frac{1}{4} F^a_{\mu\nu} F^{a\mu\nu} \tag{3.3}$$

where it is important to note, for clarity, that the colour indices A in equation (3.1) become lower-case a in (3.3).

There are a few clear differences right from the start. Firstly, $\mathcal{L}_{CGC}$ does not have any fermions, which is caused by the CGC being an *effective field theory*. That is, it describes the system in terms of effective degrees of freedom. In CGC, those degrees of freedom are colour gauge fields that end up separated according to their respective energy scales. Let $x = \frac{k}{P}$, with k being the momentum of a given parton and P, the momentum of the hadron. x describes the fraction of the total nuclear momentum carried by a specific

parton. Large x partons are treated as external sources $J^{\mu a}$ for the slow, small x partons. In other words, the fast partons are classical colour sources with respect to the small x partons. These fast partons include the valence quarks, which serve as static sources, frozen by Lorentz time dilation on the time scale of the interaction. In more technical terms, the degrees of freedom in this framework are colour source ρ at large x and gauge fields A^{μ} at small x. Furthermore, the small x partons couple to the large x partons, as equation (3.3) makes clear.

Fig. 16 shows the parton distribution functions obtained by fitting to HERA data. The plot clearly demonstrates that small x gluons dominate the distribution functions (at this specific scale). At higher energies, the fact that gluons radiate other gluons exacerbates this phenomenon until the system reaches saturation. More on this later.

As mentioned previously, the colour sources ρ are assumed to be infinitely Lorentz contracted. They are therefore treated as surface charge densities (which is why they are designated by the variable ρ), propagating along the light cone. The CGC framework uses the "infinite momentum limit" on its nuclei to create these simplistic conditions. Therefore, the nuclei are considered to be moving at the speed of light, no matter what the collision energy is. At the LHC, where the center of mass energy is 2.76 TeV, this leads to a Lorentz factor of 1470, which in turn leads to a longitudinal nuclear width of 0.0082 fm, while it a typical nucleus is usually $\approx$ 12 fm wide. In this thesis, however, the center of mass energies are much smaller, at 193 GeV. This leads to

$$\gamma = \frac{E}{m} = \frac{\sqrt{s}/2}{m} \approx \frac{97\text{GeV}}{0.940\text{GeV}} = 103 \tag{3.4}$$

$$\Rightarrow \text{Nuclear Width} = \frac{2R_{nuc}}{\gamma} = \frac{12\text{fm}}{103} \approx 0.12\text{fm} \tag{3.5}$$

While the approximation is better at greater energies, it still is acceptable at the energies that this thesis aims to study. At the scale of our nucleons, which are about 1 fm in diameter, this translates to target and projectile nucleons seeing one another with less than 1 percent of the longitudinal extent of what they would usually "see" at rest. The contraction applies to large x valence partons that carry large fractions of the nuclei's momentum [16].

However, small x partons must be dealt with differently. Given that $x \ll R_{nuc}$, these partons become delocalized over distances larger than the nuclear radius. That is, quan-

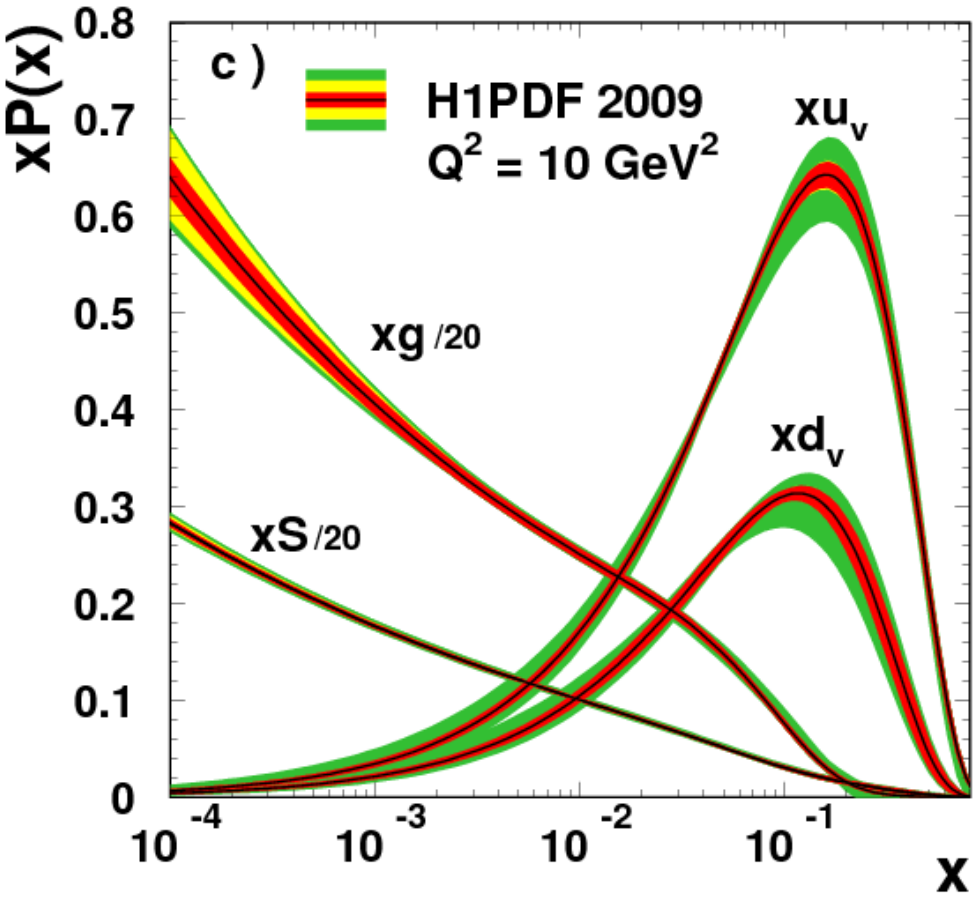

Figure 16: The different curves correspond to different parton distribution functions where xu_v is for the valence up quark ($u_v = u - \bar{u}$, quarks minus antiquarks), xd_v is for the valence down quark, xS is for sea quarks (quarks that have not been accounted for yet, such as the anti-up and anti-down quarks along with strange and anti-strange quarks), and xg is for gluons. The gluon and sea quark curves are divided by a factor of 20 to make the plot compact and readable. Data produced by HERA, from [15].

tum mechanics and the uncertainty principle dictate that small x partons see the large x source terms as infinitely thin in the longitudinal direction. To make this clear, we use the relativistic dispersion relation, coupled to the uncertainty principle:

$$\Delta x^+ \approx \frac{1}{k^-} \tag{3.6}$$

$$m^2 = E^2 - \boldsymbol{k}^2 = 2k^+k^- - \boldsymbol{k}_\perp^2 \tag{3.7}$$

$$\Rightarrow k^- = \frac{m^2 + \boldsymbol{k}_\perp^2}{2k^+} = \frac{m_\perp^2}{2xP^+} \tag{3.8}$$

Here, $x^{\pm} = x_{\mp} = (x^0 \pm x^3)/\sqrt{2}$, which is the light cone coordinate of a parton and $k^{\mp}$ is it conjugate momentum in the same coordinate system (see appendix A for details). Equation (3.6) is first used to estimate the lifetime of a given parton. We then translate the usual relativistic dispersion relation to our light-cone coordinate system, leading to equation (3.7). We then rearrange equation (3.7) to gain a more intuitive form, (3.8), where $m_{\perp}^2 = m^2 + \boldsymbol{k}_{\perp}^2$, and we've used $k^+ = xP^+$, where P^+ is the total momentum carried by the of the nucleus and x is the fraction of said momentum carried by the parton under study, as outlined previously. Finally, we insert equation (3.6) into equation (3.8) to obtain

$$\Delta x^+ \approx \frac{xP^+}{m_{\perp}^2} \tag{3.9}$$

Thus, the lifetime Δx^+ of each parton is proportional to x, its momentum fraction, which implies that large x partons, such as our valence quarks, live much longer than their small x counterparts. This difference in longevity reiterates that, to small x and short-lived gluons, the large x sources seem frozen.

Now that we've established our frozen sources approximation, we can outline how said sources are represented in equation (3.1), our $\mathcal{L}_{QCD}$. The sources are found in the $J^{\mu a}$ term. To represent their lack of evolution over the relevant time scales and two-dimensional nature, the large x partons are represented using delta functions which move along the light cone before and after the collision takes place:

$$J^{\mu a}(x) = \rho_A^a\left(\mathbf{x}_{\perp}\right)\delta^{\mu+}\delta\left(x^-\right) + \rho_B^a\left(\mathbf{x}_{\perp}\right)\delta^{\mu-}\delta\left(x^+\right) \tag{3.10}$$

In 3.10, the two colliding nuclei are represented by the subscripts A and B. As stated above, the delta function enforce the two-dimensional nature of the relevant partons and their spatiotemporal position along the light cone. The charge density functions $\rho(x)$ are unique to both nuclei. These are generated through stochastic sampling due to event-by-event fluctuations. The CGC provides a gauge-invariant distribution of $W[\rho]$, which gives the probability of obtaining a specific configuration of ρ. This functional encodes all the correlations of the colour charge density at the relevant cutoff scale between slow

and fast degrees of freedom. Given this statistical distribution, the expectation value of for a given operator is given by

$$\langle O \rangle = \int [D\rho] W[\rho] O[\rho] \tag{3.11}$$

where O is the operator in question. In this thesis, the weight function $W[\rho]$ takes the form of a Gaussian, following the McLerran-Venugopalan [12] model. However, why are we not accounting for deflections of these large x partons during collisions?

3.3 THE EIKONAL APPROXIMATION

We use the eikonal approximation in many different areas of physics. It aims to reduce the complexity of systems by reducing differential equations to a single variable and was first used in the CGC framework by Iancu, Leonidov and McLerran [17]. To start our proof of validity, we define rapidity in terms of the momentum fraction x, which is

$$x = \frac{k^+}{P^+} \tag{3.12}$$

We can then define the following *approximation* for rapidity,

$$y \approx \ln\left(\frac{1}{x}\right) \tag{3.13}$$

It is important to note, here, that rapidity is related to the direction and momentum of a particle, ranging from $-\inf$, for particles travelling down the negative beam axis, to $+\inf$, for particles travelling down the positive beam axis. A particle travelling purely in the transverse plane will have a rapidity of zero. Rapidity is a particularly useful tool to describe heavy-ion collisions because it is additive under Lorentz boosts. The approximate form shown in equation (3.13) is handy for quick estimates of a parton's rapidity. The eikonal approximation, however, requires the exact form of rapidity in light cone coordinates, which is

$$y = \frac{1}{2} \ln\left(\frac{k^+}{k^-}\right) \tag{3.14}$$

where $k^{\pm} = k_{\mp} = (k^0 \pm k^3)/\sqrt{2}$. We then use the definition of the transverse mass, outlined in equation (3.8), to simplify further:

$$m_\perp^2 = \boldsymbol{k}_\perp^2 + m^2 = E^2 - k_z^2 = 2k^+k^- \tag{3.15}$$

$$\Rightarrow y = \frac{1}{2}\ln\left(\frac{2(k^+)^2}{m_\perp^2}\right) \tag{3.16}$$

Then, any particle which contributes or is created during the collision can be qualified using its rapidity as follows:

$$y = \frac{1}{2}\ln\left(\frac{2(k^+)^2}{m_\perp^2}\right) = \ln\left(\frac{\sqrt{2}(xP^+)}{m_\perp}\right) \tag{3.17}$$

Finally, defining

$$y_{proj} = \ln\left(\frac{\sqrt{2}P^+}{M}\right) \tag{3.18}$$

where M is the mass of our nucleus and P^+, as defined above, is its momentum, allows us to write

$$y = \ln\left(\frac{M}{m_\perp}\right) - \ln\left(\frac{1}{x}\right) + y_{proj} \tag{3.19}$$

where our initial approximation for rapidity from equation (3.13) can be found.

Now, obviously, in order for the eikonal approximation to be valid in our analysis, it must be that our large x partons, the frozen sources of our framework, travel at rapidities close to that of our initial beam, or the colliding nuclei. This imposes the following condition on equation (3.19):

$$y \approx y_{proj} \iff \tag{3.20}$$

$$\ln\left(\frac{M}{m_\perp}\right) - \ln\left(\frac{1}{x}\right) \approx 0 \iff \tag{3.21}$$

$$\ln\left(\frac{M}{m_\perp}\right) \approx \ln\left(\frac{1}{x}\right) \tag{3.22}$$

$$\Rightarrow x \approx \frac{m_\perp}{M} = \frac{\sqrt{m^2 + \boldsymbol{k}_\perp^2}}{M} \tag{3.23}$$

Then, if we look at the valence partons (which make up most of the mass of a nucleus), we will have $m \approx M$, which leaves us with $k_\perp \ll m$, which means that our valence partons do not have much transverse momentum. Therefore, we use the eikonal approximation to ignore deviations in the large x partons' path, which would be extremely subtle.

McLerran and Venugopalan ([12]) give another way of motivating the use of the eikonal approximation. The authors explain that the primary parton production mechanism is bremsstrahlung, which transfers minimal amounts of momentum to the radiated particles (a *soft* transfer). This small transfer would leave our sources, the valence quarks, as recoilless particles moving along the light cone.

3.4 SEPARATING SCALES

No matter how one perceives it, the eikonal approximation leaves a system of strong, classical colour gauge fields behind. The high energies at hand allow us to treat these fields classically since the usual quantum corrections would be negligible. The quantum field theory at hand makes this clearer. The high number of gluons leads to a large occupancy number N_g, which towers over the value of the commutator of the raising and lowering operators. That is,

$$\langle N_k \rangle = \langle a_k^\dagger a_k \rangle \gg \langle \left[a_k, a_k^\dagger \right] \rangle = 1 \tag{3.24}$$

Phrased as above, this seems like a technical artifact, and its use is doubtful. However, this is analogous to large systems in the everyday world. Newtonian mechanics describe these systems exceptionally well. Quantum corrections are only required once we dive closer and reduce the size of these systems. This same separation of scales exists in QCD! The high density of gluons at all points of the interaction region makes our system large enough that quantum corrections are subdominant. What are these classical considerations, then? They are the classical Yang-Mills equations - our equations of motions - which we will now describe in detail.

4

SOLVING THE CLASSICAL YANG-MILLS EQUATIONS

As stated in our introduction, QED and QCD share some key features but diverge on others. The fact that QCD has multiple colour charges adds much complexity to this theory. While we use Maxwell's equations to determine the features of large electromagnetic systems, they cannot describe multiple different types of charges. That is where the Yang-Mills equations step in. A scalar can represent an electromagnetic charge, while colour charge must be represented on a vector space. The Euler-Lagrange equation applied to $\mathcal{L}_{CGC}$ (3.3) lends

$$[D_\mu, F^{\mu\nu}]_a = J_a^\nu \tag{4.1}$$

$$D_\mu = \partial_\mu + igA_\mu^a t^a \tag{4.2}$$

Since this was obtained using the CGC Lagrangian, J_a^ν is the source term, as described in equation (3.10). Now, these equations of motion resemble those of QED, except for the colour index a. This colour index represents the vector space described above and is part of an SU(3) symmetry because of the three existing colour charges - red, green and blue. This change may seem small and inconsequential at first, but it carries much weight in actuality. First of all, fields in QCD are matrices that do not commute with one another, making this theory non-abelian. Given that our EOMs include the covariant derivative D_μ, our equations will be non-linear. Said covariant derivative would introduce commutator terms in our colour gauge fields, which will not be linear. As mentioned previously, this means that contrarily to photons, which are neutral and do not interact with one another, gluons interact with one another. These interactions add a plethora of additional diagrams and vertices which complicate perturbative calculations. Finally, the non-abelian nature of the Yang-Mills equations leads to a negative beta func-

tion in the renormalization group flow. This is the root cause of the *asymptotic freedom* described in chapter 1. In the following sections, we will outline various results related to the Yang-Mills equations. These will be key to evolving our system after the initial collision and into the glasma phase, which is central to the IP-Glasma framework. Their detailed mathematical derivations will be added to appendix A.

We start by looking at the colour gauge fields stemming from a single nucleus before the collision. These fields evolve in regions 2 and 4 of figure 17, and, once the nuclei collide, are transported into region 1 and produce glasma.

4.1 LIGHT CONE BOUNDARY

The gluon field strength tensor is given by

$$F^a_{\mu\nu} = \partial_\mu A^a_\nu - \partial_\nu A^a_\mu - g_s f_{abc} A^b_\mu A^c_\nu \tag{4.3}$$

In chapter 3, we derived a few key equations using light cone, or $\tau - \eta$ coordinates. These are used throughout this thesis and are outlined in appendix A. The field strength tensor, as presented in equation (4.3), is not in $\tau - \eta$ coordinates. Therefore, we must find the expression for our colour gauge field strength tensor in the relevant coordinate system. We start by noting that

$$\tau = \sqrt{t^2 - z^2} \tag{4.4}$$

$$\eta = \frac{1}{2} \ln \left(\frac{t+z}{t-z} \right) \tag{4.5}$$

where t and z are the usual time and spatial coordinates. Equation (4.5) shows the rapidity, which we used in section 3.3, in a different form. Recalling that our $\tau - \eta$ coordinates can easily be transformed into specific $\pm$ indices for propagation in the negative and positive beam directions, $F^a_{\mu\nu}$ becomes

$$F^{i\pm} = \partial^i A^\pm - \partial^\pm A^i - ig \left[A^i, A^\pm \right] \tag{4.6}$$

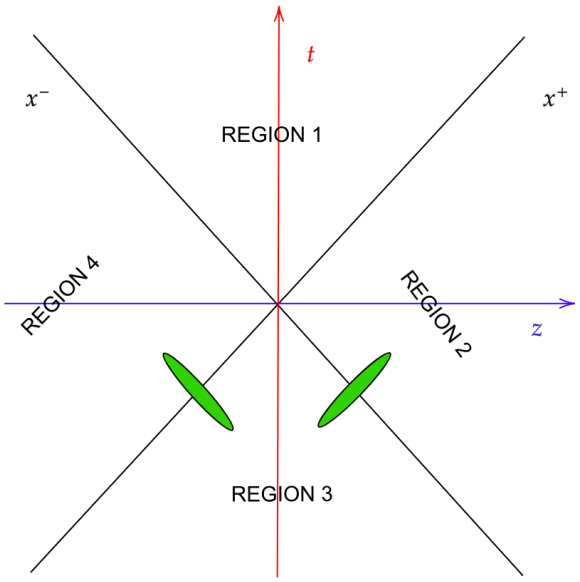

Figure 17: Different spacetime regions of our collision, as depicted on this Minkowski diagram. The nuclei are represented in green on the light lines.

We know that the sources for our classical gluon fields are the hard partons which travel along the light cone, undeflected due to the eikonal approximation. Recall that we write the colour current

$$J_a^{\pm} = g\rho_a\left(x^{\mp}, \boldsymbol{x}_{\perp}\right) \tag{4.7}$$

As we know, the CGC framework models both nuclei as infinitely Lorentz contracted, 2-dimensional sheets of colour charge fluctuations. This approximation means that outside of our two nuclei (whose large x partons keep travelling near the speed of light after the collision), our solution must solve the equations of motions derived previously.

These questions have been tackled in [12, 18, 19], which allows us to use these results to our advantage. We are seeking the boundary conditions along the light cone created by our colliding nuclei. We will first examine the regions directly outside of the light cone, which are not the subject of our study but are necessary to a full understanding. By choosing a covariant gauge, we can cancel some of the colour gauge fields. Since both of these regions are symmetric about the light cone, their solutions will be analogous. Taking the region to the "left" (in Minkowski terms) of our backward-propagating

nucleus (region 4 in fig. 17), we will have $A^+ = A^i = 0$, as a consequence of our choice of gauge. This choice leads our field strength tensor to become

$$F^{i-} = \partial^i A_C^- \tag{4.8}$$

since its other relevant components have vanished. We can insert equation (4.8) into the sourced classical Yang-Mills equation

$$\left[D_i, F^{i-}\right] = J^- \tag{4.9}$$

we obtain

$$\partial_i \partial^i A^- = J^- \tag{4.10}$$

This is a two-dimensional Poisson equation, which is a well-known partial differential equation. We write its solution

$$A^- = \frac{-g\rho\left(x^+, \boldsymbol{x}_\perp\right)}{\nabla_\perp^2} \tag{4.11}$$

and, as is usual in physics, we require that our gauge fields vanish at infinity. This same process yields

$$A^+ = \frac{-g\rho\left(x^-, \boldsymbol{x}_\perp\right)}{\nabla_\perp^2} \tag{4.12}$$

for the region to the "right" of our forward-propagating nucleus, (region 2 in fig. 17). It is now important to transform our gauge since our system is not in the covariant gauge, but the light-cone gauge. We know that gauge transformations take the form

$$A_\mu^a(x)t^a \to V(x)\left(A_\mu^a(x)t^a + \frac{i}{g}\partial_\mu\right)V^\dagger(x) \tag{4.13}$$

with V being the gauge transformation matrix at hand. Then, transforming to the light-cone gauge for region 4 of fig. 17 would give

$$A^- = 0 \tag{4.14}$$
$$A^i = \frac{i}{g} V \partial^i V^\dagger \tag{4.15}$$
$$i\partial_- V^\dagger = g A^+ V^\dagger \tag{4.16}$$

Referring to equation (4.13), we see that our field must be a pure gauge field in that region. Using well-known techniques to find V by inserting our Poisson equation solutions in equation (4.16), we can solve for our gauge fields, which yields

$$A^i = i \left(\mathrm{P} \exp \left[ig \int_{-\infty}^{x^-} \frac{-1}{\nabla_\perp^2} \rho \left(z^-, \boldsymbol{x}_\perp \right) dz^- \right] \right) \cdot \nabla^i \left(\mathrm{P} \exp \left[ig \int_{-\infty}^{x^-} \frac{-1}{\nabla_\perp^2} \rho \left(z^-, \boldsymbol{x}_\perp \right) dz^- \right] \right) \tag{4.17}$$

Although this result seems exceptionally complicated, it is what we needed. Our charge densities are now related to our pure gauge fields for each nucleus before the collision. We now need to relate these pre-collision, pure gauge colour fields to our post-collision system.

In this post-collision system, our colour gauge sources include both nuclei. This means that our source term is now a sum of our two colour sources,

$$J_{tot} = g\rho_A \left(x^-, \boldsymbol{x}_\perp \right) + g\rho_B \left(x^+, \boldsymbol{x}_\perp \right) \tag{4.18}$$

Now, these nuclei are moving in opposite directions, on the x^+ and x^- axes of fig. 17. Our nuclei are moving at the speed of light, which means that their fields cannot precede them. It also implies that said fields are pure gauge in their wake. This means that our gauge fields are given by [20]

$$A^i = A_A^i \left(\boldsymbol{x}_\perp \right) \theta \left(x^- \right) \theta \left(-x^+ \right) + A_B^i \left(\boldsymbol{x}_\perp \right) \theta \left(x^+ \right) \theta \left(x^- \right) \tag{4.19}$$
$$A^\pm = 0 \tag{4.20}$$

where the A and B subscripts represent our two nuclei. An interesting consequence of these solutions is that our nucleus' charge density is related to the discontinuity de-

scribed by our colour gauge fields at our nuclei's spatial positions. That is, before the collision, we have

$$\nabla_i A_A^i = \rho_A \left(\boldsymbol{x}_\perp \right) \tag{4.21}$$

with the same being true for nucleus B. Our solutions equation (4.19) and (4.20) have another consequence, which is that all components of F^{ij} vanish, meaning that our solution is exact in regions 2 and 4 for fig. 17.

After the collision, our solution changes. Instead of having a pure gauge field, we now have a complex arrangement of colour gauge sources that generate gluons in the interaction region. All of our sources remain on the light cone, as dictated by the CGC framework.

To obtain the post-collision solutions, we must first move to the Schwinger gauge [20],

$$x^- A^+ + x^+ A^- = 0 \tag{4.22}$$

We then take the following ansatz, which will also be used to determine our colour gauge field strength tensors in section 4.3:

$$A^\pm = \pm x^\pm \alpha(\boldsymbol{x}_\perp, \tau) \tag{4.23}$$

$$A^i = \alpha_\perp^i(\boldsymbol{x}_\perp, \tau) \tag{4.24}$$

Before and after the collision, our nuclei colliding at $\tau = 0$ connect the different regions of spacetime. Therefore, we must match our colour gauge field solutions before and after the collision at this point in spacetime.

$$\alpha_\perp^i\Big|_{\tau=0} = \alpha_1^i + \alpha_2^i \tag{4.25}$$

$$\alpha|_{\tau=0} = \tfrac{ig}{2}\left[\alpha_1^i, \alpha_2^i\right] \tag{4.26}$$

where $\alpha_{1,2}$ are required because of a singularity on the light cone exhibited by $\left[D_\mu, F^{\mu i}\right] = 0$, which will be solved in section 4.3. We can now eliminate our αs by rewriting in terms of our colour gauge fields

$$A^+\big|_{\tau=0} = x^+ \frac{ig}{2}\left[A_A^i(\tau,\boldsymbol{x}_\perp), A_B^i(\tau,\boldsymbol{x}_\perp)\right] \tag{4.27}$$

$$A^-\big|_{\tau=0} = x^- \frac{ig}{2}\left[A_A^i(\tau,\boldsymbol{x}_\perp), A_B^i(\tau,\boldsymbol{x}_\perp)\right] \tag{4.28}$$

$$A^i\Big|_{\tau=0} = A_A^i(\boldsymbol{x}_\perp) + A_B^i(\boldsymbol{x}_\perp) \tag{4.29}$$

This shows that our initial charge distributions, which are sampled and stochastic, define our fields after the collision via the pure gauge fields existing before the collision. These represent the initial state of our glasma, which is then evolved using the Classical Yang-Mills equations of motion, which we will solve shortly. For now, let us quickly examine how we obtain our initial fields from our Poisson equations.

4.2 WILSON LINES AND THE INITIAL FIELDS

Recall that we had obtained

$$A^\pm = \frac{-g\rho(x^\mp,\boldsymbol{x}_\perp)}{\nabla_\perp^2} \tag{4.30}$$

as our solution to the Poisson equation which had risen from our source equations of motion. We now use a widespread trick in PDE analysis, which takes the Fourier transform of our solution. This yields

$$A^\pm(\boldsymbol{k}_\perp) = \frac{g\rho(\boldsymbol{k}_\perp)}{\boldsymbol{k}_\perp^2} \tag{4.31}$$

This simplifies our earlier problem from a differential problem to an algebraic problem. We can solve this new equation and take the solution's Fourier transform to obtain our initial fields. This allows us to write the following expression

$$V(\boldsymbol{x}_\perp) = P\exp\left(i\int dx^- A^+\left(x^-,\boldsymbol{x}_\perp\right)\right) \tag{4.32}$$

Wilson lines are given by the path ordered exponential of a given gauge field. We can discretize this expression as follows

$$V(\boldsymbol{x}_\perp) = \prod_{k=1}^{N_y} \exp\left\{\frac{-ig\rho(\boldsymbol{x}_\perp)}{\nabla_\perp^2 - m^2}\right\} \tag{4.33}$$

Here, m is an infrared cutoff which leaves out momentum modes below it and protects our results from dreaded infrared divergences. Conveniently, the modes which are left out thanks to such a cutoff are those that should be subject to colour confinement. These Wilson lines are precisely the gauge transformation matrices V described earlier. Inserting our discretized expression (4.33) into (4.15) and solving for the gauge fields. We will be using Wilson lines, and specifically, our discretized expression while talking about implementing all of this theory mathematically via the lattice. We are now finally ready to look at the theory behind the colour charge densities, which is now clearly central to our classical Yang-Mills equation solving methods.

4.3 $F^a_{\mu\nu}$ AND THE EQUATIONS OF MOTION

We are now ready to understand how these initial gauge fields evolve after the collision. Recall the ansatz taken at the end of section 4.1

$$A^\pm = \pm x^\pm \alpha(\boldsymbol{x}_\perp, \tau) \tag{4.34}$$

$$A^i = \alpha^i_\perp(\boldsymbol{x}_\perp, \tau) \tag{4.35}$$

which is taken at $\tau = 0$ and therefore concerns all fields in the forward light cone (i.e. after the collision, in figure 6).

Using this, along with equation (**??**), we arrive at

$$F^{i\pm} = \partial^i(\pm x^\pm \alpha) - \partial_\mp \alpha^i_\perp - ig\left[\alpha^i_\perp, \pm x^\pm \alpha\right] \tag{4.36}$$

We can then use the chain rule and useful quantities to obtain

$$F^{i\pm} = -x^\pm\left(\mp\left[D^i, \alpha\right] + \frac{1}{\tau}\partial_\tau \alpha^i_\perp\right) \tag{4.37}$$

where equation (4.37) represents gauge fields and field strengths within the light cone. All αs present in the equation are part of the ansatz mentioned earlier. For pure light cone gauge fields and components, we have

$$F^{+-} = -F^{-+} = \partial^+ A^- - \partial^- A^+ \tag{4.38}$$

$$\Rightarrow F^{+-} = -\tfrac{1}{\tau}\partial_\tau(\tau^2 \alpha) \tag{4.39}$$

while the purely transverse coordinates give

$$F^{ij} = \partial^i \alpha^j_\perp - \partial^j \alpha^i_\perp - ig\left[\alpha^i_\perp, \alpha^j_\perp\right] \tag{4.40}$$

These require intricate steps to complete, which we will outline in detail in appendix A. Now that we have the general form of our gauge field strength tensor under wraps, we can find our EOMs. We will again segregate our steps between regions of spacetime, starting with the forward light cone, where the collision and all subsequent essential events occur. In the $x^\pm$ directions, we have

$$\left[D_\mu, F^{\mu\pm}\right] = 0 \tag{4.41}$$

$$\Rightarrow \partial_\mp F^{\mp\pm} - ig\left[A^\pm, F^{\mp\pm}\right] + \left[D_i, F^{i\pm}\right] = 0 \tag{4.42}$$

Explicitly converting to light-cone coordinates and inserting our colour gauge field strength tensor expressions, we find (once again for $x^\pm$)

$$-\left[D_i, \partial_\tau \alpha^i_\perp\right] - ig\tau^2\left[\alpha, \partial_\tau \alpha\right] \mp \tau\left[D^i, \left[D^i, \alpha\right]\right] \pm \partial_\tau\left(\frac{1}{\tau}\partial_\tau(\tau^2\alpha)\right) = 0 \tag{4.43}$$

Now, since our expressions for x^+ and x^- are similar, we can add and subtract them to give simpler results:

$$\begin{aligned}
\left[D_\mu, F^{\mu+}\right] + \left[D_\mu, F^{\mu-}\right] &= 0 && (4.44)\\
\Rightarrow ig\tau^2 \left[\alpha, \partial_\tau \alpha\right] + \left[D_i, \partial_\tau \alpha^i_\perp\right] &= 0 && (4.45)\\
\left[D_\mu, F^{\mu+}\right] - \left[D_\mu, F^{\mu-}\right] &= 0 && (4.46)\\
\Rightarrow \partial_\tau \left(\frac{1}{\tau}\partial_\tau(\tau^2\alpha)\right) - \tau\left[D^i, \left[D^i, \alpha\right]\right] &= 0 \iff && (4.47)\\
\frac{1}{\tau^3}\partial_\tau \tau^3 \partial_\tau \alpha - \left[D^i, \left[D^i, \alpha\right]\right] &= 0 && (4.48)
\end{aligned}$$

The last Yang-Mills equations written in terms of our initial colour gauge fields is

$$\left[D_\mu, F^{\mu i}\right] = 0 \tag{4.49}$$

After a few steps and a fair bit of cancellations, and using the expressions for our field strength tensor shown previously, we arrive to

$$\frac{1}{\tau}\partial_\tau \tau \partial_\tau \alpha^i_\perp - ig\tau^2\left[\alpha, \left[D^i, \alpha\right]\right] - \left[D^j, F^{ji}\right] = 0 \tag{4.50}$$

These are extremely useful. We now have equations describing our system after the collision in terms of the initial colour gauge fields, as described in our ansatz. We now have the boost invariant Yang-Mills equations of motion at our disposition. We use these equations to evolve our system passed its initial conditions and into the post-collision phase. Coupled to equations (4.27), (4.28), and (4.29), our system is now completely defined and can be evolved in time after the collision. We have therefore fully-developed the glasma spatiotemporally, starting from the initial gauge fields produced by our two nuclei pre-collision, to point of collision, and through the time after the collision.

We end this chapter with a quick discussion on the saturation scale Q_s and its relationship to our initial colour gauge fields via the colour charge density profiles it helps produce.

4.4 COLOUR CHARGE DENSITY

We have established that our large x partons acted as sources for our small x gluons. The large x valence partons radiate gluons via bremsstrahlung. However, as one might

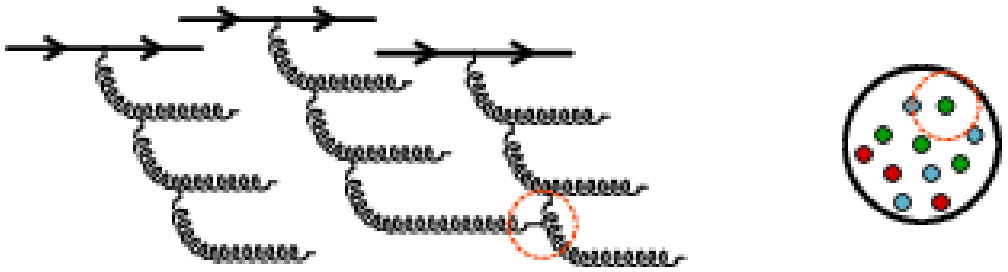

Figure 18: Gluon cascades from a valence quark in a hadron, circled in red. From [10].

have already foretold, this physical process becomes limited as more and more gluons are radiated.

Given that gluons can radiate other gluons, it would make sense for two gluons of the right colour charges to, sometimes, recombine into a single gluon. The saturation of a system occurs when the two processes outlined previously, namely gluon production and gluon recombination, compete on the same scale. Once the number of recombined gluons is comparable to the number of new gluons radiated in a given volume, we have reached *gluon saturation*. The momentum at which saturation occurs is given by

$$Q_s^2 = \frac{\alpha_s x G\left(x, Q^2\right)}{A^{2/3}} \tag{4.51}$$

One can obtain this equation by remarking that a sufficient condition for saturation would be that the product of the gluon recombination cross-section with the gluon surface density exceeds 1 [10, 17].

The saturation scale, however, is not a hard cap on gluon production. While saturation effects can be measured at energies lower than Q_s, gluon-gluon radiation is still a significant contributor at scales larger than Q_s. Fig. 18 shows a Feynman diagram that showcases both gluon radiation and recombination. Once the recombination probability equals the probability for further radiation, the system has reached saturation.

Q_s sets the energy below which the gluon density is limited and growth, limiting our colour charge density. In IP-Glasma, the colour charge density ρ and the saturation scale Q_s are related by a simple constant.

Up to $\tau = Q_s^{-1}$, solutions to the classical Yang-Mills equations describe our system accurately. However, after this time, the gluon density reduces greatly, and the classical fields do not represent the system accurately anymore. Since Q_s depends on the colli-

sion energy, the more energetic the collision, the longer our classical Yang-Mills field approximation will remain valid.

The MV model, which is central to the currently presented theoretical framework, also depends on a feature of Q_s. The feature in question is *geometric scaling* and states that the ratio of the transferred momentum in scattering processes to the saturation scale Q_s should be central to the cross-sections of such processes [16]. Geometric scaling's effect come into play if the area of a hadron involved in a process is much larger than the inverse of the saturation scale squared,

$$R^2 \gg Q_s^{-2} \tag{4.52}$$

If this condition is met, then the hadron's area, as "seen" by small x partons, will be effectively infinite. This practical infinity leads to all participating hadrons seemingly behaving in the same way on the scale of our small x partons.

Having finished our talk about classical fields, we must now explain how we liken the glasma to a fluid, via the stress-energy tensor.

5

FLOW IN THE GLASMA

As we have mentioned in the introduction to this thesis, we usually divide heavy-ion collision simulations into three stages: initial conditions, relativistic hydrodynamics, and hadronic cascade. While the transition from the purely hydrodynamic stage to the hadronic cascade stage is not the subject of this thesis, one might ask how we move from colour gauge fields evolving in the collision area to viscous, relativistic hydrodynamics. The critical element of such a transition is the stress-energy tensor, $T^{\mu\nu}$.

5.1 THE STRESS-ENERGY TENSOR

We will start by giving the form of the stress-energy tensor before explaining its different parts. [21] gives $T^{\mu\nu}$ for our glasma

$$T^{\mu\nu} = -g^{\nu\delta}g^{\rho\epsilon}g^{\mu\theta}F_{\theta\epsilon}F_{\delta\rho} + \frac{1}{4}g^{\mu\nu}g^{\alpha\lambda}g^{\beta\omega}F_{\lambda\omega}F_{\alpha\beta} \tag{5.1}$$

The $g^{\mu\nu}$s are our metric matrices and simply raise and lower the indices of our colour gauge field tensors. We can therefore take them out:

$$T^{\mu\nu} = -F^{a\mu\rho}F^{a\nu}_{\rho} + \frac{1}{4}g^{\mu\nu}F^{a\alpha\beta}F_{a\alpha\beta} \tag{5.2}$$

The first term in this equation can be re-written partly in terms of our colour gauge field A^a_μ

$$-F^{a\mu\rho}F^{a\nu}_{\rho} = -F^{a\mu\rho}\partial^{\nu}A^a_{\rho} - ig\left[A^b_{\rho}, F^{a\rho\mu}\right]A^{a\nu} + F^{a\mu\rho}\partial_{\rho}A^{a\nu} \tag{5.3}$$

Now, to backtrack further, we reiterate that the covariant derivative can be written $\partial_\rho = D_\rho + igA^b_\rho$, and that we are in the sourceless regime $\left[D_\rho, F^{a\mu\rho}\right] = 0$. This brings us to

$$T^{\mu\nu} = -F^{a\mu\rho}\partial^\nu A^a_\rho + \frac{1}{4}g^{\mu\nu}F^{a\alpha\beta}F^a_{\alpha\beta} + \partial_\rho\left(F^{a\mu\rho}A^{a\nu}\right) \tag{5.4}$$

We can then remove the total derivative $\partial_\rho F^{a\mu\rho}A^{a\nu}$, as done in [22]. This removal is valid because the 4-momentum, which we obtain by integrating the $T^{0\mu}$ component over all of space, is unchanged by a total derivative, which becomes a boundary term after integration by parts. We then have

$$T^{\mu\nu} = -F^{\mu\rho}\partial^\nu A_\rho + \frac{1}{4}g^{\mu\nu}F^{\alpha\beta}F_{\alpha\beta} \tag{5.5}$$

Recalling that our system, here, is sourceless, we have

$$\mathcal{L}_{CGC} = -\frac{1}{4}F^{a\mu\nu}F^a_{\mu\nu} \tag{5.6}$$

This fact leads us Noether's theorem. The conserved current associated with translational invariance, here, is our stress-energy tensor, and is given by

$$T^{\mu\nu} = \frac{\delta L}{\delta\left(\partial_\mu A^a_\rho\right)}\partial^\nu A^a_\rho - L\delta^{\mu\nu} \tag{5.7}$$

which matches equation (5.5).

Now that we have established the physical validity of our stress-energy tensor, we can look at the specifics of our 2+1D setting. To do so, we must first quickly dive into the specific form of our colour gauge field strength tensor. Given that we are only interested in a single mid-rapidity slice, our longitudinal colour gauge field will be a scalar field. To simplify things further, we can set the longitudinal chromo-electric field to the longitudinal colour gauge field's conjugate momentum. Furthermore, using the gauge $A^\tau = 0$, as outlined in [23], we obtain

$$F^{\mu\nu} = \begin{pmatrix} 0 & -\frac{E^x}{\tau} & -\frac{E^y}{\tau} & -\frac{\pi}{\tau} \\ \frac{E^x}{\tau} & 0 & F^{xy} & \frac{D_x\phi}{\tau^2} \\ \frac{E^y}{\tau} & F^{yx} & 0 & \frac{D_y\phi}{\tau^2} \\ \frac{\pi}{\tau} & -\frac{D_x\phi}{\tau^2} & -\frac{D_y\phi}{\tau^2} & 0 \end{pmatrix} \tag{5.8}$$

with ϕ being the scalar field describing the longitudinal colour gauge field, E^i being the chromo-electric field, π representing the conjugate momentum of ϕ, and D_i representing covariant derivatives. We can now return to our analysis of $T^{\mu\nu}$.

5.2 ENERGY, PRESSURE AND FLOW

The stress-energy tensor, while being a necessary element of transition towards the hydrodynamic phase, offers important information about the glasma. By diagonalizing $T^{\mu\nu}$, we can obtain the components of the pressure (in x, y and η) along with the energy density at a specific location. This key information allows us to evaluate pre-hydrodynamic quantities that are not experimentally measurable, which allows us to make predictions on observable results and other phenomenological analyses. Let us start by looking at the pressure components. Using equation (5.1), we have

$$T^{xx} = \text{tr}\left[-\frac{E_x^2}{\tau^2} + \frac{E_y^2}{\tau^2} + \pi^2 + (F^{xy})^2 + \frac{1}{\tau^2}(D_x\phi)^2 - \frac{1}{\tau^2}(D_y\phi)^2\right] \tag{5.9}$$

$$T^{yy} = \text{tr}\left[\frac{E_x^2}{\tau^2} - \frac{E_y^2}{\tau^2} + \pi^2 + (F^{xy})^2 - \frac{1}{\tau^2}(D_x\phi)^2 + \frac{1}{\tau^2}(D_y\phi)^2\right] \tag{5.10}$$

$$T^{\eta\eta} = \frac{1}{\tau^2}\,\text{tr}\left[\frac{E_x^2}{\tau^2} + \frac{E_y^2}{\tau^2} - \pi^2 - (F^{xy})^2 + \frac{1}{\tau^2}(D_x\phi)^2 + \frac{1}{\tau^2}(D_y\phi)^2\right] \tag{5.11}$$

These are the pressure components of our glasma, and include all of the elements present in $F^{\mu\nu}$. The last diagonal element of $T^{\mu\nu}$ is $T^{\tau\tau}$, which represents the energy density of the system. It is given by

$$T^{\tau\tau} = \text{Tr}\left[\frac{E_x^2}{\tau^2} + \frac{E_y^2}{\tau^2} + \pi^2 + (F^{xy})^2 - \frac{1}{\tau^2}(D_x\phi)^2 - \frac{1}{\tau^2}(D_y\phi)^2\right] \tag{5.12}$$

The energy density in the chromo-electric field is given by the first three terms, while the last three terms give the energy density in the chromo-magnetic field. The fact that τ^{-1} terms appear in this expression leads to an apparent singularity. Therefore, we start our analysis at $\tau > 0$

To determine the flow vector of our glasma at a specific location, we must dive a bit deeper into the procedure to determine $T^{\tau\tau}$. That is, a local eigenvalue/eigenvector equation

$$T^{\mu}_{\nu} u^{\nu} = a u^{\mu} \tag{5.13}$$

where u^{ν} represents the eigenvector associated to the eigenvalue a. If the eigenvalue and the norm of its associated eigenvector are both positive (i.e. the flow solution is time-like), we know that we have solved for the energy density ϵ, which in turn allows us to ascertain that the associated eigenvector is the glasma's flow velocity at that point. It must be made clear that, here, we are talking about energy flow - how the glasma's energy is propagating through the transverse plane - which is more subtle than typical flow descriptions. It is important to note that we normalize the obtained four-vector's norm to unity, i.e.

$$u^{\mu} u_{\mu} = g_{\mu\nu} u^{\mu} u^{\nu} = (u^{\tau})^2 - (u^{x})^2 - (u^{y})^2 - \tau^2 (u^{\eta})^2 = 1 \tag{5.14}$$

$$g_{\mu\nu} = \begin{pmatrix} 1 & 0 & 0 & 0 \\ 0 & -1 & 0 & 0 \\ 0 & 0 & -1 & 0 \\ 0 & 0 & 0 & -\tau^2 \end{pmatrix} \tag{5.15}$$

Figure 19 shows how the flow acts at different stages of the evolution of the glasma. At first, high energy densities across the interaction region limit the flow, leading to tiny flow vectors scattered across the transverse plane. However, as the energy diffuses, larger energy gradients tend to emerge. These eventually lead to flow, which is showcased by the largest flow vectors pointing from high energy density locations to low energy density locations. It is also clear that the glasma is flowing outwards and expanding, as

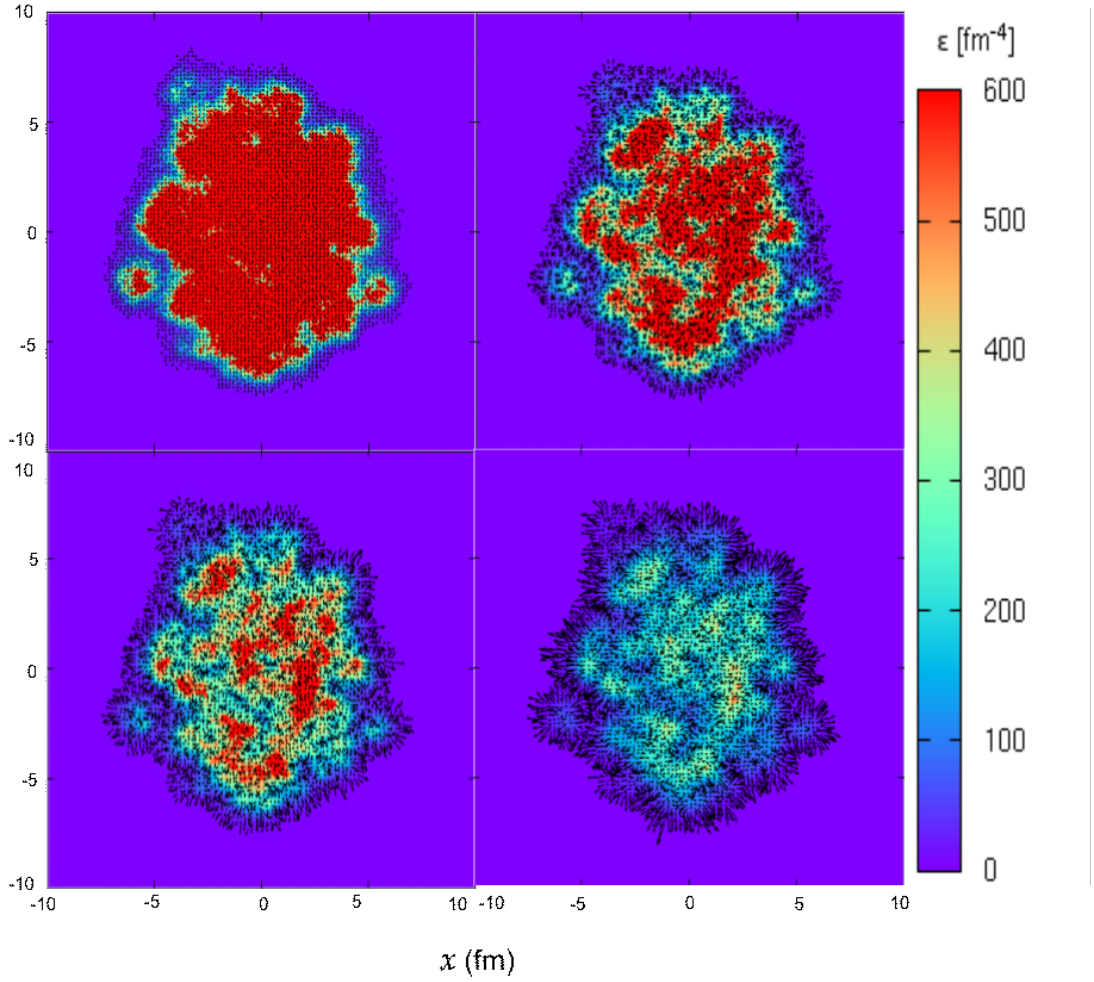

Figure 19: Four panels showing energy density and flow vectors at different stages of the glasma evolution. The time snapshots, going from left to right, then top to bottom, are at $\tau = 0.010, 0.037, 0.135$ and 0.401 fm/c.

it should. This is a satisfying and intuitive result enabled by the theoretical framework that we have outlined in this section of the thesis.

This significant consequence of the CGC and Glasma frameworks allows us to initialize the hydrodynamics stage of our simulation using flow velocities, which are not permitted by other initial conditions models. Obviously, given that our simulations are in 2+1D, the longitudinal flow is set to 0 throughout. It is, however, important to note that, throughout our calculations, the full 4x4 $T^{\mu\nu}$ is always used, meaning that the η-directional flow is *not* 0, and can sometimes be quite large. We ignore it in our subsequent steps because of our 2+1D, boost invariant approximation.

We are now ready to move on to the numerical implementation of this theoretical framework, and its produced results.

Part III

NUMERICAL STRUCTURE AND RESULTS

In this part, we provide details as to how we employ the general theoretical framework outlined previously in our simulations. We will, amongst other things, look at how we discretize the space, solve the initial fields numerically, and deal with gauge invariance. We will also be introducing a crucial component of our scheme: lattice QCD.

6

THE LATTICE

We will start our discussion on the numerical methods used in our simulations with the lattice, the spatial setting on which our glasma evolves. Using discretized space in simulations is necessary. However, it can be used to our advantage when it comes to QCD simulations, as we will see in this chapter. Let us start by looking at the parameters for our lattice.

6.1 THE SPACE

Technically, the lattice spacings should have units of length. However, as nuclear and particle physicists like to do, we make all length quantities, whether longitudinal or transverse, unitless. This transformation means that our length units are now *lattice units*. As we will see later on in this chapter, we can write many useful quantities in terms of our lattice spacing a using natural units. That is, by multiplying by appropriate factors of $\hbar$ and c, one can rewrite any result in terms of our lattice spacing a, which is measured in fm.

The size of the lattice spacing a affects the energy densities generated by our chromo-electric and chromo-magnetic fields within the lattice at early times. This effect can be seen in figure 20. While the differences in energy densities are wide at early times, they all converge to similar values later. In figure 20, $g^2\mu \approx 2\text{GeV}$, which means that the final time shown on the graph, $g^2\mu\tau = 3$, is $\tau \approx 0.25\text{fm}$, which is much earlier than the time at which we pass from IP-Glasma to relativistic hydrodynamics. This effect, while interesting, is, therefore, inconsequential. In this thesis, $N = 500$ and $a = 0.044$ fm ≈ 0.2 GeV^{-1}. However, as was outlined in chapter 5, energy density and glasma flow are both tightly related. Because the flow is obtained by diagonalizing $T^{\mu\nu}$, it is *more* sensitive to the grid size than ϵ, and pushes our grid parameters towards finer grids. We can use the

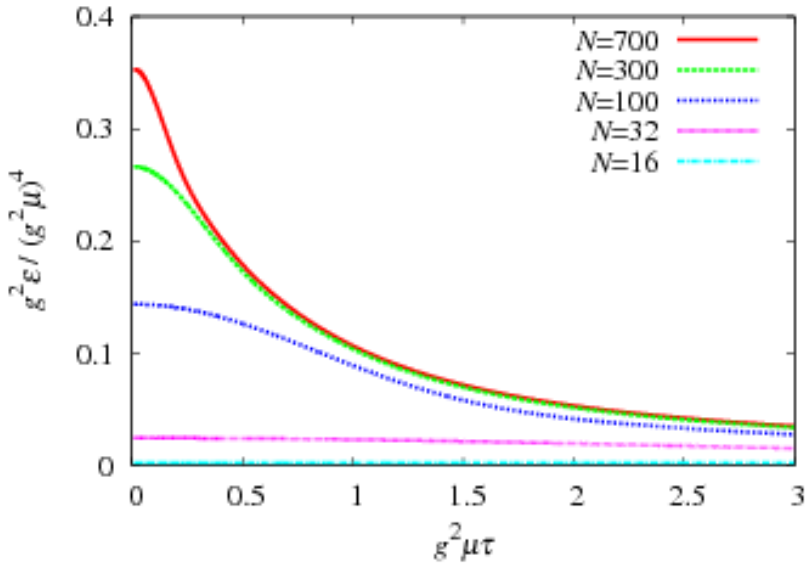

Figure 20: The energy density for various choices of transverse grid size N, averaged over more than 30 random configurations of the initial colour charge density to avoid any bias. Taken from [24]

.

saturation scale Q_s to determine an upper bound for our lattice spacing a. To be able to see and analyze gluons down to the saturation scale, we must have a grid size which takes this into consideration. Since, in the natural units, energy and distance are related by an inversion, we seek to have

$$a \leq Q_s^{-1} \tag{6.1}$$

At the energies relevant to our analysis, the maximum saturation scale should be around 0.5 GeV, which means that $a \leq 2$ GeV^{-1} is sufficiently small to resolve the important physics at hand. This upper bound puts our choice of lattice spacing well below the maximally allowed value.

Now that we have settled the basics, we must show how we will effectively use this lattice.

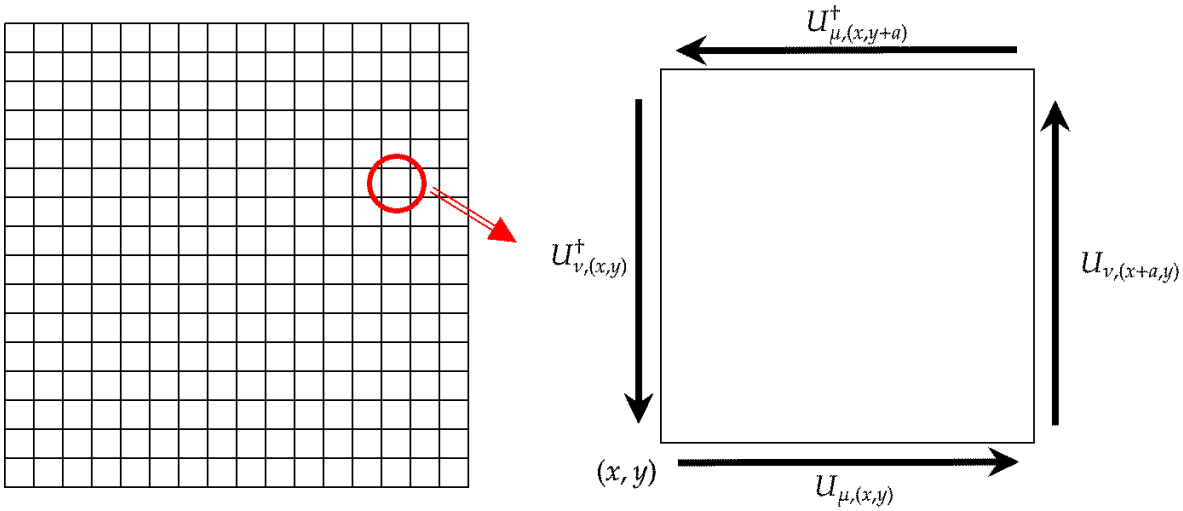

Figure 21: A lattice site at (x, y), taken from the entire lattice. Since this thesis only deals with 2+1 dimensional calculations, we only need to consider our lattice links in the transverse plane.

6.2 GAUGE THEORY ON THE LATTICE

This section will bank heavily on figure 21, which shows a Wilson loop, or *plaquette*, as a visual aid. Four Wilson lines, or links, make up each plaquette. A link serves to transport gauge fields from one lattice site to another. Figure 21 pictorially shows that, while a link U transports information in the positive x or y direction, its hermitian conjugate $U^{\dagger}$ transports information in the opposite direction, a very clever and useful mathematical tool.

Now - the theoretical considerations of Part II stated equations that relied on continuous spatial variables. We can not use continuous spatial variables on our lattice. However, each lattice site offers information regarding the colour gauge fields within the boundaries traced by its links! How do we, then, reconstruct the values of our colour gauge fields inside of our plaquettes?

We start by defining the link at point $\boldsymbol{x}$ and discretizing it by expanding about small variations (in this case, our lattice spacing a):

$$U_\mu(x) = \exp\left\{igaA^a_\mu(x)t^a\right\} \tag{6.2}$$

$$U_\mu = 1 + igaA^a_\mu t^a - \frac{1}{2}g^2a^2A^a_\mu A^b_\mu t^a t^b + O\left(a^3\right) \tag{6.3}$$

As stated previously, we use links to transport quantities from lattice site to lattice site. We can chain such transport actions together by multiplying links with adjacent links. Therefore, looping around the plaquette and back to our lattice site (x, y) in figure 21, we have

$$U_{\mu\nu} = U_\mu(x)U_\nu(x + a\hat{\mu})U^\dagger_\mu(x + a\hat{\nu})U^\dagger_\nu(x) \tag{6.4}$$

$$U_{\mu\nu} = 1 + iga\left(A_\mu(x) + A_\nu(x + a\hat{\mu}) - A_\mu(x + a\hat{\nu}) - A_\nu(x)\right) \tag{6.5}$$

$$U_{\mu\nu} = 1 + iga^2\left(\partial_\mu A_\nu - \partial_\nu A_\mu\right) \tag{6.6}$$

Where, in the second step, we have kept only terms to linear order in our lattice spacing and, in the third step, we have used the fact that, on the lattice, we calculate derivatives by subtracting the values of functions at adjacent lattice sites and dividing by the lattice spacing. This explains why, while we keep our terms to first order in a, we have an a^2 term leading equation (6.6). If we now look at terms stemming from equation (6.4), but only keeping terms quadratic in a, we will have

$$\begin{aligned} U_{\mu\nu} = & -g^2a^2\left(A_\mu A_\mu + A_\nu A_\nu + A_\mu A_\nu - A_\mu A_\mu\right. \\ & \left. -A_\mu A_\nu - A_\nu A_\mu - A_\nu A_\nu + A_\mu A_\nu\right) \end{aligned} \tag{6.7}$$

$$U_{\mu\nu} = -g^2a^2\left[A_\mu, A_\nu\right] \tag{6.8}$$

Combining equations (6.6) and (6.8) gives

$$U_{\mu\nu} = 1 + iga^2\left(\partial_\mu A_\nu - \partial_\nu A_\mu\right) - g^2a^2\left[A_\mu, A_\nu\right] \tag{6.9}$$

The last two terms can clearly be combined and simplified into $F_{\mu\nu}$ such that

$$U_{\mu\nu} = 1 + iga^2F_{\mu\nu} \approx \exp\left(iga^2F_{\mu\nu}\right) \tag{6.10}$$

$$U^\dagger_{\mu\nu} = 1 - iga^2F_{\mu\nu} \approx \exp\left(-iga^2F_{\mu\nu}\right) \tag{6.11}$$

where equation (6.11) represents us circling the plaquette in the opposite direction.

This result may look inconsequential at first, but is quite powerful. In these plaquettes lie the values of our gauge field strength, which is, as we have established before, at heart of most of the quantities important to the framework. As an example, let us take the trace of the difference between a plaquette $U_{\mu\nu}$ and its Hermitian conjugate $U^{\dagger}_{\mu\nu}$,

$$i \operatorname{Tr}\left[\left(U^{\dagger}_{\mu\nu} - U_{\mu\nu}\right) t^{a}\right] \approx g a^{2} F^{a}_{\mu\nu} + \mathrm{O}(a^{6}) \tag{6.12}$$

where t^a is a Gell-Mann matrix. By multiplying this trace by a second identical trace, we obtain F^2. This calculation is precise to order a^4, which is satisfying and useful.

Let us now outline, in more detail, the forms taken by other quantities on the lattice.

6.3 USEFUL QUANTITIES ON THE LATTICE

All steps regarding quantities on the lattice are taken from [23] and [25].

We will begin by looking at the initial conditions of our simulation, that were discussed in chapter 4, on the lattice. This concerns our system at $\tau = 0$. Using the tricks shown in the previous section, we formulate the initial conditions as as

$$\operatorname{Tr}\left[t^{a}\left(\left(U_{i}^{(A)} + U_{i}^{(B)}\right)\left(1 + U_{i}^{\dagger}\right) - \left(U_{i}^{(A)} + U_{i}^{(B)}\right)\left(1 + U_{i}^{\dagger}\right)^{\dagger}\right)\right] = 0 \tag{6.13}$$

where, we have replaced (x, y) with the simple index i. Given that our lattice is equally spaced, we can easily track the entire lattice space using a single index.

We will also take

$$\phi = 0 \tag{6.14}$$

$$E^{i} = 0 \tag{6.15}$$

$$\begin{aligned} \pi\left(\boldsymbol{x}_{\perp}\right) = \frac{-i}{4g} \sum_{i} \Big[& \left(U_{i}\left(\boldsymbol{x}_{\perp}\right) - 1\right)\left(U_{i}^{\dagger(B)}\left(x_{\perp}\right) - U_{i}^{\dagger(A)}\left(\boldsymbol{x}_{\perp}\right)\right) \\ & + \left(U_{i}^{\dagger}\left(\boldsymbol{x}_{\perp} - \hat{\boldsymbol{i}}\right) - 1\right)\left(U_{i}^{(B)}\left(\boldsymbol{x}_{\perp} - \hat{\boldsymbol{i}}\right) - U_{i}^{(A)}\left(\boldsymbol{x}_{\perp} - \hat{\boldsymbol{i}}\right)\right) - \text{h.c.}\Big] \end{aligned} \tag{6.16}$$

where we have used the shorthand h.c. to designate the hermitian conjugate of the previous group of terms. The $\hat{\boldsymbol{\imath}}$ represent the unit vectors aligned with our lattice, and we are summing over their two possible directions (x and y). Equation (6.16) is analogous to the solution to our ansatz α.

We can easily show that equation (6.13) solves our continuous initial conditions. Expanding the exponential in U_i, and keeping track of the colour gauge fields for each nucleus, we have

$$\begin{aligned} &\mathrm{Tr}\left\{t^a\left[\left(2+iga\left(A_i^{(A)}+A_i^{(B)}\right)\right)(2-igaA_i)\right.\right. \\ &\left.\left.-\left(2-ig\left(aA_i^{(A)}+A_i^{(B)}\right)\right)(2+igaA_i)\right]\right\}=0 \end{aligned} \tag{6.17}$$

Keeping only terms linear in a, we have

$$\mathrm{Tr}\left\{t^a\left[\left(4+2iga\left(A_i^{(A)}+A_i^{(B)}\right)-2igaA_i\right)-\left(4-2iga\left(A_i^{(A)}+A_i^{(B)}\right)+2igaA_i\right)\right]\right\} \tag{6.18}$$

$$\mathrm{Tr}\left\{t^a\left[4iga\left(A_i^{(A)}+A_i^{(B)}\right)-4igaA_i\right]\right\}=0 \tag{6.19}$$

$$\Rightarrow A_i=A_i^{(A)}+A_i^{(B)} \tag{6.20}$$

which is what we wanted to show. We can repeat this procedure for the other defining equations of our initial conditions.

Now that we have ensured that our initial conditions are easily transferrable to the lattice, we can look at the equations of motion derived in chapter 4. We start by writing the Yang-Mills Hamiltonian in 2+1 dimesions:

$$H=\int d\boldsymbol{x}_\perp\eta\left(\frac{1}{2\tau}E_i^aE_i^a+\frac{\tau}{4}F_{ij}^aF_{ij}^a+\frac{1}{2\tau}\left(D_i\phi\right)^a\left(D_i\phi\right)^a+\frac{\tau}{2}E_\eta^aE_\eta^a\right) \tag{6.21}$$

We note that our choice of gauge makes it so that the longitudinal colour gauge field A_η is a scalar field ϕ, which leads to our chromo-electric fields having the following forms:

$$E_a^\eta = \frac{1}{\tau}\partial_\tau A_\eta^a=\pi \tag{6.22}$$

$$E_a^i = \tau\partial_\tau A_i^a \tag{6.23}$$

where we have reiterated that the longitudinal chromo-electric field is set as the conjugate momentum of our scalar field ϕ. We can then use the Hamiltonian density $\mathcal{H}$ and discretize it, to obtain

$$\begin{aligned}\mathcal{H} &= \sum_{x_\perp}\left(\frac{g^2}{\tau}\operatorname{Tr}\left(E^iE^i\right)+\frac{2N_c\tau}{g^2a^2}\left(1-\frac{1}{N_c}\operatorname{Re}\left(\operatorname{Tr}\left(U_{xy}\right)\right)\right)\right. \\ &\left.+\frac{\tau}{a^2}\operatorname{Tr}\left(\pi^2\right)+\frac{1}{\tau}\sum_i\operatorname{Tr}\left(\phi-\tilde{\phi}_i\right)^2\right)\end{aligned} \tag{6.24}$$

This is reminiscent of our energy density $T^{\tau\tau}=\epsilon$, presented in chapter 5, in that it combines contributions due to the chromo-electric and chromo-magnetic fields. N_c designates the number of different colour charges in our theory, which is 3. Also, the scalar field ϕ can be *transported* using our gauge links U_i, giving rise to $\tilde{\phi}_i$, which is the scalar field transported from the lattice site of ϕ into the direction i. U_{xy} designates the plaquette in the transverse plane, as shown previously. At initial times, all of our energy is stored in longitudinal fields only, which means

$$\epsilon(\tau=0) = \frac{2}{g^2a^4}\left(N_c-\operatorname{Re}\left(\operatorname{Tr}\left(U_{xy}\right)\right)\right)+\frac{1}{a^4}\operatorname{Tr}\left(\pi^2\right) \tag{6.25}$$

which is calculated and presented in [26]. We can a combination of similar procedures and Poisson brackets to obtain the discretized equations of motion for our fields, which are given by

$$\dot{E}^x = \tfrac{i\tau}{2g^2}\left[U_{xy}+U_{x(-y)}-U_{xy}^\dagger-U_{x(-y)}^\dagger\right]-\text{trace}+\tfrac{\mathrm{i}}{\tau}\left[\tilde{\phi}_\mathrm{x},\phi\right] \tag{6.26}$$

$$\dot{E}^y = \tfrac{i\tau}{2g^2}\left[U_{yx}+U_{y(-x)}-U_{yx}^\dagger-U_{y(-x)}^\dagger\right]-\text{trace}+\tfrac{\mathrm{i}}{\tau}\left[\tilde{\phi}_\mathrm{y},\phi\right] \tag{6.27}$$

$$\dot{U}_i = i\tfrac{g^2}{\tau}E^iU_i \tag{6.28}$$

$$\dot{\phi} = \tau\pi \tag{6.29}$$

$$\dot{\pi} = \tfrac{1}{\tau}\textstyle\sum_i\left[\tilde{\phi}_i+\tilde{\phi}_{-i}-2\phi\right] \tag{6.30}$$

where, in equations (6.26) and (6.27), we are making the plaquette matrices traceless. How to discretize and evolve these equations temporally will be the subject of section 6.5. For now, let us quickly look at how we deal with the stress-energy tensor on the lattice.

This part will exclude many long-form equations, which we will show in the appendix B instead. Their derivations follow the techniques outlined previously in this thesis. We treat the transverse electric fields E_{xy} slightly differently. Instead of defining them at lattice sites, we define them at the centre of our plaquettes. That is, if we have a plaquette at the lattice site (x, y), as in figure 21, we want the electric field at $(x + \frac{a}{2}, y + \frac{a}{2})$. However, this adds a different element of complexity, which is that two neighbouring lattice sites now contribute equally to our electric field in the middle of certain plaquettes. Defining E_{xy} means that we must also define our stress-energy tensor at the same location since it relies on the electric field's value. Now, let

$$E^2_{xy}(i) = \tfrac{g^2}{2\tau^2} \operatorname{Tr}\left[E^{x2}_i + E^{x2}_{i+a} + E^{y2}_i + E^{y2}_{i+a}\right] \tag{6.31}$$

$$E^2_{\eta}(i) = \tfrac{1}{4} \operatorname{Tr}\left[\pi^2_i + \pi^2_{i+a} + \pi^2_{i+a} + \pi^2_{i+a_x+a_y}\right] \tag{6.32}$$

$$B^2_y(i) = \tfrac{1}{2\tau^2} \operatorname{Tr}\left[\left(\phi_i - U_{x,i}\phi_{i+a}U^\dagger_{x,i}\right)^2 + \left(\phi_{i+a} - U_{x,i+a}\phi_{i+a_x+a_y}U^\dagger_{x,i+a}\right)^2\right] \tag{6.33}$$

$$B^2_x(i) = \tfrac{1}{2\tau^2} \operatorname{Tr}\left[\left(\phi_i - U_{y,i}\phi_{i+a}U^\dagger_{y,i}\right)^2 + \left(\phi_{i+a} - U_{y,i+a}\phi_{i+a_x+a_y}U^\dagger_{y,i+a}\right)^2\right] \tag{6.34}$$

$$B^2_\eta(i) = \left[-\tfrac{i}{2g}\left(U_{x,i}U_{y,i+a}U^\dagger_{x,i+a}U^\dagger_{y,i} - U_{y,i}U_{x,i+a}U^\dagger_{y,i+a}U^\dagger_{x,i} - \text{trace}\right)\right]^2 \tag{6.35}$$

where a_x and a_y are to indicate that we are looking at a lattice point one x lattice and one y lattice spacing a away. Equation (6.35) stems directly from equation (6.12). From these expressions, we can write the stress-energy tensor's diagonal elements rather simply

$$T^{xx} = E^2_{xy} + E^2_\eta - B^2_x + B^2_y + B^2_\eta \tag{6.36}$$

$$T^{yy} = E^2_{xy} + E^2_\eta + B^2_x - B^2_y + B^2_\eta \tag{6.37}$$

$$T^{\eta\eta} = E^2_{xy} - E^2_\eta + B^2_x + B^2_y - B^2_\eta \tag{6.38}$$

$$T^{\tau\tau} = E^2_{xy} + E^2_\eta + B^2_x + B^2_y + B^2_\eta \tag{6.39}$$

which leaves $T^{\mu\nu}$ traceless. Due to the stress-energy tensor's symmetry, only six of the 12 remaining elements (excluding the diagonal elements that we have just outlined) need to be determined. These, as mentioned previously, can be found in appendix B.

We now begin a quick yet crucial discussion on the specific algorithms used to solve and evolve the initial fields on the lattice.

6.4 SOLVING THE INITIAL FIELDS

We want to solve

$$\mathrm{Tr}\left[t^a\left(\left(U_i^{(A)}+U_i^{(B)}\right)\left(1+U_i^{\dagger}\right)-\left(U_i^{(A)}+U_i^{(B)}\right)\left(1+U_i^{\dagger}\right)^{\dagger}\right)\right]=0 \tag{6.40}$$

which was the initial condition outlined in the previous chapter. We will follow the procedure developed by Marius Cautun, Francois Fillion-Gourdeau, and Sangyong Jeon in [27], without going into too much details.

Now, equation (6.40) presents a system of 8 equations to solve (one for each SU(3) group generator). Because of its non-linearity and complexity, we must solve this system iteratively.

Even though we know our solution will not be Abelian, we start off by taking the following ansatz for our solution at a given lattice site:

$$U_i = U_i^{(A)}U_i^{(B)} \iff \tag{6.41}$$

$$U^{(3)} = U^{(1)}U^{(2)} \tag{6.42}$$

We insert it into equation (6.40) to obtain

$$\mathrm{ReTr}\left[t_a\left(U^{(1)}+U^{(2)}\right)\left(1+U^{(3)\dagger}\right)\right]=f_a \tag{6.43}$$

where f_a is a small numerical quantity that we want to take to 0. We can write

$$U^{(3)}_{\text{current}} = e^{i\alpha x_a t_a}U^{(3)}_{\text{previous}} \tag{6.44}$$

$$U^{(3)}_{\text{current}} \approx \left(1+i\alpha x_a t_a\right)U^{(3)}_{\text{previous}} \tag{6.45}$$

where $U^{(3)}_{\text{previous}}$ designates the previous iteration's guess and α is a constant chosen to ensure convergence. If we require that our newest guess solve equation (6.40), we obtain

$$\alpha x_b\,\mathrm{Im\,Tr}\left[t_b t_a\left(U^{(1)}+U^{(2)}\right)U^{(3)\dagger}_{previous}\right]=-f_a \tag{6.46}$$

which we solve for x_b. This gives us $U^{(3)}_{\text{current}}$ via equation (6.44), which we plug back into (6.40) to give us our new f_a, f'_a. If we look at the Taylor expansion of the exponential in equation (6.44), we find that

$$f'_a = -\frac{\alpha^2}{2} x_b x_c \,\text{Re}\,\text{Tr}\left[t_b t_c t_a \left(U^{(1)} + U^{(2)}\right) U^{(3)\dagger}_{previous}\right] \tag{6.47}$$

If we stray away from our lattice and into the continuum limit, our links become unit matrices, which leads to

$$f'_a = -\frac{\alpha^2}{2} f_b f_c \,\text{Tr}\left[\{t_a, t_b\}\, t_c\right] \tag{6.48}$$

Even though we have taken the continuum limit leading up to this result, we still expect that f_a should remain proportional t $f_b f_c$ on our lattice. We also expect that $|f'_a| < f_a$, which means that, by iterating this process enough times, f_a should reach 0, and we should be left with $U^{(3)}$, our solution. If we do not move towards smaller values of f_a after approximately 20 tries, we use another algorithm, SAM, which improves our initial guess for $U^{(3)}$, and we move from there.

6.5 TEMPORAL EVOLUTION

We now look at how we solve key differential equations in time, such as equations (6.26)-(6.30), using the Leap Frog algorithm. The algorithm follows a similar procedure by evolving derivatives at times halfway between the time steps of the quantities themselves, and thus the quantity and its derivative successively leap over one another, but are never at the same time. In general, for a quantity x, its first time derivative v, and second derivative a,

$$x(\tau + d\tau) = x(\tau) + v(\tau + d\tau/2)d\tau \tag{6.49}$$

$$v(\tau + d\tau/2) = v(\tau - d\tau/2) + a(\tau)d\tau \tag{6.50}$$

We can apply this procedure to equations (6.26)-(6.30) to obtain (in order)

$$E^x(x,\tau+d\tau/2) = \; = E^x(x,\tau-d\tau/2) + i\frac{\left(\tau+\frac{d\tau}{2}\right)d\tau}{2g^2}\left(U_{xy}+U_{x-y}\right. \tag{6.51}$$
$$\left. - \text{ h.c. } - \text{trace}\right) + i\frac{d\tau}{\left(\tau+\frac{d\tau}{2}\right)}\left[\tilde{\phi}_x,\phi\right]$$

$$E^y(x,\tau+d\tau/2) = E^y(x,\tau-d\tau/2) + i\frac{\left(\tau+\frac{d\tau}{2}\right)d\tau}{2g^2}\left(U_{yx}+U_{y-x}\right. \tag{6.52}$$
$$\left. -\text{h.c.} - \text{trace}\right) + i\frac{d\tau}{\left(\tau+\frac{d\tau}{2}\right)}\left[\tilde{\phi}_y,\phi\right]$$

$$U_i(x.\tau+d\tau) = \exp\left(i\frac{g^2 d\tau}{\left(\tau+\frac{d\tau}{2}\right)}E^i\left(\tau+\frac{d\tau}{2}\right)\right)U_i(\tau) \tag{6.53}$$

$$\phi(x,\tau+d\tau) = \phi(x,\tau) + \frac{\tau+\frac{d\tau}{2}}{d\tau}\pi\left(x,\tau+\frac{d\tau}{2}\right) \tag{6.54}$$

$$\pi(x,\tau+d\tau/2) = \pi(x,\tau-d\tau/2) + \frac{d\tau}{\left(\tau+\frac{d\tau}{2}\right)}\sum_i\left(\tilde{\phi}_i+\tilde{\phi}_{-i}-2\phi\right) \tag{6.55}$$

Note that the last three equations above would involve division by τ, which would cause clear issues for $\tau = 0$. For this reason $\frac{1}{\tau}$ is replaced by $\frac{d\tau}{\left(\tau+\frac{d\tau}{2}\right)}$ which equals $1/2$ for $\tau = 0$. This introduces some error but prevents these terms from blowing up at initial time. For large τ this expression has the same behaviour as $\frac{1}{\tau}$. Furthermore, because, as mentioned, the momenta (derivatives) E^i and π are stored at $\tau - \frac{d\tau}{2}$, while ϕ and U_i are stored at τ, the derivatives will always lag behind the fields by half of a time step. This method is the so-called leapfrog algorithm. At the end of the simulation, derivatives are evolved by an additional half time step to bring all quantities to the same value of τ. The leapfrog algorithm has an error of order $d\tau^2$ at each step.

This concludes this important part of the thesis and precludes our discussion regarding colour charge density sampling and saturation scale determination.

7

STOCHASTIC PROCESSES

This chapter will outline how we determine the saturation scale for each nucleus and how we generate our colour charge distribution. These steps are all taken within the IP-Sat model. The last section will be a quick overview of the IP-Jazma framework used to guide more complex calculations in this thesis.

7.1 FINDING THE SATURATION SCALE

Determining the saturation scale is done through the IP-Sat model, which stands for "Impact Parameter Dipole Saturation model" [1]. The information presented in this section is but a condensed version of [1]. We start by looking at the cross-section for a $q\bar{q}$ to pass through a dilute gluon cloud. This quantity is proportional to the strong coupling α_s, the quark-antiquark dipole's area, and the number of gluons in the cloud. This readily gives

$$\sigma_{q\bar{q}} = \frac{\pi^2}{N_c} r^2 \alpha_s \left(\mu^2\right) xg\left(x, \mu^2\right) \tag{7.1}$$

where $\frac{xg(x,\mu^2)}{N_c}$ represents the gluon density at a specific momentum fraction x, per colour charge. It is important to reiterate that α_s and g are both scale-dependent, as mentioned in the introduction to this thesis, which is why both present μ^2 dependence, with μ being a scale parameter. Now, take a single proton. If we assume that the quark-antiquark pairs form a dense enough cloud (which is in line with what the CGC framework prescribes), then the probability for a $q\bar{q}$ dipole to not undergo an inelastic interaction is given by

$$|S(b)|^2 = \exp\left\{-\frac{\pi^2}{N_c} r^2 \alpha_s \left(\mu^2\right) xg\left(x, \mu^2\right) \int dz \rho(b, z)\right\} \tag{7.2}$$

where $\rho(b, z)$ is the gluon density inside the proton, and we are integrating over the longitudinal extent of the proton. Now, taking

$$\int dz\rho(b,z) = T(b) = \frac{1}{2\pi B_G}\exp\left(-b^2/2B_G\right) \tag{7.3}$$

we can write the differential cross-section thanks to the impact parameter dependence introduced in $T(b)$:

$$\frac{d\sigma_{\bar{q}q}}{d^2b} = 2\left[1-\exp\left(-\frac{\pi^2}{2N_c}r^2\alpha_s\left(\mu^2\right)xg\left(x,\mu^2\right)T(b)\right)\right] \tag{7.4}$$

It is important to note that, here, the impact parameter b represents the *proton* impact parameter, and not the nucleus impact parameter described in chapter 2. The parameter B_G found in $T(b)$ is obtained by fitting to HERA diffractive data. For a given dipole size, the cross-section will plateau at a particular value of b. As we increase the dipole size, the corresponding value for b increases as well. We initialize the gluon density distribution at a given scale ($\mu_0^2 = 1$ GeV^2) as

$$xg\left(x,\mu_0^2\right) = A_g x^{-\lambda_g}(1-x)^{5.6} \tag{7.5}$$

with the values of A_g and λ_g coming from fits to experimental scattering data. We calculate the individual momentum fraction x of partons using the average transverse momentum as a function of collision energy reported by CMS [28]

$$\langle p_T\rangle = 0.413 - 0.0171\ln(s) + 0.00143(\ln(s))^2 \tag{7.6}$$

Finally, we take strong coupling as a function of scale to be

$$\alpha_s\left(\mu^2\right) = \frac{12\pi}{\left(33-2N_f\right)\ln\left(\mu^2/\Lambda^2_{QCD}\right)} \tag{7.7}$$

with $\Lambda_{QCD} = 200$ MeV and $N_f = 3$. We evolve the equations using the DGLAP (Dokshitzer-Gribov-Lipatov-Altarelli-Parisi) equations [29, 30],

$$\frac{\partial xg\left(x,\tilde{\mu}^2\right)}{\partial\log\tilde{\mu}^2} = \frac{\alpha_S\left(\tilde{\mu}^2\right)}{2\pi}\int_x^1 dzP_{gg}(z)\frac{x}{z}g\left(\frac{x}{z},\tilde{\mu}^2\right) \tag{7.8}$$

$$\text{where}\quad P_{gg}(z) = 6\left[\frac{z}{(1-z)}+\frac{1-z}{z}+z(1-z)\right]+\left(\frac{11}{2}-\frac{N_f}{3}\right)\delta(1-z) \tag{7.9}$$

In IP-Glasma, we take the saturation radius r_s to be the dipole size for which the proton becomes one interaction's length. This assumption sets a requirement on the exponent in equation (7.4), namely

$$\left(\frac{\pi^2}{2N_c} r^2 \alpha_s\left(\mu^2\right) xg\left(x, \mu^2\right) T(b)\right)\Big|_{r=r_s} = \frac{1}{2} \tag{7.10}$$

Solving this using Brent's method, outlined in section A.3, we can find the saturation radius, which can easily be related to the saturation scale for a single proton via

$$Q_{s,p}^2 = \frac{2}{r_s^2} \tag{7.11}$$

We then compute the saturation scale for each nucleus by summing the contribution from each nucleon at a given point in the transverse plane. This sum depends on the spatial distribution of nucleons discussed in chapter 2, and is related to the colour charge density via [1]

$$Q_s^2\left(x, \boldsymbol{b}_\perp\right) = C g^2 \mu^2\left(x, \boldsymbol{b}_\perp\right) \tag{7.12}$$

where this is for a single nucleus, C is a proportionality constant we use to fit overall energy densities, and $g^2\mu^2$ represents the colour charge per unit area. That is, g and μ are treated as a single quantity, given that g depends on μ, as seen in equation (7.4). In this thesis, we use $C = 0.5$.

An important caveat to the method we have outlined here is that it uses a constant momentum fraction x, which is entirely determined by the collision energy. However, physically, it would be more realistic to have each gluon have a specific momentum share, determined by its position in the transverse plane and related to the saturation scale. Therefore, following techniques outlined in [31], we define

$$x(\boldsymbol{x}_\perp) = \frac{Q_s(\boldsymbol{x}_\perp)}{\sqrt{s}} \tag{7.13}$$

along with a total thickness function for the whole nucleus (instead of individual nucleons)

$$T_{\text{total}}(b) = \sum_{i=1}^{A} T_i(b) \tag{7.14}$$

where A is the total number of nucleons in our given nucleus. We insert this definition into equation (7.4) to give

$$\frac{d\sigma_{\bar{q}q}}{d^2b} = 2\left[1 - \exp\left(-\frac{\pi^2}{2N_c} r^2 \alpha_s\left(\mu^2\right) xg\left(x, \mu^2\right) \sum_{i=1}^{A} T(b)\right)\right] \tag{7.15}$$

This leads to apparent complications, such as the fact that x now depends on Q_s. To circumvent this barrier, we initialize our system using the x calculated via equation (7.6). We then solve iteratively for Q_s and x until our solution converges. We then finally arrive at a distribution for our colour charges in the transverse plane.

7.2 COLOUR CHARGE DISTRIBUTION

We use equation (7.12) to determine the surface colour charge density of each nucleus. Following the MV and CGC models, we have the following distribution of colour charge for a nucleus moving in the positive z direction

$$W[\rho] = \exp\left\{-\int d^2\boldsymbol{x}_\perp \frac{\rho^2\left(x^-, \boldsymbol{x}_\perp\right)}{2\mu^2\left(x^-, \boldsymbol{x}_\perp\right)}\right\} \tag{7.16}$$

where μ is the local charge density in the transverse plane, as obtained via equation (7.12), and which [12] describes in detail. We then sample the colour charge squared per unit area from the Gaussian (7.16), through

$$\left\langle \rho^a\left(x^-, \boldsymbol{x}_\perp\right) \rho^b\left(x^-, \boldsymbol{y}_\perp\right)\right\rangle = g^2 \delta^{ab} \delta\left(\boldsymbol{x}_\perp - \boldsymbol{y}_\perp\right) \mu^2 \tag{7.17}$$

which we can discretize on the lattice via

$$\left\langle \rho_k^a\left(\boldsymbol{x}_\perp\right) \rho_l^b\left(\boldsymbol{y}_\perp\right)\right\rangle = \delta^{ab} \delta^{kl} \delta\left(\boldsymbol{x}_\perp - \boldsymbol{y}_\perp\right) \frac{g^2 \mu^2}{N} \tag{7.18}$$

with the indices $k, l = 1...N$ representing discretized longitudinal coordinates, which we have chosen to be 10. We recognize the general colour indices a and b which run from 1 to $N_c^2 - 1$. Also, $\boldsymbol{x}_\perp$ and $\boldsymbol{y}_\perp$, which are the positions of the charges in the transverse plane. Even though our simulations are run in 2+1 dimensions, a finite width in the x^- direction is necessary to avoid singularities. Taking N slices in the longitudinal direction corresponds to averaging over N colour charge configurations. This averaging picture implies that the saturation scale and colour charge distributions depend on N to some extent, with $N = 10$ being sufficient to ensure convergence. Using equation (7.12), we can relate the saturation scale to our charge distribution as follows

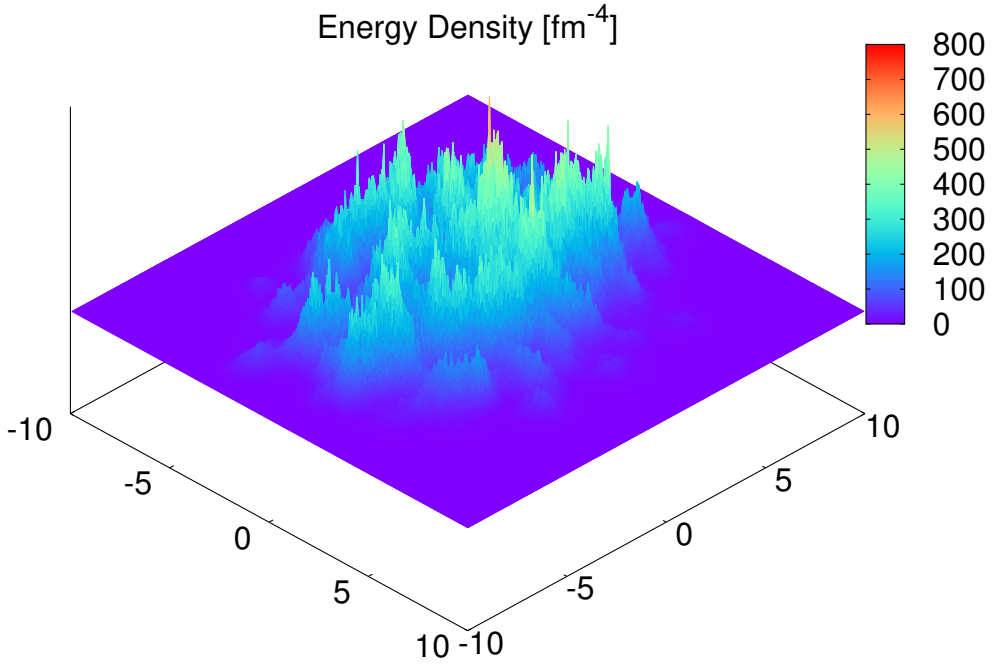

Figure 22: Contour plot of the energy density in the transverse plane for an ultra-central event ($b = 0$fm) at 193 GeV and $\tau = 0.4$ fm. The spikes are a unique feature of IP-Glasma.

$$\left\langle \rho_k^a\left(\boldsymbol{x}_\perp\right) \rho_l^b\left(\boldsymbol{y}_\perp\right)\right\rangle = \delta^{ab}\delta^{kl}\delta\left(\boldsymbol{x}_\perp - \boldsymbol{y}_\perp\right)\frac{Q_s^2}{CN_z} \tag{7.19}$$

Because of colour confinement, the expectation value of all colour charges should vanish. In other words, our sampled system should remain colour-neutral. However,

equation (7.19) describes fluctuations in the colour charge densities on time scales much longer than the collision time. These fluctuations are on length scales of order Q_s^{-1}, leading to bumps of colour charge on each incoming sheet of colour glass. This is in contrast to purely geometric models, such as the Glauber model, which lead to smooth initial states. This is a trademark of IP-Glasma and can be seen in figure 22.

7.3 IP-JAZMA

Full IP-Glasma calculations can be rather computationally intensive and, therefore, time-consuming. To guide our quest for results, we use frameworks which skip long steps (such as glasma time evolution). These frameworks help identify interesting data avenues quickly, which allows us to focus our intensive calculations on systems and parameters which are promising. These quicker frameworks do not, however, replace attempts at complete physical descriptions of our systems such as IP-Glasma. Therefore, final results in this thesis should always be understood as having been obtained through a complete initial conditions (IP-Glasma), relativistic hydrodynamics (MUSIC) and hadronic cascade (UrQMD) simulation.

IP-Jazma is one such framework. It is a simplified version of IP-Glasma. It is based upon Nagle and Zajc's paper [32] and has been a useful phenomenological tool since its inception. The main assumption made by IP-Jazma, based on results from [33], is that the energy density ε at initial time is proportional the product of the saturation scale squared of both nuclei. That is, at $\tau \approx 0$,

$$\varepsilon(x, y) \propto g^2 Q^2_{s(A)}(x_\perp, y_\perp) \times Q^2_{s(B)}(x_\perp, y_\perp) \tag{7.20}$$

where $Q^2_{s(A)}$ and $Q^2_{s(B)}$ are the saturation scales squred of both our nuclei, g is the strong coupling constant, and ε is the energy density.

Our implementation of the IP-Jazma framework differs from what is described in [32], but the essence remains the same. We generate the nuclei, saturation scales and colour charge densities as we would during a regular IP-Glasma event. However, after the first time step, the simulation is terminated, which saves a lot of computational time. The

code returns a simple dataset, which is comprised of lattice site positions, Q_s^2 for nuclei A and B, and $Q_{s(A)}^2 \times Q_{s(B)}^2$. We then have all it takes to broadly depict the energy density distribution at initial time. Using this description, we can calculate ϵ_2, our eccentricity, at initial times. This is because eccentricity is a relative quantity. By this, we mean that each lattice site's weight in a given eccentricity calculation is not absolute, but relative to the values of the other lattice sites in the same transverse plane. Therefore, the fact that we do not recover an accurate value of the energy density ε is inconsequential to the calculation of eccentricities, which has allowed us to save precious time throughout this project.

8

RESULTS

This section will be constructed such that the thought process we went through becomes clear. Experimental results for deformed nuclei collisions are incredibly scarce. The only reported results within the last decade stem from [3], which will be central to our analysis. However, most of the plots, especially those involving IP-Jazma results, will be compared against data from [2]. Those are results generated by Bjorn Schenke, Prithwish Tribedy and Raju Venugopalan, who are based at the Brookhaven National Laboratory (BNL), where the Relativistic Heavy Ion Collider (RHIC) is located. Although the underlying concepts are similar, our code and theirs are different, and comparing our data with simulations they have done in 2+1 dimensions is an excellent indicator of our progress and the validity of our simulations. Given the general lack of experimental data available for U + U collisions at 193 GeV, the general approach to our analysis, especially towards the end, is to guide further simulations and further data accumulation towards a phenomenological understanding of how initial state anisotropies affect observables, and, by proxy, the formation of QGP. Let us start by reintroducing essential quantities that will be present in our various plots.

8.1 ϵ_n AND v_n

As we have discussed in the introduction, v_2 is the second coefficient of the Fourier expansion of the azimuthal distribution of particles

$$\frac{dN}{p_T dp_T dy d\phi} = \frac{dN}{2\pi p_T dp_T dy}\left(1 + \sum_n 2v_n\left(y, p_T\right)\cos\left[n\left(\phi - \psi_n\right)\right]\right) \tag{8.1}$$

All coefficients present important information about our system, but v_2 is the key signature of the formation of QGP. Coherent elliptic flow, measured by v_2 and described

schematically in figure 5, is linked to ϵ_2, which is a measure of the elliptic shape of the distribution of energy in the initial state that gets converted by hydrodynamic flow from a pressure anisotropy to a momentum anisotropy. While the relationship is true up to the n^{th} harmonic, it is much more important in the case of ϵ_2 and v_2 because of the initial state geometry of colliding nuclei at finite impact parameter. Looking at figure 23, which shows data from a group of 2000 ultra-central events ($b = 0$ fm), we see that v_2 and ϵ_2 form a roughly horizontal line, which illustrates their intimate relationship. A seemingly disheartening fact becomes apparent however, when looking at the inconsistent nature of the two other curves described in figure 23, $\frac{\langle v_3 \rangle}{\langle \epsilon_3 \rangle}$ and $\frac{\langle v_4 \rangle}{\langle \epsilon_4 \rangle}$. However, this can be explained by the fact that, at lower energies, higher flow harmonics have a harder time to develop, given the fleeting nature of the QGP. The peaks and valleys in the $\langle v_3 \rangle / \langle \epsilon_3 \rangle$ and $\langle v_4 \rangle / \langle \epsilon_4 \rangle$ distributions should therefore be regarded as noise explained by our relatively small center of mass energy. Also, even though their allure is much less consistent than that of $\frac{\langle v_2 \rangle}{\langle \epsilon_2 \rangle}$, the fact that the ratios are on three distinct levels, going from the largest for the elliptical ratio to the smallest for the quadratic ratio, is a great sign and consistent with previous results [34]. A more detailed examination of the calculation of v_n is offered in appendix A. We can now look at centrality selection in this thesis.

8.2 ZERO DEGREE CALORIMETER

Heavy-Ion collision simulations usually determine the centrality by calculating the total energy deposited in the transverse plane at a certain rapidity, a quantity related to observables such as the multiplicity. Calculating energies deposited in initial overlaps is not feasible experimentally, so various experimental centrality selection techniques have been devised. One such technique is the use of a Zero Degree Calorimeter (ZDC). We place a ZDC apparatus in line with the beam axis of a collider *starting at the expected point of collision*. In circular colliders, as shown schematically in figure 24, the ZDC is placed such that it is in line with the tangent to the accelerator's path at the point of collision.

ZDCs can only detect neutrons because colliders rely on strong electromagnetic fields to accelerate and guide particles/nuclei. When a nucleus is accelerated, the strong force has the upper hand and the nucleus remains unchanged - a mix of protons and neu-

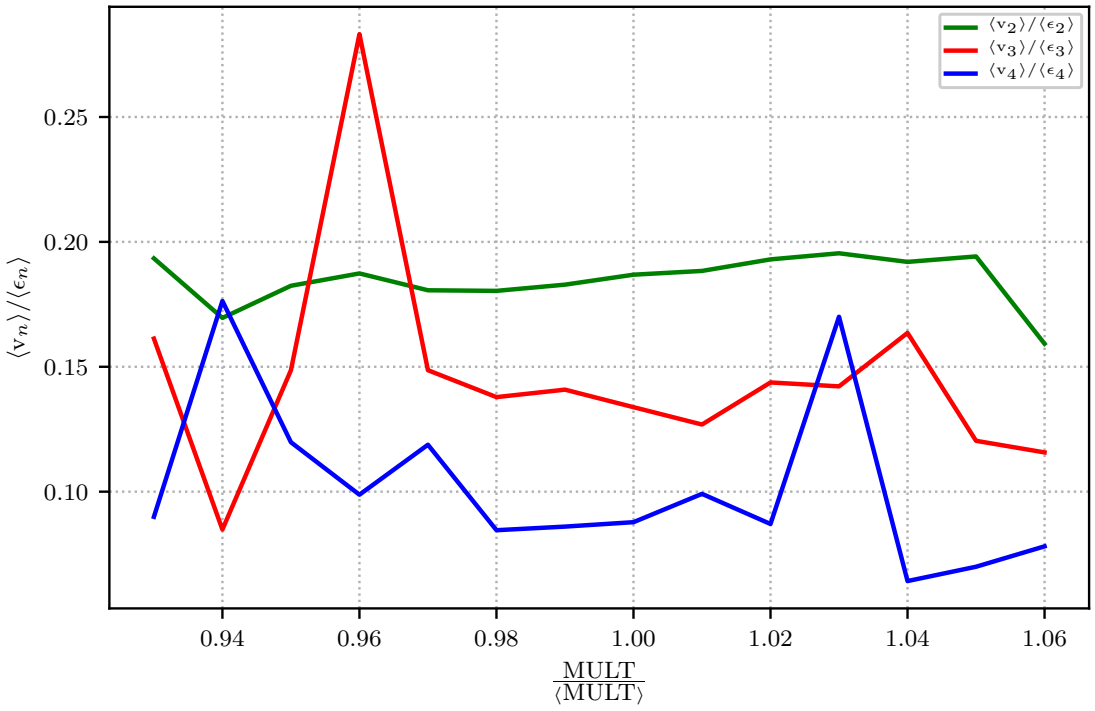

Figure 23: The event averaged v_n in ratio to the event averaged ϵ_n for geometrically ultra-central U + U events at 193 GeV, with $b = 0$fm. The low centre of mass energy makes it so that the third and fourth flow harmonics do not have time to develop as well as the second. For this reason, peaks and valleys in $\langle v_3 \rangle / \langle \epsilon_3 \rangle$ and $\langle v_4 \rangle / \langle \epsilon_4 \rangle$ should be viewed as noise resulting from the lack of development of higher harmonics caused by our relatively low center of mass energy.

trons - at the nuclear scale. Therefore, the positively charged protons are deflected by the electromagnetic fields and carry the neutrons around with them via the strong force. However, the collision is so energetic that it can free a nucleon from its atomic confines. That is, the non-participating protons continue their assisted path around the particle accelerator, while the neutrons, now freed from the grips of the strong force and, therefore, their bond to positive charges, continue in a straight line - unaffected by the overwhelming electromagnetic fields surrounding them. ZDCs measure the neutrons, which make it to its detectors. Experimentalists can then assess how central the collision was, based on the number of neutrons detected: more neutrons mean that there is a higher chance that the collision was off-centre and that most of the nuclear matter from one nucleus missed the other (and vice-versa), while fewer neutrons point to more nuclear matter

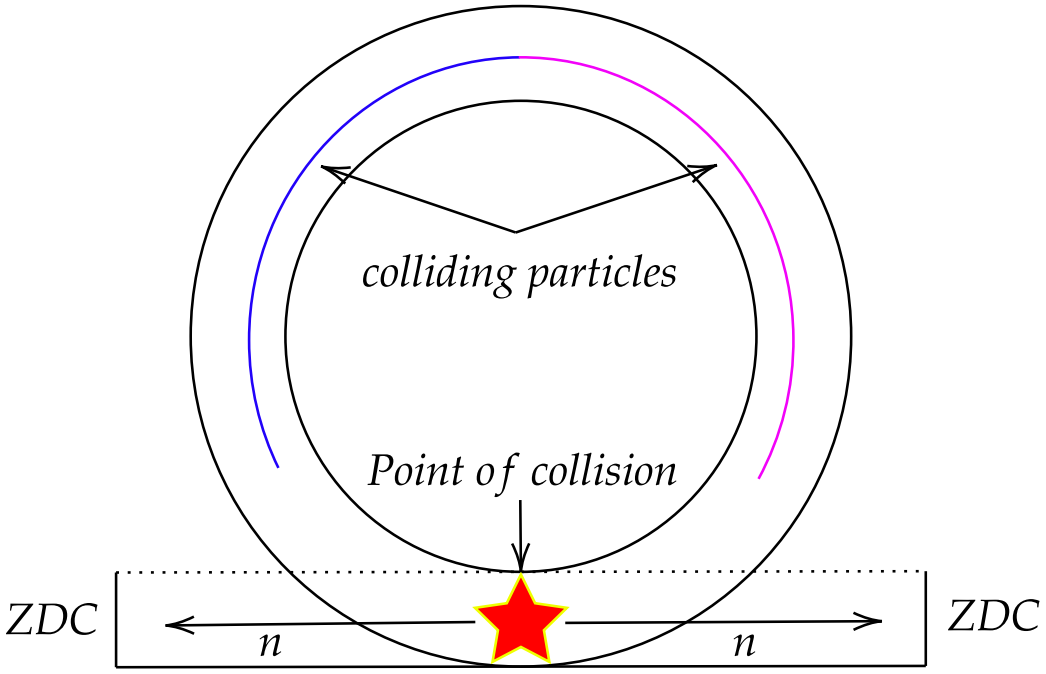

Figure 24: Schematic view of a Zero Degree Calorimeter (ZDC). After the collision, neutrons which have not collided with the opposite nucleus are left undeflected and are measured by the ZDC.

participating in the initial impact, and that they probably have witnessed a very central, head-on collision.

The process of introducing such a centrality determination scheme theoretically is two-fold. Firstly, we find the number of participating nucleons. Two nucleons have an inelastic collision whenever their geometric distance is less than σ_{NN}, the nucleon-nucleon cross-section, which is an energy-dependent quantity. Thankfully, it has been measured at the highest energies at RHIC to be $\sigma_{NN} = 42$ mb [2], which is the value we use in our analysis. Once the number of participating nucleons is determined, we must sample from a binomial distribution to estimate the number of those undeflected nucleons which are neutrons. We are required to do so because, in its current state, our Woods-Saxon sampling method does not differentiate between neutrons and protons. Many efforts are underway to characterize nucleon distribution function using neutron-proton correlation functions [35], and it could be interesting to consider such segregating distributions in the future. For now, however, we sample from equation (8.3). It is important to note,

here, that the measurement is done for each nucleus individually. As can be seen in figure 24, the spectator neutrons from both colliding nuclei are measured in two separate ZDCs. This allows researchers to be even more selective in their events, by asking that both nuclei have a less than x spectator neutrons, instead of only fixating on the total amount of spectators. Therefore, to determine the number of spectator neutrons stemming from a particular nucleus for a given event, we sample from equation (8.3) 100 times per nucleus and average those samplings to obtain a final value. This final value is used to then bin that particular event according to its number of spectator neutrons. By averaging over 100 samplings of our binomial distribution (8.3), we reduce the amount of variability introduced in our results, which was important given the small amount of statistics accrued in our full IP-Glasma+MUSIC+UrQMD runs.

$$\mathrm{P}(X = k) = \binom{n}{k} p^k (1-p)^{n-k} \tag{8.2}$$

$$\Rightarrow \mathrm{P}(X = k) = \binom{S}{N} \left(1 - \tfrac{Z}{A}\right)^N \left(\tfrac{Z}{A}\right)^{S-N} \tag{8.3}$$

In equation (8.3), S represents the number of spectators stemming from a given nucleus (calculated geometrically), Z is the atomic number (98 for U), A, the atomic mass (238 in this thesis), and N is what we aim to sample, the number of neutrons. The results that follow all stem from the same single centrality cut. That is, the selection process is binary. If both nuclei accounted for six (6) or fewer neutrons "detected" by our ZDC, we retain the event. If not, we do not group the event with the others (although its data will someday prove useful). This specific cut mimics what is done in [2] and [3], and represents the $0 - 0.1\%$ most central events of a minimum-bias set of events using randomly oriented U nuclei. We are now ready to interpret our results.

8.3 ULTRA-CENTRAL EVENTS

This project's goal was always to determine the effects of initial state geometry on observables. With this in mind, we set out to generate data using our 2+1D IP-Glasma framework, coupled to MUSIC and UrQMD. In this phase, we generated 2000 geometrically ultra-central events. That is, we set our impact parameter b to 0fm. The deforma-

tion parameters for our Uranium nuclei were taken from [36], a well-known compilation of experimentally obtained deformation parameters for commonly used ions. The deformed Woods-Saxon parameters were $R = 6.874$ fm, $a = 0.556$ fm, $\beta_2 = 0.2802$ and $\beta_4 = -0.0035$. Finally, instead of orienting our nuclei in a specific direction, we randomly oriented each generated nucleus' long axis to avoid biases towards events which cannot be intentionally reproduced experimentally.

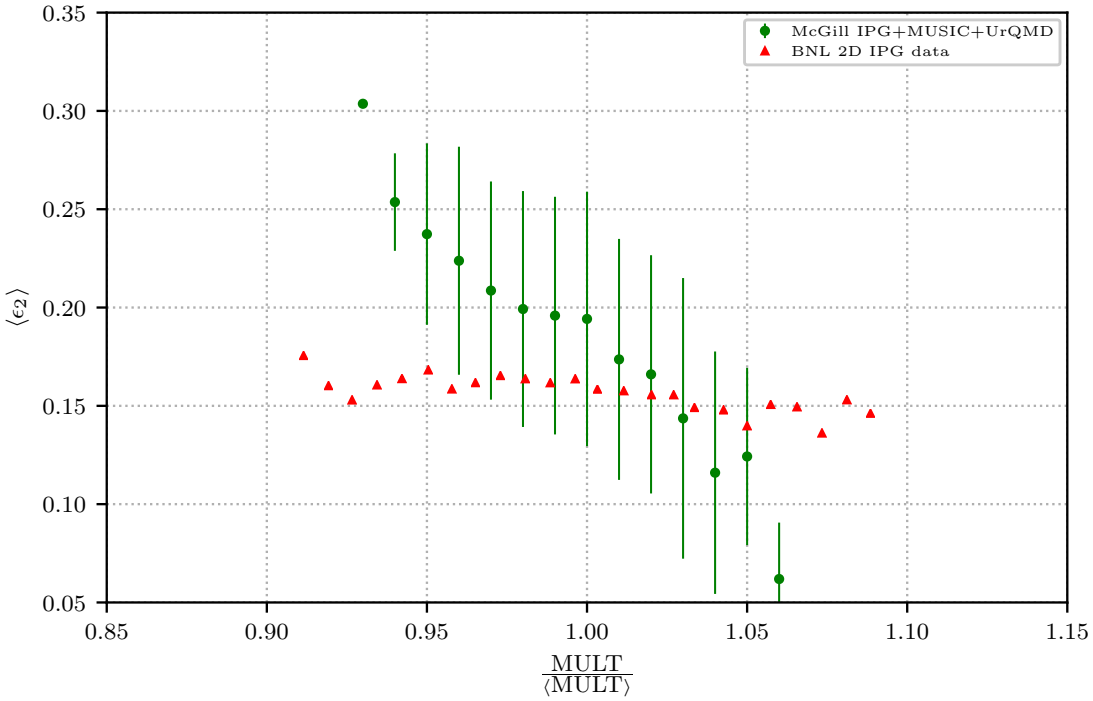

Figure 25: Eccentricity versus scaled multiplicity for geometrically ultra-central U+U events at 193 GeV $b = 0$fm, compared to BNL data [2].

Figure 25 shows our data compared to that obtained through BNL's version of 2+1 D IP-Glasma. Before we go further, it is important to note that the data obtained by BNL [2] does not stem from a full hydrodynamic+hadronic cascade simulation. They get their scaled multiplicities by using fits of gluon multiplicity for events ran and compared against experimental data. This is a good approximation but does not replace going through MUSIC and UrQMD. Nevertheless, as will become apparent, their data compares itself nicely against experimental flow harmonics.

Looking back to figure 25, our data seems to vary more than BNL's data. It is less steady and goes through a wider range of eccentricity values. For the most part, BNL's

data is within our errors, which means we are not completely off. However, statistically, about half of our 2000 events make it through our centrality cut, meaning that, while 1000 events are by no means an excessive amount, it is still a statistically significant amount, and the tail-ends of our distributions are far from satisfactory. The datapoint without error bars stems from a single event. Let us now look at how our dataset fares against experimental data.

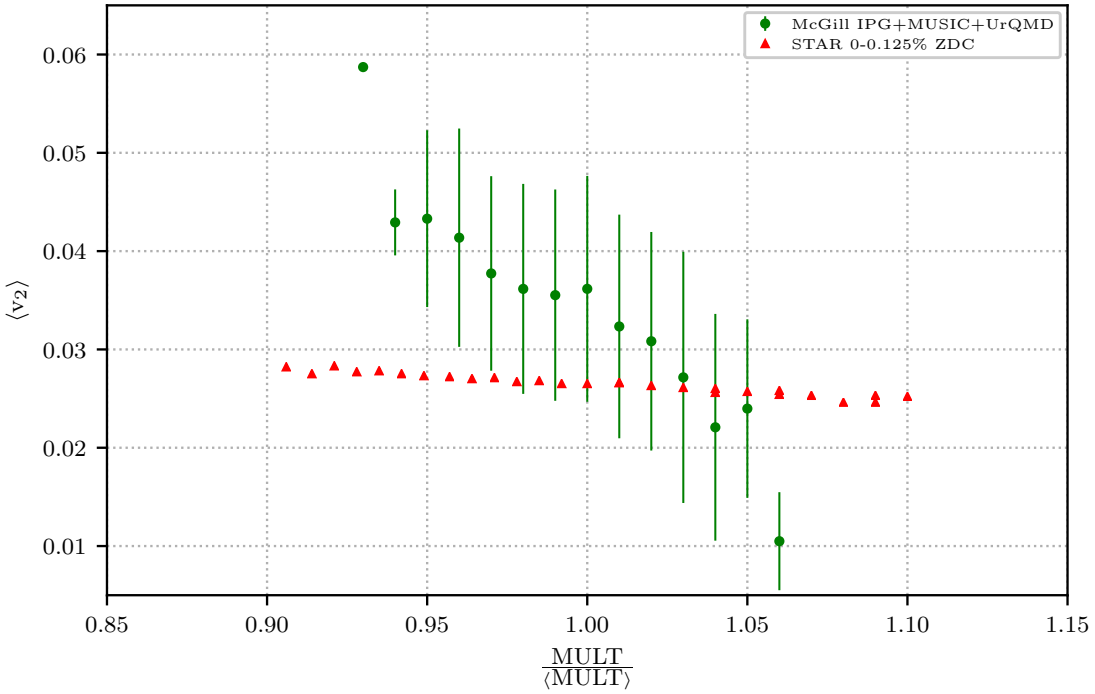

Figure 26: Elliptic flow versus scaled multiplicity for geometrically ultra-central U+U events at 193 GeV $b = 0$fm, compared to STAR data [3].

Figure 26 shows our elliptic flow values plotted against scaled multiplicity, and compared to STAR data, for the $0 - 0.125\%$ most central events of their runs. Once again, our data's variance is too high, and we are not reproducing experimental data satisfactorily. Notice that the STAR data shown in figure 26 and the BNL data shown in figure 25 follow the same flat distribution. This shared behaviour matches expectations of how eccentricity and elliptic flow distributions should compare, and is another reason we have decided to attribute as much importance to BNL's data. At this point, it seems like our dataset is biased towards events that do not contribute as much in an experimental setting. However, inspired by a paper [37], which showed that successively binning first by energy, and then by ZDC calculations could greatly reduce variability and omit outlying

events from consideration, we pursued our analysis. Figure 27 shows different attempts at this successive binning technique.

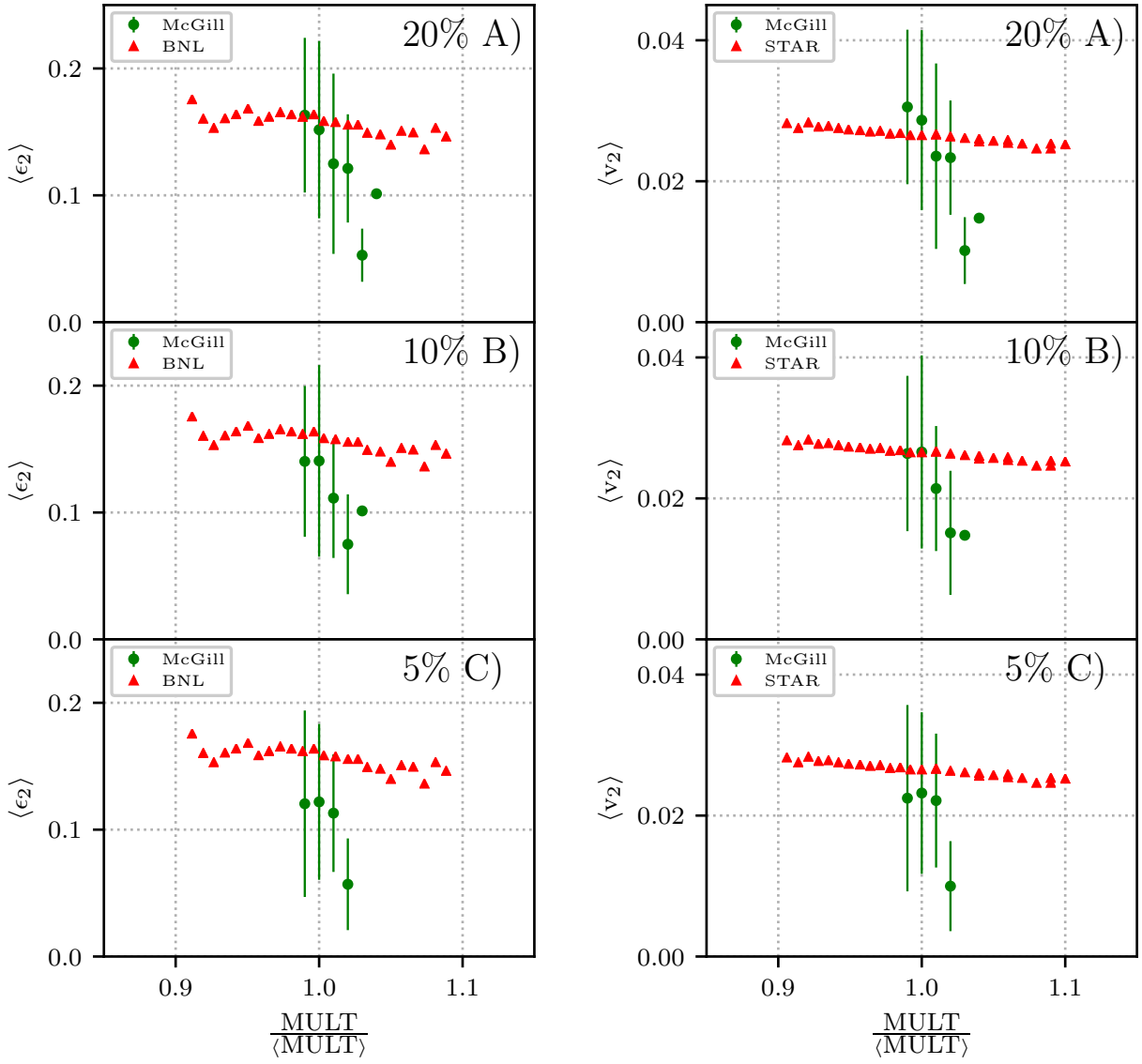

Figure 27: **LEFT COLUMN**: Eccentricity versus scaled multiplicity for geometrically ultra-central U+U events at 193 GeV $b = 0$fm, compared to BNL data [2]. **RIGHT COLUMN**: Elliptic flow versus scaled multiplicity for geometrically ultra-central U+U events at 193 GeV $b = 0$fm, compared to STAR data [3]. **A)** 20% most energetic events. **B)** 10% most energetic events. **C)** 5% most energetic events.

The **A)** panels have the largest acceptance of energy, at 20%, while the **C)** panels show the most restrictive energy window implemented, at 5%. The reclassified data does look better, especially in the **A)** panels where it overlaps BNL and STAR data at average

multiplicity. It, however, does reduce our statistics and our data's range in multiplicity. From 1000 events making it through the sole ZDC cut in our previous plots, **A)** works with $\sim$ 250 events, **B)**, with $\sim$ 150, and **C)**, with $\sim$ 70. While this is not sufficient to conclude our search, it provides useful information and indicates that our framework is behaving intuitively. The more restrictive we become in our energy filters, the less eccentricity (and elliptic flow) our data showcases. Low eccentricity values are linked to circularly shaped interaction regions, which, in the case of deformed nuclei collisions, must be caused by tip-tip collisions. Tip-tip collisions generate greater colour charge densities and more extreme collision conditions, leading to more energy being stored in the transverse plane. These results, then, do not invalidate our model.

This dataset raises many questions. To answer some of them, we turn to the IP-Jazma framework, described in chapter 7, to help us gain insights into which parameters, if any, could be at fault in our analysis.

8.4 IP-JAZMA AS A GUIDE

We ran six distinct sets of events using IP-Jazma, each comprising 50000 events. This high number of events is made possible because a single event using this framework takes approximately 2 minutes to run while going through 2+1D IPG+MUSIC+UrQMD can take up to 12 hours per event. By generating decent amounts of data in much less time, we were able to put a few hypotheses to the test.

We wanted to know if we had been too restrictive in our choice of impact parameter and were consequently omitting key initial state geometries, which contributed towards BNL's and STAR's results from minimum bias runs, but not ours. To do so, we set one of our runs' impact parameter range from $b = 0$ to 20 fm, and another from $b = 0$ to 8 fm. The reasoning behind these choices was that, while we wanted to see if a true minimum-bias set of runs would help quell the large variances in our data, the argument that omitting particular initial state geometries relevant to ultra-central ZDC collisions would not be valid beyond a few fm. Too large of an impact parameter all but guarantees that at least one of the nuclei will have more spectator neutrons than our threshold for consideration, and would generate a lot of redundant data.

Next, given that the BNL group did not use self-avoidance in their Woods-Saxon sampling (i.e. they considered nucleons to be point-like and with no spatial extent, therefore allowing them to be within any distance of one another), we wanted to see how much effect that would have on our data. On that same note, we wanted to see if using the same deformation parameters used by the BNL team would have any effects. That is, although marginal, our β_2, β_4, R and a parameters all displayed differences. The parameters used for generating their deformed nuclei were $R = 6.81$ fm, $a = 0.55$ fm, $\beta_2 = 0.28$ and $\beta_4 = 0.093$. Using these parameters, we ran our fourth set of IP-Jazma events.

Finally, we wanted to ensure that our deformation software was not at fault and that the Woods-Saxon sampling procedure was going smoothly. To do so, we set up our two final sets of runs. The first had its deformation parameters β_2 and β_4 set to 0, leaving us to sample those runs with a regular Woods-Saxon distribution. We also wanted to see what halving β_2, the most influential deformation parameter would do to our minimum bias runs. We therefore set $\beta_2 = 0.1401$ and set the impact parameter range from $b = 0$ to 8 fm.

It is important to note that, while we will be comparing these events to BNL and STAR data using scaled multiplicity, Jazma only allows estimates of total energy. Therefore, all IP-Jazma data presented runs on the assumption that transverse plane energy deposition and final state multiplicity are intrinsically related.

With this lengthy description out of the way, we can look at our IP-Jazma results.

In figure 28, while some panels look promising, we seem to have exacerbated the eccentricity variability we were looking to appease. Figures 29 and 30 showcase the use of the successive binning technique used previously, keeping only the 1% and 0.1% most energetic events respectively before applying our ZDC cut. Let us analyze these in order.

First, panel **A)** shows an apparent lack of statistics stemming from the fact that our impact parameter range is far too broad. Only ~ 40 events out of the 50 000 events make it through our cut, and we cannot make a definite statement regarding anything. This fact is only made worse by our successive binning technique - omitting much-needed data obviously will not help.

Panel **B)** shows comparable data to what we obtained in our first full ultra-central IPG+MUSIC+UrQMD. The successive binning technique gets rid of the most significant

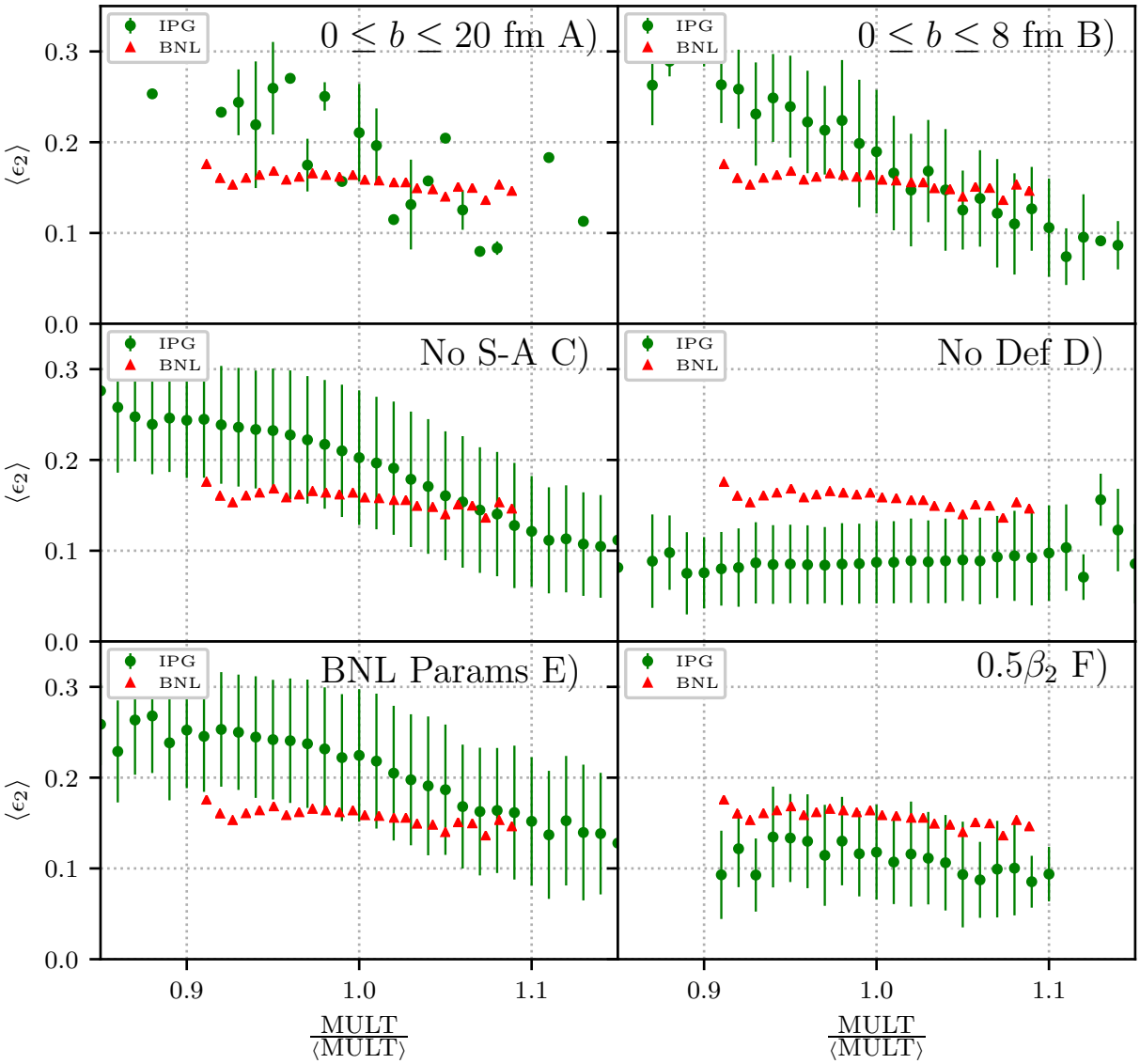

Figure 28: Eccentricity versus scaled multiplicity for U+U using IP-Jazma at 193 GeV. **A)** Minimum-bias run with impact parameter range $b = 0$ to 20 fm. **B)** Slightly-biased run with impact parameter range $b = 0$ to 8 fm. **C)** Self-avoidance neglected in Woods-Saxon sampling procedure. **D)** No deformation (perfectly symmetric Woods-Saxon distribution). **E)** Perfectly reproducing the initial parameters used by the BNL group [2]. **F)** Slightly-biased run with impact parameter range $b = 0$ to 8 fm and $\beta_2 = 0.1401$ (halved).

outliers, which is what we had hoped. However, keeping only the 0.1% most energetic events is too restrictive in this case.

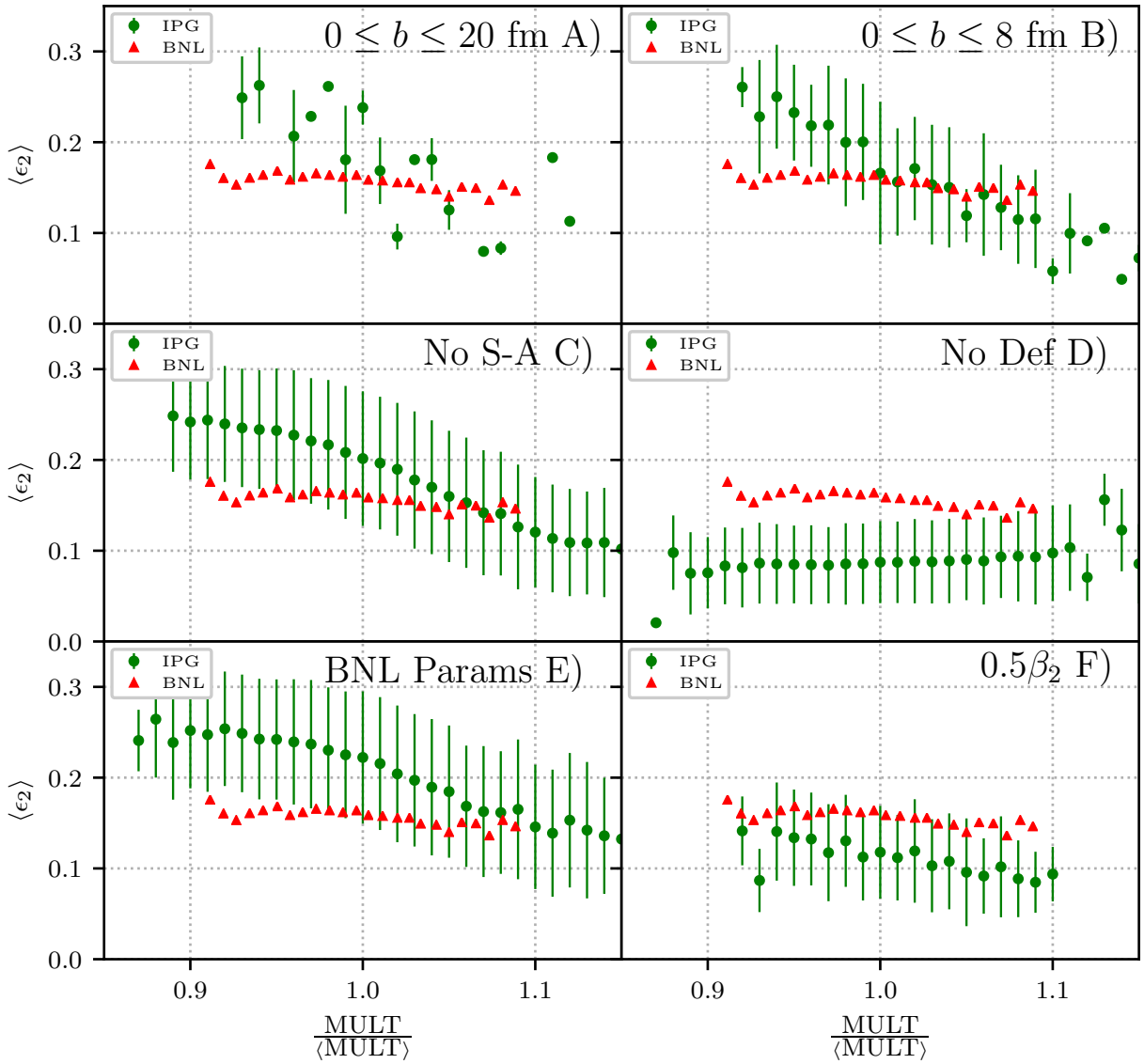

Figure 29: Eccentricity versus scaled multiplicity for U+U using IP-Jazma at 193 GeV, using the 1% most energetic events. **A)** Minimum-bias run with impact parameter range $b = 0$ to 20 fm. **B)** Slightly-biased run with impact parameter range $b = 0$ to 8 fm. **C)** Self-avoidance neglected in Woods-Saxon sampling procedure. **D)** No deformation (perfectly symmetric Woods-Saxon distribution). **E)** Perfectly reproducing the initial parameters used by the BNL group [2]. **F)** Slightly-biased run with impact parameter range $b = 0$ to 8 fm and $\beta_2 = 0.1401$ (halved).

Panel **C)** shows less variance in eccentricity, and the tails of the distributions in figure 28 seem to flatten out, which is a great sign. Applying our successive binning technique gets rid of low-energy data and reveals a bias existing in these events to-

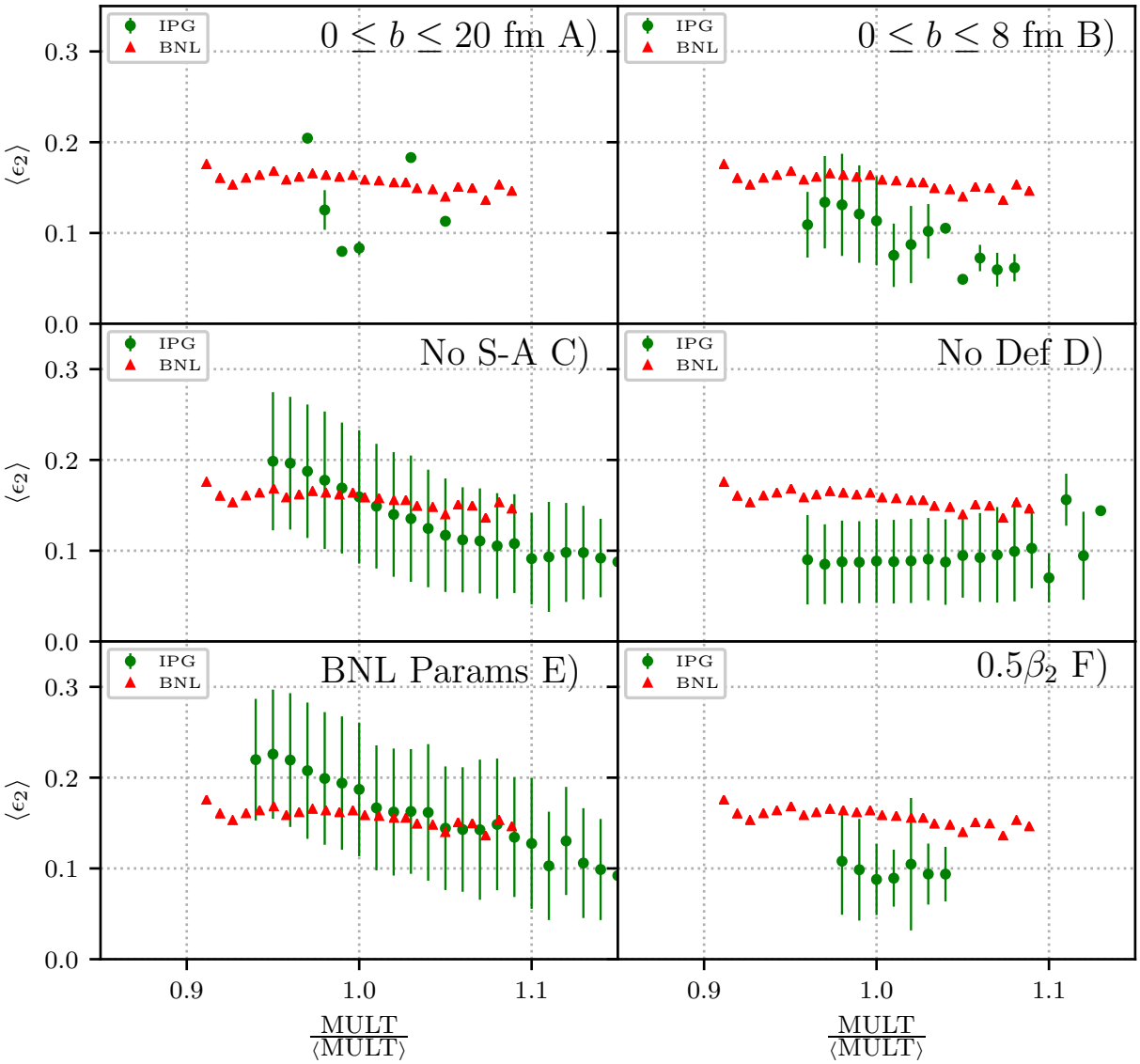

Figure 30: Eccentricity versus scaled multiplicity for U+U using IP-Jazma at 193 GeV, using the 0.1% most energetic events. **A)** Minimum-bias run with impact parameter range $b = 0$ to 20 fm. **B)** Slightly-biased run with impact parameter range $b = 0$ to 8 fm. **C)** Self-avoidance neglected in Woods-Saxon sampling procedure. **D)** No deformation (perfectly symmetric Woods-Saxon distribution). **E)** Perfectly reproducing the initial parameters used by the BNL group [2]. **F)** Slightly-biased run with impact parameter range $b = 0$ to 8 fm and $\beta_2 = 0.1401$ (halved).

wards more considerable energies. That is, while the average energy (multiplicity) of the datasets stands squarely in the middle of our plot, we see much more points to the right of the average than to the left, meaning that there was a lot more variability in

the energies generated by these events. This bias is most probably caused by the lack of self-avoidance, leading to denser nuclei on average. Denser nuclei lead to denser colour charge distributions, and, in turn, more extreme energy values

Panel **D)** demonstrates that spherically symmetric, non-deformed Woods-Saxon distributions in geometrically ultra-central collisions produce very small eccentricities, as the overlap regions tend to be circular. This data is reassuring, as it shows that the Woods-Saxon sampling, at its base, is not flawed.

Panel **E)** illustrates high eccentricity values in figure 28, which are surprising given that this data stems from a perfect reproduction of BNL's initial parameters. However, the corrections offered by our successive binning techniques do bring the eccentricities into closer accord with BNL's data.

Finally, **F)** shows values that are too small, with no crossing towards the data whatsoever. While the values are close to BNL's data, they are of the order of the non-deformed values from panel **D)** and, while they cannot be discarded outright, do not constitute proof of anything fishy going on with our or BNL's deformation application.

The final figure, fig. 31, shows the eccentricity against the total number of participants in a given event. This plot allows for a broader interpretation of results, seeking to verify the extent of the validity up to peripheral events, and also ensures that generated events do not go to waste. The panels with few points concentrated at the rightmost end of the plot are those for which the impact parameter b was 0, while those with more substantial distributions represent datasets with broader impact parameter ranges. It is interesting to note that the panels showcasing broader impact parameter ranges seem to all have overshot their purpose. With our impact parameter range as small as $b = 0$ to 8 fm, we are still generating many peripheral events, down to as low as ~ 130 total participants, which is much too peripheral for our purposes.

The main conclusion extracted from these runs is that expanding the impact parameter range is beneficial, but conservatism is critical. Given that our full simulations are computationally and temporally expensive, we should be careful not to overshoot our impact parameter range and generate large swaths of peripheral events. The benefits seem to be clear: deformed nuclei can exhibit highly anisotropic and energetic overlap areas at impact parameters larger than those of spherically symmetric nuclei. While it

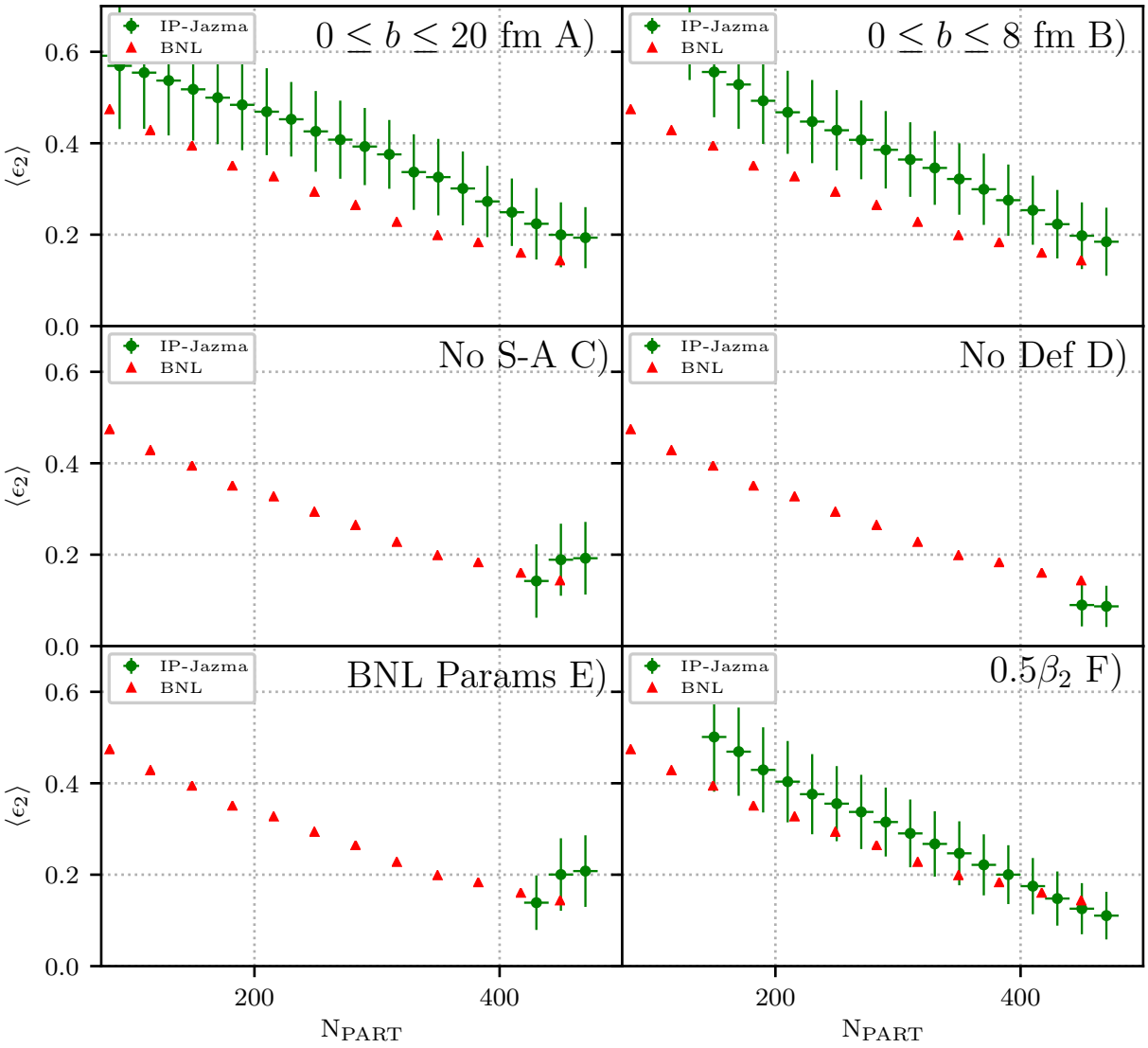

Figure 31: Eccentricity versus total number of participant nucleons for U+U using IP-Jazma at 193 GeV, compared to BNL data [2]. **A)** Minimum-bias run with impact parameter range $b = 0$ to 20 fm. **B)** Slightly-biased run with impact parameter range $b = 0$ to 8 fm. **C)** Self-avoidance neglected in Woods-Saxon sampling procedure. **D)** No deformation (perfectly symmetric Woods-Saxon distribution). **E)** Perfectly reproducing the initial parameters used by the BNL group [2]. **F)** Slightly-biased run with impact parameter range $b = 0$ to 8 fm and $\beta_2 = 0.1401$ (halved).

may seem like our deformation procedure is at fault when looking at panels showcasing non-deformed data, it is essential to note that, concerning our deformed data, the non-deformed datasets behave as expected. We find lower eccentricities caused by spherical nuclei at small impact parameters (large number of participants) while climbing more

rapidly than the BNL data at larger impact parameters (smaller number of participants). Therefore, the results stemming from non-deformed and less-deformed runs are inconclusive as of yet, and warrant a deeper investigation, which is still ongoing.

We are now able to analyze the final results presented in this thesis, stemming from our most recent runs.

8.5 BIASED RUN

After our endeavours in IP-Jazma, we return to full 2D IPG+MUSIC+UrQMD simulations. Our objectives for this run were to increase the number of events, while also allowing enough of a gap in impact parameter such that non-trivial initial conditions could occur within our simulations. Therefore, we settled on 10000 events, with impact parameter range $b = 0$ to 4 fm, while all other parameters remained the same as in our first run. While the impact parameter range might seem restrictive, it is motivated by the fact that most events beyond 4 fm in impact parameter are extremely peripheral, as shown in figure 31 and explained previously.

We begin by presenting the v_n to ϵ_n ratio, as was done in the beginning of this chapter. Figure 32 looks very similar to figure 23. Although the $\frac{\langle v_3 \rangle}{\langle \epsilon_3 \rangle}$ distribution does look better in this current iteration, spikes and variability can be found to a similar extent. The smoothness of the distribution for $\frac{\langle v_3 \rangle}{\langle \epsilon_3 \rangle}$ might be caused by increased statistics. The fact that, at these energies, higher harmonics have a harder time forming does remain true, however, and is apparent in the distribution for $\frac{\langle v_4 \rangle}{\langle \epsilon_4 \rangle}$.

We look at figure 33, which shows our eccentricity versus scaled multiplicity as compared to BNL's data. Here, we see a net improvement upon the results of figure 25. The general slope of the points is much more steady, and the tails of our distribution are much closer to the rest of the data, with the notable exception of the one, error-bar-less point in the top left, which stems from an extreme outlier in the ~ 300 datapoints making it through our ZDC cut. Our data, however, is still slightly too high.

Next, we show the elliptical flow harmonics versus scaled multiplicity for the current dataset. The same progress concerning fig. 26 is made here, which is what we would expect, given that we now know that both v_2 and ϵ_2 are intrinsically linked.

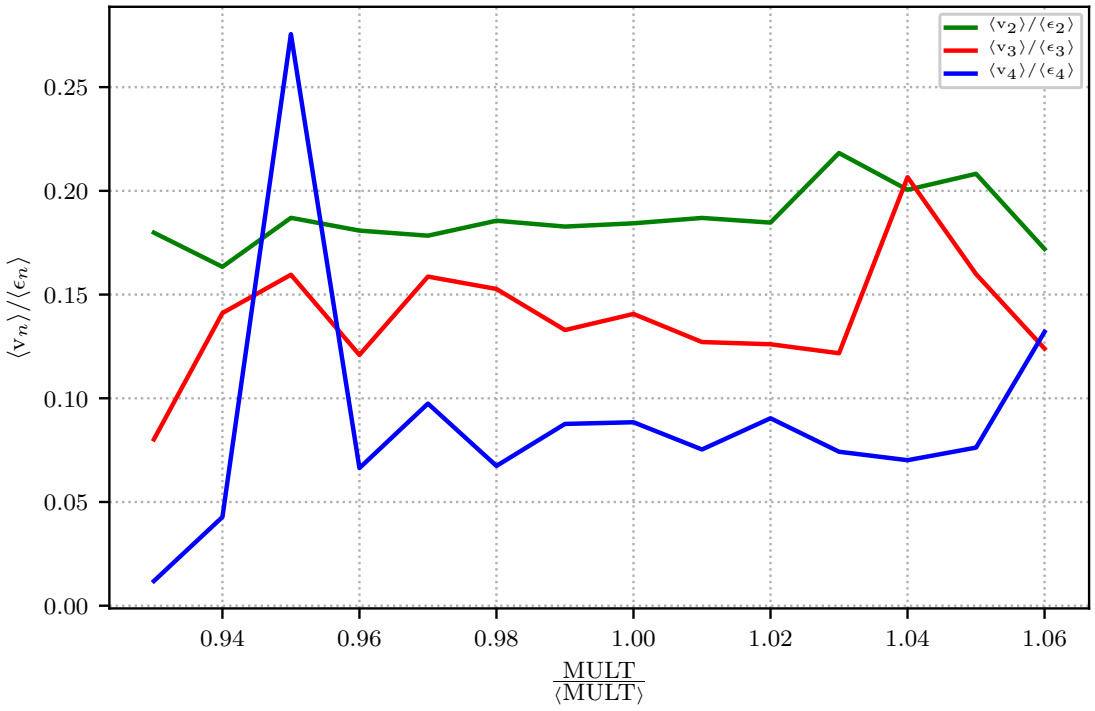

Figure 32: The event averaged v_n in ratio to the event averaged ϵ_n for biased U + U events at 193 GeV, with the impact parameter ranging from $b = 0$ to 4 fm. Similarly to fig. 23, the low centre of mass energy makes it so that the third and fourth flow harmonics do not have time to develop as well as the second.

Figure 35 shows our successive binning technique applied to our new dataset. As mentioned before, $\sim$ 300 events make it through the ZDC cut alone. That constitutes $\sim$ 3% of our events and is enough for us to reach statistically significant conclusions. However, such a small portion of our events, making it through means that our successive binning technique might not be necessary in this case, even though it is far from a minimally biased dataset. While panel **A)** removes the the outlier from figures 33 and 34, it does not do much beyond that. Both panels **B)** and **C)** flatten our data out, but do so at the expense of statistics and scaled multiplicity range, meaning that our data's general trend is harder to extrapolate. However, they are promising in the sense that their points close to average multiplicity match experimental values very closely.

We end this section ϵ_2 and ϵ_3 plotted versus the number of participants and multiplicity, respectively. Starting with figure 36, we the data shown in figures 33 and 35 shown in a different light. That is, we recognize, at the rightmost end, the central colli-

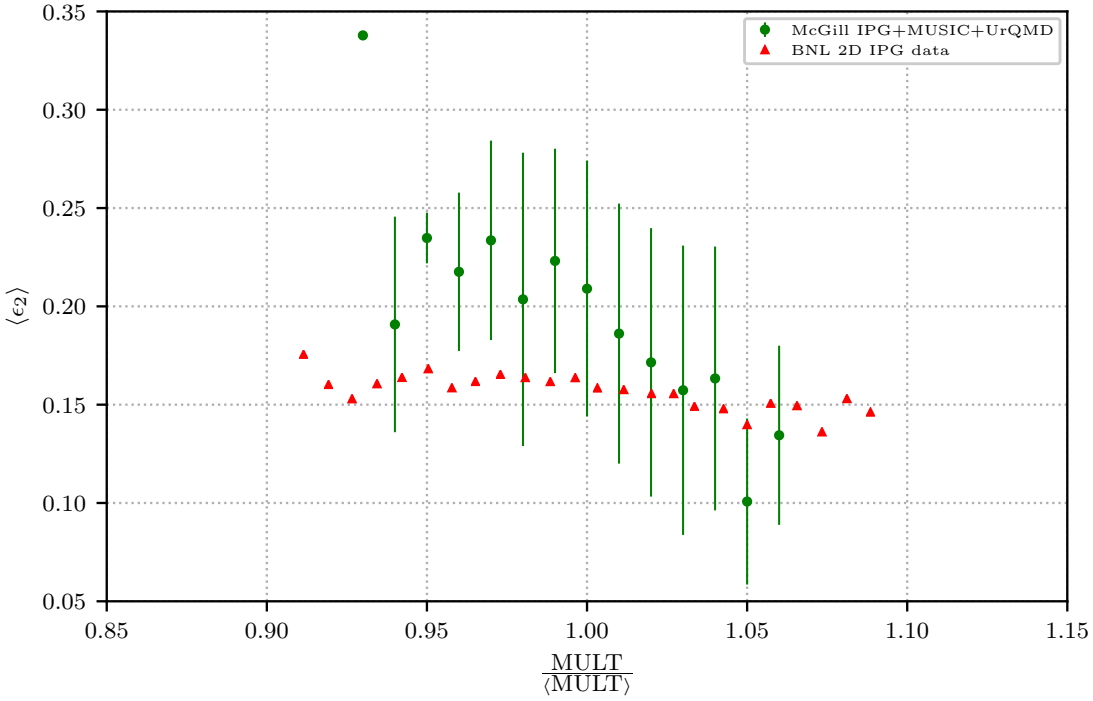

Figure 33: Eccentricity versus scaled multiplicity for biased U+U events at 193 GeV, with the impact parameter ranging from $b = 0$ to 4 fm, compared to BNL data [2].

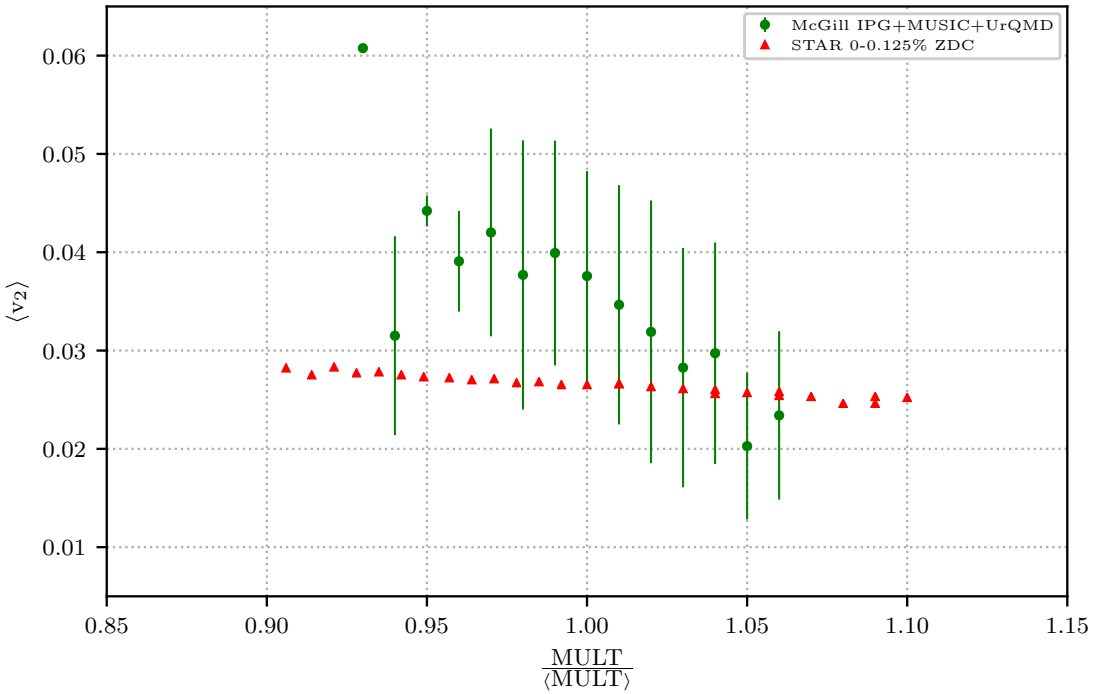

Figure 34: Elliptic flow versus scaled multiplicity for biased U+U events at 193 GeV, with the impact parameter ranging from $b = 0$ to 4 fm, compared to STAR data [3].

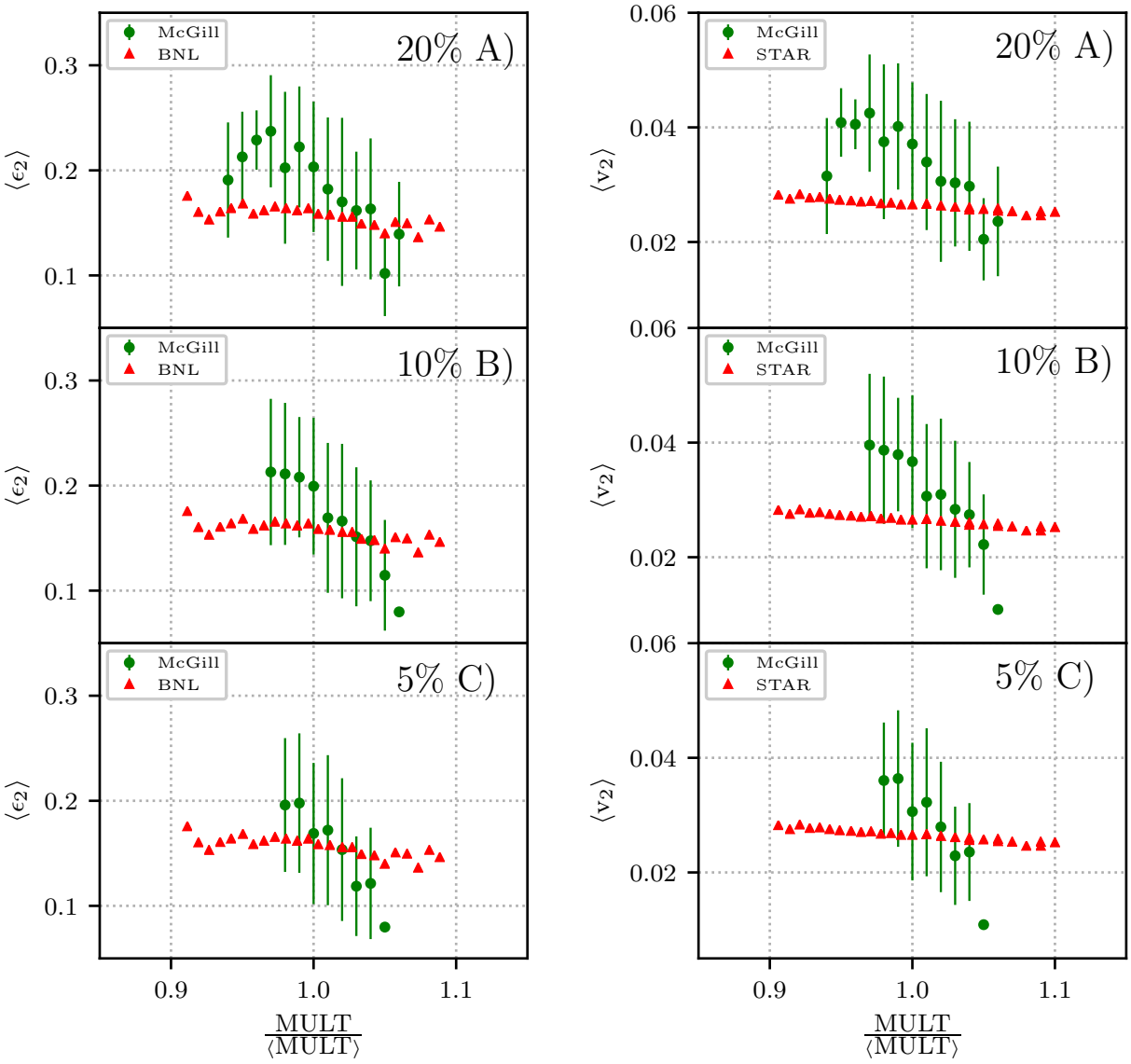

Figure 35: **LEFT COLUMN**: Eccentricity versus scaled multiplicity for biased U+U events at 193 GeV, with the impact parameter ranging from $b = 0$ to 4 fm, compared to BNL data [2]. **RIGHT COLUMN**: Elliptic flow versus scaled multiplicity for biased U+U events at 193 GeV, with the impact parameter ranging from $b = 0$ to 4 fm, compared to STAR data [3]. **A)** 20% most energetic events. **B)** 10% most energetic events. **C)** 5% most energetic events.

sions which we are represented in those figures. We are within the error of the relevant points. However, going towards more peripheral collisions, we see that our data presents considerably higher values of eccentricity than what BNL is reporting. In stark contrast, figure 37 shows the opposite: our dataset's triangularities are smaller than those reported

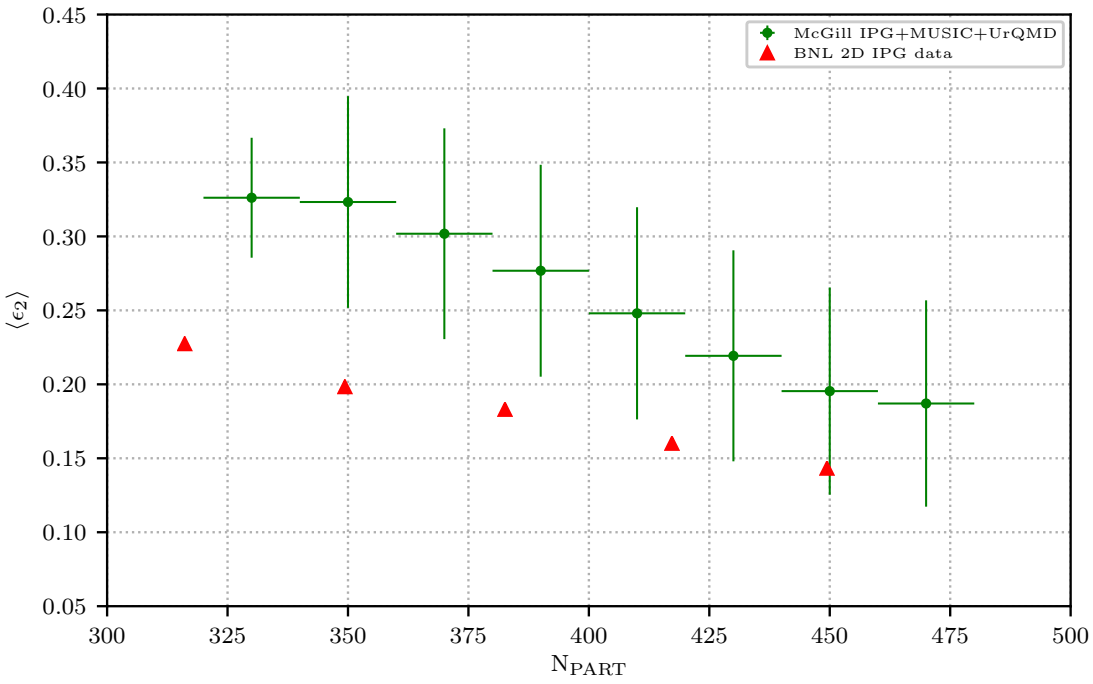

Figure 36: Eccentricity versus total number of participant nucleons for U+U events at 193 GeV, with the impact parameter ranging from $b = 0$ to 4 fm, compared to BNL data [2].

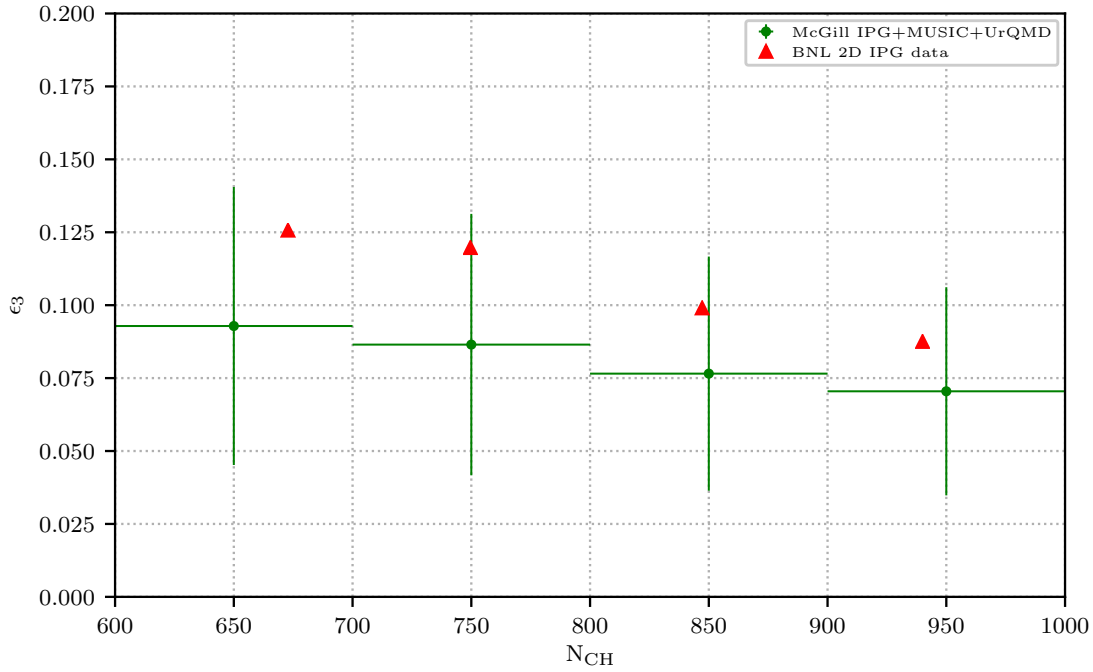

Figure 37: Triangularity versus multiplicity for U+U events at 193 GeV, with the impact parameter ranging from $b = 0$ to 4 fm, compared to BNL data [2].

by BNL while remaining within error. While these two plots were added to ensure that all analysis elements were available to the reader, it is important to note that second and third flow harmonic data was not reported by the STAR collaboration in [3] for peripheral collisions. Therefore, BNL's data and trends for these specific plots is not yet verified by experimental data. Both our and their data, while showing differences, are parts of a plausible whole.

9

CONCLUSION AND FUTURE WORK

In this thesis, we have discussed the motivation for Heavy-Ion Collisions and the underlying theoretical framework in which we study them, with a strong emphasis on the initial state. In particular, we have provided an in-depth description of the IP-Glasma model, highlighted its distinguishing features, and some of its phenomenological successes. We have also described in detail how we generate deformed nuclei and the expected effects of using deformed collision systems.

These unusual, asymmetric initial conditions have challenged our ability to describe established theoretical data and experimental data at $\sqrt{s} = 193$ GeV. However, in the span of our work, we have been able to considerably improve our results by the use of phenomenological and theoretical analysis. By this, we mean that, after an initial assessment, we were able to use tools based upon the IP-Glasma framework at large in order to guide our final analysis. The evident lack of experimental data describing deformed systems makes unbiased analyses tough. However, in this thesis, it allowed us to showcase the flexibility and applicability of our framework at large. Critical insights into the role of the impact parameter b, deformation parameters β_2 and β_4, and that of the collision energy were realized.

This helped us further the broader goal of proving the existence of QGP, and analyzing its consequences on observables. By generating non-trivial initial state anisotropies, we were able to produce larger ranges of eccentricities ϵ_2, which, as we have shown, are critical to the later properties of the QGP. By generating unique configurations of the overlap area, we were able to generate values of eccentricity which are usually inaccessible when using spherically symmetric nuclei. We have, therefore, been successful in generating the types of initial conditions which can lead to interesting effects within the QGP and on end-state observables.

While this project was a success, its narrow scope means that our search for the effects of initial state anisotropies on observables remains wide open. We realize that the data presented and the conclusions reached are only partial, and our analysis must be deepened. For this, we believe that increasing statistics on our final runs could be helpful. We also believe that a full minimum bias dataset could be an exciting addition, as it would allow for a more intelligent analysis of the effects of deformed nuclei on observables. By focusing entirely on central (as determined by a ZDC) collisions, we might be losing insights by overlooking peripheral events, which could hold the key to the specific effects of deformed nuclei and initial state anisotropies at large on end-state observables. The end goal will be to generate data using a 3+1D simulation, which will provide more detailed calculations of important quantities at hand, such as longitudinal flow. We also hope to have considerably more experimental data in the near future.

Part IV

APPENDIX: CALCULATIONS AND USEFUL QUANTITIES

A

COORDINATES & IMPORTANT CALCULATIONS

Here, we give a quick reference guide which can be useful to conceive of the sometimes odd $\tau - \eta$ coordinate system, as well as a key calculation in said coordinate system. We also show how calculations of the flow harmonics v_n are done in this thesis.

A.1 LIGHT-CONE COORDINATES

In light-cone coordinates, we mix beam-axis coordinates (z) with temporal coordinates t to obtain a sensible way of analyzing heavy-ion collisions. Using typical cartesian coordinates would lead to multiple complications. The most easy of these to conceive of is the velocity with which each part of our system is moving. Therefore, looking at these collisions in a fixed system of with coordinates (x, y, z, t) would force us into analyzing huge, constantly expanding volumes, even on the relatively small timescales at which these events occur. Therefore, we use rapidity coordinates in order to constantly move with specific parts of our coordinate system which are going at specific speeds relative to the speed of light. Let us start our descriptions, then, with

$$x^{\pm} = \frac{1}{\sqrt{2}} (t \pm z) \tag{A.1}$$

$x^{\pm}$ trace the light-cone from the origin onwards, and are used to track our nuclei in the CGC framework. We can write quantities such as momentum in the same way,

$$p^{\pm} = \frac{1}{\sqrt{2}} (E \pm p^z) \tag{A.2}$$

Very important definitions within this coordinate system include the *proper time* τ,

$$\tau = \sqrt{t^2 - z^2} \tag{A.3}$$

and spacetime rapidity,

$$\eta = \tfrac{1}{2} \ln \left(\tfrac{t+z}{t-z} \right) \tag{A.4}$$

which can both be written in terms of $x^{\pm}$ if one uses

$$x \cdot y = x^+ y^- + x^- y^+ - x_\perp y_\perp \tag{A.5}$$

$$\Rightarrow \tau = \sqrt{x^+ x^-} \tag{A.6}$$

$$\Rightarrow \eta = \tfrac{1}{2} \ln \left(\tfrac{x^+}{x^-} \right) \tag{A.7}$$

where equation A.5 is the dot product of two vectors. We use proper time τ to evolve our system, because it puts us in the reference frame of the moving particles which are experiencing all of this. By way of a simple trick, we can find

$$\tau = \sqrt{t^2 - z^2} = t\sqrt{1 - \left(\frac{z}{t}\right)^2} = t\sqrt{1 - v_z^2} = \frac{t}{\gamma} \tag{A.8}$$

where γ is the Lorentz factor. One can also solve equations A.3 and A.4 to find

$$t = \tau \cosh \eta = \tfrac{1}{2} \left(x^+ + x^- \right) \tag{A.9}$$

$$z = \tau \sinh \eta = \tfrac{1}{2} \left(x^+ - x^- \right) \tag{A.10}$$

It is clear, however, that we are working with 3 different coordinate systems, which, even though they are related, can lead to complications. We explicitly define their respective metrics in order to avoid any confusion, and possibly to save the reader a headache:

$$g_{\mu\nu}\left(x^{+},x^{-}\right)=\begin{pmatrix}0&1&0&0\\1&0&0&0\\0&0&-1&0\\0&0&0&-1\end{pmatrix} \tag{A.11}$$

$$g_{\mu\nu}(\tau,\eta)=\begin{pmatrix}1&0&0&0\\0&-1&0&0\\0&0&-1&0\\0&0&0&-\tau^{2}\end{pmatrix} \tag{A.12}$$

$$g_{\mu\nu}(t,x,y,z)=\begin{pmatrix}1&0&0&0\\0&-1&0&0\\0&0&-1&0\\0&0&0&-1\end{pmatrix} \tag{A.13}$$

where one recognizes, in $g_{\mu\nu}(t,x,y,z)$, the regular Minkowski metric, given as reference. One can change between these metrics by applying the standard

$$g'_{\alpha\beta}=\frac{\partial x^{\mu}}{\partial x^{\alpha}}\frac{\partial x^{\nu}}{\partial x^{\beta}}g_{\mu\nu} \tag{A.14}$$

A.2 CLASSICAL YANG-MILLS FIELD STRENGTH AND EOMS

This section outlines selected detailed steps towards recovering the field strength tensor and equations of motion in $\tau-\eta$ coordinates. We will skip over details already presented in chapter 4, and how tricky steps that were overlooked. Let us start.

Take the tensor in light cone coordinates and the ansatz as described in chapter 4, and substituting the latter into the former

$$F^{i\pm} = \partial^i A^\pm - \partial^\pm A^i - ig\left[A^i, A^\pm\right] \tag{A.15}$$

$$A^\pm = \pm x^\pm \alpha\left(x_\perp, \tau\right) \tag{A.16}$$

$$A^i = a^i_\perp\left(x_\perp, \tau\right) \tag{A.17}$$

$$\rightarrow F^{i\pm} = \partial^i\left(\pm x^\pm \alpha\right) - \partial^\pm \alpha^i_\perp - ig\left[\alpha^i_\perp, \pm x^\pm \alpha\right] \tag{A.18}$$

$$F^{i\pm} = \partial^i\left(\pm x^\pm \alpha\right) - g_{\pm\mp}\partial^\pm \alpha^i_\perp - ig\left[\alpha^i_\perp, \pm x^\pm \alpha\right] \tag{A.19}$$

$$\Rightarrow F^{i\pm} = \partial^i\left(\pm x^\pm \alpha\right) - \partial_\mp \alpha^i_\perp - ig\left[\alpha^i_\perp, \pm x^\pm \alpha\right] \tag{A.20}$$

Use the chain rule to expand into $\tau - \eta$ coordinates

$$F^{i\pm} = \pm x^\pm \partial^i \alpha - \tfrac{\partial\tau}{\partial x^\mp}\partial_\tau \alpha^i_\perp - ig\left[\alpha^i_\perp, \pm x^\pm \alpha\right] \tag{A.21}$$

$$\Rightarrow F^{i\pm} = \pm x^\pm\left(\partial^i \alpha - ig\left[\alpha^i_\perp, \alpha\right]\right) - \tfrac{\partial\tau}{\partial x^\mp}\partial_\tau \alpha^i_\perp \tag{A.22}$$

and remark that

$$\frac{\partial\tau}{\partial x^\mp} = \frac{\partial}{\partial x^\mp}\sqrt{2x^+x^-} = \frac{1}{2}\frac{2x^\pm}{\sqrt{2x^+x^-}} = \frac{x^\pm}{\tau} \tag{A.23}$$

which leaves us with equation 4.37, or

$$F^{i\pm} = -x^\pm\left(\mp\left[D^i, \alpha\right] + \frac{1}{\tau}\partial_\tau \alpha'_\perp\right) \tag{A.24}$$

For pure light-cone gauge fields and components, we have

$$F^{+-} = -F^{-+} = \partial^+ A^- - \partial^- A^+ - ig\left[A^+, A^-\right] = \partial^+ A^- - \partial^- A^+ \tag{A.25}$$

$$\left[A^+, A^-\right] = \left[x^+\alpha, -x^-\alpha\right] = -x^+x^-\left[\alpha, \alpha\right] = 0 \tag{A.26}$$

$$\Rightarrow F^{+-} = \partial^+\left(-x^-\alpha\right) - \partial^-\left(x^+\alpha\right) \tag{A.27}$$

$$= \tfrac{\partial\tau}{\partial x^-}\partial_\tau\left(-x^-\alpha\right) - \tfrac{\partial\tau}{\partial x^+}\partial_\tau\left(x^+\alpha\right) \tag{A.28}$$

$$= \tfrac{x^+}{\tau}\partial_\tau\left(-x^-\alpha\right) - \tfrac{x^-}{\tau}\partial_\tau\left(x^+\alpha\right) \tag{A.29}$$

$$= \tfrac{-x^-x^+}{\tau}\partial_\tau\alpha - \tfrac{x^+}{\tau}\tfrac{\tau}{x^+}\alpha - \tfrac{x^-x^+}{\tau}\partial_\tau\alpha - \tfrac{x^-}{\tau}\tfrac{\tau}{x^-}\alpha \tag{A.30}$$

$$= -2\tfrac{x^-x^+}{\tau}\partial_\tau\alpha - 2\alpha \tag{A.31}$$

$$= -\tfrac{1}{\tau}\partial_\tau\left(\tau^2\alpha\right) \tag{A.32}$$

where we have used the partial derivative relation between light-cone coordinates and $\tau - \eta$ coordinates.

Now, for the EOMs, we start with

$$\left[D_\mu, F^{\mu+}\right] = 0 \tag{A.33}$$

$$\partial_- F^{-+} - ig\left[A^+, F^{-+}\right] + \left[D_i, F^{i+}\right] = 0 \tag{A.34}$$

which, once converted to $\tau - \eta$ coordinates, becomes

$$\frac{\partial\tau}{\partial x^-}\partial_\tau\left(\frac{1}{\tau}\partial_\tau\left(\tau^2\alpha\right)\right) - ig\left[x^+\alpha, \frac{1}{\tau}\partial_\tau\left(\tau^2\alpha\right)\right] + \left[D_i, -x^+\left(-\left[D^i,\alpha\right] + \frac{1}{\tau}\partial_\tau\alpha^i_\perp\right)\right] = 0 \tag{A.35}$$

$$\frac{x^+}{\tau}\left\{\partial_\tau\left(\frac{1}{\tau}\partial_\tau\left(\tau^2\alpha\right)\right) - ig\left[\alpha, \partial_\tau\left(\tau^2\alpha\right)\right] + \tau\left[D_i, \left[D^i,\alpha\right]\right] - \left[D_i, \partial_\tau\alpha^i_\perp\right]\right\} = 0 \tag{A.36}$$

Dividing out the $\frac{x^+}{\tau}$ factor, carrying out the τ derivative in the second term and raising the index on the first covariant derivative in the third term,

$$\partial_\tau\left(\frac{1}{\tau}\partial_\tau\left(\tau^2\alpha\right)\right) - ig\tau^2\left[\alpha, \partial_\tau\alpha\right] - \tau\left[D^i, \left[D^i,\alpha\right]\right] - \left[D_i, \partial_\tau\alpha^i_\perp\right] = 0 \tag{A.37}$$

We can follow the same procedure in the x^- direction, and add and subtract these solutions as described in chapter 4. We are left with the last Classical Yang-Mills to solve:

$$\left[D_\mu, F^{\mu i}\right] = \left[D_+, F^{+i}\right] + \left[D_-, F^{-i}\right] + \left[D_j, F^{ji}\right] = 0 \tag{A.38}$$

Plug in the field strength components:

$$\begin{aligned}&\partial_+\left(x^+\left(-\left[D^i,\alpha\right] + \frac{1}{\tau}\partial_\tau\alpha^i_\perp\right)\right) - ig\left[-x^-\alpha, x^+\left(-\left[D^i,\alpha\right] + \frac{1}{\tau}\partial_\tau\alpha^i_\perp\right)\right] \\ &+\partial_-\left(x^-\left(\left[D^i,\alpha\right] + \frac{1}{\tau}\partial_\tau\alpha^i_\perp\right)\right) - ig\left[x^+\alpha, x^-\left(\left[D^i,\alpha\right] + \frac{1}{\tau}\partial_\tau\alpha^i_\perp\right)\right] + \left[D_j, F^{ji}\right] = 0\end{aligned} \tag{A.39}$$

Applying the derivatives:

$$
\begin{aligned}
&- \left[D^i, \alpha\right] + \frac{1}{\tau}\partial_\tau \alpha^i_\perp + x^+ \frac{\partial \tau}{\partial x^+}\partial_\tau \left(- \left[D^i, \alpha\right] + \frac{1}{\tau}\partial_\tau \alpha^i_\perp \right) \\
&- ig \left[-x^- \alpha, x^+ \left(- \left[D^i, \alpha\right] + \frac{1}{\tau}\partial_\tau \alpha^i_\perp \right) \right] \\
&+ \left[D^i, \alpha\right] + \frac{1}{\tau}\partial_\tau \alpha^i_\perp + x^- \frac{\partial \tau}{\partial x^-}\partial_\tau \left(\left[D^i, \alpha\right] + \frac{1}{\tau}\partial_\tau \alpha^i_\perp \right) \\
&- ig \left[x^+ \alpha, x^- \left(\left[D^i, \alpha\right] + \frac{1}{\tau}\partial_\tau \alpha^i_\perp \right) \right] - \left[D^j, F^{ji}\right] = 0
\end{aligned}
\tag{A.40}
$$

Which we can simplify to

$$
\frac{2}{\tau}\partial_\tau \alpha^i_\perp + 2\frac{x^+x^-}{\tau}\partial_\tau \left(\frac{1}{\tau}\partial_\tau \alpha^i_\perp \right) - 2igx^+x^- \left[\alpha, \left[D^i, \alpha\right]\right] - \left[D^j, F^{ji}\right] = 0 \tag{A.41}
$$

$$
\frac{2}{\tau}\partial_\tau \alpha^i_\perp + \tau\partial_\tau \left(\frac{1}{\tau}\partial_\tau \alpha^i_\perp \right) - ig\tau^2 \left[\alpha, \left[D^i, \alpha\right]\right] - \left[D^j, F^{ji}\right] = 0 \tag{A.42}
$$

$$
\Rightarrow \frac{1}{\tau}\partial_\tau \tau \partial_\tau \alpha^i_\perp - ig\tau^2 \left[\alpha, \left[D^i, \alpha\right]\right] - \left[D^j, F^{ji}\right] = 0 \tag{A.43}
$$

We now have derived the field strength tensor and EOMs of the classical Yang-Mills field in more detail than in chapter 4.

A.3 DETERMINING ROOTS

As outlined in section 7.1, the determination of the saturation scale is dependent upon finding the roots to

$$
f(r) = \frac{\pi^2}{2N_c} r^2 \alpha_s\left(\mu^2\right) xg\left(x, \mu^2\right) T(b) - \frac{1}{2} = 0 \tag{A.44}
$$

To do this, we use Brent's method, a root-finding algorithm that combines several simpler methods, namely the bisection model, secant method, and inverse quadratic interpolation. This provides quick and reliable solutions to our equations. In the case of our saturation scale, the root in r give the saturation scale, because $Q_s^2 = \frac{2}{r^2}$. In order to solve this problem, Brent's method begins with the bisection method to isolate the root. Taking an initial guess for r, to be the average squared gluon radius of the proton, $B_G = 4.0\text{GeV}^2$, and then searching for a place where the value of $f(r)$ changes sign, i.e.

$f(a)f(b) < 0$ for two points a and b, will allow us to utilize the bisection method. For a continuous function, a change in sign guarantees a root between the two points with differing signs, mirroring the intermediate value theorem. We will call the current guess b and the guess for which the sign changes a such that $[a, b]$ contains the solution, and require that $|f(b)| \leq |f(a)|$, meaning if this condition is not met, we swap a and b. Thus b is regarded as the better approximation and a third point, c, is initialized by setting $c = a$. Now that the solution is bracketed, we check at each iteration whether $f(b) = 0$ or $a - b < \delta$, where δ is the tolerance that we set for the solution. If either condition is satisfied, b is the approximate solution and the process is complete. Otherwise, the method determines a new trial point b' in the following way: If $f(a) \neq f(c)$ and $f(b) \neq f(c), b'$ is determined using inverse quadratic interpolation

$$b' = \frac{af(b)f(c)}{(f(a)-f(b))(f(a)-f(c))} + \frac{bf(a)f(c)}{(f(b)-f(a))(f(b)-f(c))} + \frac{cf(a)f(b)}{(f(c)-f(a))(f(c)-f(b))} \tag{A.45}$$

Otherwise, b' is determined by linear interpolation

$$b' = \frac{af(b)-bf(a)}{f(b)-f(a)} \tag{A.46}$$

The method maintains values of a, b, and c that satisfy the following conditions at each iteration:

- $b \neq c$
- $f(b)f(c) < 0$ such that the solution lies in the interval (a, c) if f is continuous
- $|f(b)| \leq f(c)$ such that b is a better approximate solution than c
- either $a \neq b$ and $a \neq c$, or $a = c$ and a and is the previous value of b

At this point, a relatively complicated set of conditions determines whether to proceed by bisection or interpolation. The method iterates until a zero is found or the procedure converges. Brent's method is robust, fast, and reliable, and allows us to accurately solve for our saturation scales.

A.4 SCALAR PRODUCT METHOD

There are various methods and definitions for calculating flow harmonics. The method employed for the plots shown in this thesis is known as the scalar product method and

is outlined briefly here. For a more in depth discussion see [38]. First defining the event flow as

$$Q_n = |Q_n| e^{in\psi_n} = \frac{1}{N} \sum_j e^{in\phi_j} \tag{A.47}$$

Then, as is done in the event plane method, one can define particles of interest as, for example, identified particles in a small p_T range and their corresponding flow vector as Q_n. Then v_n is determined by correlating the particles of interest to two different groups of particles, known as sub-events and denoted by A and B, in a wide p_T range with flow vectors Q_{nA}, and Q_{nB}, respectively. The expression is

$$v_n\{SP\} = \frac{\langle Q_n Q_{nA}^* \rangle}{\sqrt{\langle Q_{nA} Q_{nB}^* \rangle}} \tag{A.48}$$

where the name scalar product comes from this definition. This expression assumes that v_n does not fluctuate event to event, an assumption we know not to be true. In the case of of event-by-event fluctuations in v_n, event averages are taken in two steps: first averaging over events with the same v_n and then averaging over v_n bins. Doing so for equation (7.13) and using the following two definitions

$$\langle Q_n Q_{nA}^* \rangle_{|v_n} = \langle Q_n e^{-in\phi_n} \rangle_{|v_n} \langle Q_{nA} e^{-in\phi_n} \rangle_{|v_n}^* = v_n v_{nA} \tag{A.49}$$

$$\langle Q_{nA} Q_{nB}^* \rangle_{|v_n} = v_{nA}^2 \tag{A.50}$$

we can calculate the scalar product result for the fluctuating case,

$$v_n\{SP\} = \frac{\langle v_n v_{nA} \rangle_{v_n}}{\sqrt{\langle v_{nA}^2 \rangle_{v_n}}} = \sqrt{v_n^2} \tag{A.51}$$

The scalar product method does not include any experimental detector specific prop erties and thus allows for an easy comparison between theory and experiment.

B

RELEVANT QUANTITIES

This can serve as a quick refresher for the reader who has not seen or done calculations in field theories, and QCD in particular, in a long time.

B.1 ELEMENTS OF THE STRESS-ENERGY TENSOR ON THE LATTICE

Here, we explicitly add the various elements of the stress-energy tensor on the lattice which were omitted from section 6.3. Their derivations follow the a few differential equations which are solved iteratively on the lattice, and are quite tedious, yet intuitive.

$$
\begin{aligned}
T_i^{\tau x} = & \frac{1}{4\tau}\,\mathrm{Tr}\Big[-iE_i^y\Big(U_{y,i}U_{x,i+\hat{y}}U^\dagger_{y,i+\hat{x}}U^\dagger_{x,i} - U_{x,i}U_{y,i+\hat{x}}U^\dagger_{x,i+\hat{y}}U^\dagger_{y,i} \\
& -\frac{1}{N_c}\,\mathrm{trace} + U^\dagger_{x,i-\hat{x}}U_{y,i-\hat{x}}U_{x,i-\hat{x}+\hat{y}}U^\dagger_{y,i} - U_{y,i}U^\dagger_{x,i-\hat{x}+\hat{y}}U^\dagger_{y,i-\hat{x}}U_{x,i-\hat{x}} - \frac{1}{N_c}\,\mathrm{trace}\Big) \\
& - iE^y_{i+\hat{x}}\Big(U_{y,i+\hat{x}}U_{x,i+\hat{x}+\hat{y}}U^\dagger_{y,i+2\hat{x}}U^\dagger_{x,i+\hat{x}} - U_{x,i+\hat{x}}U_{y,i+2\hat{x}}U^\dagger_{x,i+\hat{x}+\hat{y}}U^\dagger_{y,i+\hat{x}} - \frac{1}{N_c}\,\mathrm{trace} \\
& + U^\dagger_{x,i}U_{y,i}U_{x,i+\hat{y}}U^\dagger_{y,i+\hat{x}} - U_{y,i+\hat{x}}U^\dagger_{x,i+\hat{y}}U^\dagger_{y,i}U_{x,i} - \frac{1}{N_c}\,\mathrm{trace}\Big) \\
& - \pi_i\Big(U_{x,i}\phi_{i+\hat{x}}U^\dagger_{x,i} - U^\dagger_{x,i-\hat{x}}\phi_{i-\hat{x}}U_{x,i-\hat{x}}\Big) \\
& - \pi_{i+\hat{y}}\Big(U_{x,i+\hat{y}}\phi_{i+\hat{x}+\hat{y}}U^\dagger_{x,i+\hat{y}} - U^\dagger_{x,i-\hat{x}+\hat{y}}\phi_{i-\hat{x}+\hat{y}}U_{x,i-\hat{x}+\hat{y}}\Big) \\
& - \pi_{i+\hat{x}}\Big(U_{x,i+\hat{x}}\phi_{i+2\hat{x}}U^\dagger_{x,i+\hat{x}} - U^\dagger_{x,i}\phi_i U_{x,i}\Big) \\
& - \pi_{i+\hat{x}+\hat{y}}\Big(U_{x,i+\hat{x}+\hat{y}}\phi_{i+2\hat{x}+\hat{y}}U^\dagger_{x,i+\hat{x}+\hat{y}} - U^\dagger_{x,i+\hat{y}}\phi_{i+\hat{y}}U_{x,i+\hat{y}}\Big)\Big]
\end{aligned}
\tag{B.1}
$$

$$
\begin{aligned}
T_i^{\tau y} =& \frac{1}{4\tau}\,\mathrm{Tr}\Big[-iE_i^x\Big(U_{x,i}U_{y,i+\hat{x}}U_{x,i+\hat{y}}^\dagger U_{y,i}^\dagger - U_{y,i}U_{x,i+\hat{y}}U_{y,i+\hat{x}}^\dagger U_{x,i}^\dagger - \frac{1}{N_c}\,\mathrm{trace} \\
&+U_{y,i-\hat{y}}^\dagger U_{x,i-\hat{y}}U_{y,i-\hat{y}+\hat{x}}U_{x,i}^\dagger - U_{x,i}U_{y,i-\hat{y}+\hat{x}}^\dagger U_{x,i-\hat{y}}^\dagger U_{y,i-\hat{y}} - \frac{1}{N_c}\,\mathrm{trace}\Big) \\
&- iE_{i+\hat{y}}^x\Big(U_{x,i+\hat{y}}U_{y,i+\hat{y}+\hat{x}}U_{x,i+2\hat{y}}^\dagger U_{y,i+\hat{y}}^\dagger - U_{y,i+\hat{y}}U_{x,i+2\hat{y}}U_{y,i+\hat{x}+\hat{y}}^\dagger U_{x,i+\hat{y}}^\dagger - \frac{1}{N_c}\,\mathrm{trace} \\
&+U_{y,i}^\dagger U_{x,i}U_{y,i+\hat{x}}U_{x,i+\hat{y}}^\dagger - U_{x,i+\hat{y}}U_{y,i+\hat{x}}^\dagger U_{x,i}^\dagger U_{y,i} - \frac{1}{N_c}\,\mathrm{trace}\Big) \\
&- \pi_i\Big(U_{y,i}\phi_{i+\hat{y}}U_{y,i}^\dagger - U_{y,i-\hat{y}}^\dagger\phi_{i-\hat{y}}U_{y,i-\hat{y}}\Big) \\
&- \pi_{i+\hat{x}}\Big(U_{y,i+\hat{x}}\phi_{i+\hat{x}+\hat{y}}U_{y,i+\hat{x}}^\dagger - U_{y,i-\hat{y}+\hat{x}}^\dagger\phi_{i-\hat{y}+\hat{x}}U_{y,i-\hat{y}+\hat{x}}\Big) \\
&- \pi_{i+\hat{y}}\Big(U_{y,i+\hat{y}}\phi_{i+2\hat{y}}U_{y,i+\hat{y}}^\dagger - U_{y,i}^\dagger\phi_i U_{y,i}\Big) \\
&- \pi_{i+\hat{x}+\hat{y}}\Big(U_{y,i+\hat{x}+\hat{y}}\phi_{i+2\hat{y}+\hat{x}}U_{y,i+\hat{x}+\hat{y}}^\dagger - U_{y,i+\hat{x}}^\dagger\phi_{i+\hat{x}}U_{y,i+\hat{x}}\Big)
\end{aligned}
\tag{B.2}
$$

$$
\begin{aligned}
T^{\tau\eta} =& \frac{g}{\tau^3}\,\mathrm{Tr}\Big[E_i^x\Big(U_{x,i}\phi_{i+\hat{x}}U_{x,i}^\dagger - \phi_i\Big) + E_{i+\hat{y}}^x\Big(U_{x,i+\hat{y}}\phi_{i+\hat{x}+\hat{y}}U_{x,i+\hat{y}}^\dagger - \phi_{i+\hat{y}}\Big) \\
&+E_i^y\Big(U_{y,i}\phi_{i+\hat{y}}U_{y,i}^\dagger - \phi_i\Big) + E_{i+\hat{x}}^y\Big(U_{y,i+\hat{x}}\phi_{i+\hat{x}+\hat{y}}U_{y,i+\hat{x}}^\dagger - \phi_{i+\hat{x}}\Big)\Big]
\end{aligned}
\tag{B.3}
$$

$$
\begin{aligned}
T_i^{xy} =& \frac{1}{2\tau^2}\,\mathrm{Tr}\Big[-g^2\Big(E_i^x + U_{y,i}E_{i+\hat{y}}U_{y,i}^\dagger\Big)\Big(E_i^y + U_{x,i}E_{i+\hat{x}}U_{x,i}^\dagger\Big) \\
&+\Big(U_{x,i}\phi_{i+x}U_{x,i}^\dagger - \phi_i\Big)\Big(U_{y,i}\phi_{i+y}U_{y,i}^\dagger - \phi_i\Big) \\
&+U_{y,i}\Big(U_{x,i+\hat{y}}\phi_{i+\hat{x}+\hat{y}}U_{x,i+\hat{y}}^\dagger - \phi_{i+\hat{y}}\Big)U_{y,i}^\dagger\Big(U_{y,i}\phi_{i+\hat{x}}U_{y,i}^\dagger - \phi_i\Big) \\
&+\Big(U_{x,i}\phi_{i+\hat{x}}U_{x,i}^\dagger - \phi_i\Big)U_{x,i}\Big(U_{y,i+\hat{x}}\phi_{i+\hat{x}+\hat{y}}U_{y,i+\hat{x}}^\dagger - \phi_{i+\hat{x}}\Big)U_{x,i}^\dagger \\
&+U_{y,i}\Big(U_{x,i+\hat{y}}\phi_{i+\hat{x}+\hat{y}}U_{x,i+\hat{y}}^\dagger - \phi_{i+\hat{y}}\Big)U_{y,i}^\dagger U_{x,i}\Big(U_{y,i+\hat{x}}\phi_{i+\hat{x}+\hat{y}}U_{y,i+\hat{x}}^\dagger - \phi_{i+\hat{x}}\Big)U_{x,i}^\dagger\Big]
\end{aligned}
\tag{B.4}
$$

$$
\begin{aligned}
T_i^{x\eta} =& -\frac{2}{\tau^2}\,\mathrm{Tr}\Big\{\frac{g}{4}\Big[E_i^x\Big(\pi_i + U_{x,i}\pi_{i+\hat{x}}U_{x,i}^\dagger\Big) + E_{i+\hat{y}}^x\Big(\pi_{i+\hat{y}} + U_{x,i+\hat{y}}\pi_{i+\hat{x}+\hat{y}}U_{x,i+\hat{y}}^\dagger\Big)\Big] \\
&+\frac{1}{8ig}\Big[\Big(U_{x,i}U_{y,i+\hat{x}}U_{x,i+\hat{y}}^\dagger U_{y,i}^\dagger - U_{y,i}U_{x,i+\hat{y}}U_{y,i+\hat{x}}^\dagger U_{x,i}^\dagger - \frac{1}{N_c}\,\mathrm{trace} \\
&+U_{y,i}U_{x,i-\hat{x}+\hat{y}}^\dagger U_{y,i-\hat{x}}^\dagger U_{x,i-\hat{x}} - U_{x,i-\hat{x}}^\dagger U_{y,i-\hat{x}}U_{x,i-\hat{x}+\hat{y}}U_{y,i}^\dagger - \frac{1}{N_c}\,\mathrm{trace}\Big)\Big(U_{y,i}\phi_{i+\hat{y}}U_{y,i}^\dagger - \phi_i\Big) \\
&+\Big(U_{y,i+\hat{x}}U_{x,i+\hat{y}}^\dagger U_{y,i}^\dagger U_{x,i} - U_{x,i}^\dagger U_{y,i}U_{x,i+\hat{y}}U_{y,i+\hat{x}}^\dagger - \frac{1}{N_c}\,\mathrm{trace} \\
&+U_{x,i+\hat{x}}U_{y,i+2\hat{x}}U_{y,i+\hat{x}+\hat{y}}^\dagger U_{x,i+\hat{x}}^\dagger - U_{y,i+\hat{x}}U_{y,i+\hat{x}+\hat{y}}U_{x,i+2\hat{x}}^\dagger U_{x,i+\hat{x}}^\dagger - \frac{1}{N_c}\,\mathrm{trace}\Big) \\
&\times\Big(U_{y,i+\hat{x}}\phi_{i+\hat{x}+\hat{y}}U_{y,i+\hat{x}}^\dagger - \phi_{i+\hat{x}}\Big)\Big]\Big\}
\end{aligned}
\tag{B.5}
$$

$$
\begin{aligned}
T_i^{y\eta} = -\frac{2}{\tau^2}\,\mathrm{Tr}\Big\{ & \frac{g}{4}\left[E_i^y\left(\pi_i + U_{y,i}\pi_{i+\hat{y}}U_{y,i}^\dagger\right) + E_{i+\hat{x}}^y\left(\pi_{i+\hat{x}} + U_{y,i+\hat{x}}\pi_{i+\hat{x}+\hat{y}}U_{y,i+\hat{x}}^\dagger\right)\right] \\
& + \frac{1}{8ig}\Bigg[\Bigg(U_{y,i}U_{x,i+\hat{y}}U_{y,i+\hat{x}}^\dagger U_{x,i}^\dagger - U_{x,i}U_{y,i+\hat{x}}U_{x,i+\hat{y}}^\dagger U_{y,i}^\dagger - \frac{1}{N_c}\,\mathrm{trace} \\
& + U_{x,i}U_{y,i+\hat{x}-\hat{y}}^\dagger U_{x,i-\hat{y}}^\dagger U_{y,i-\hat{y}} - U_{y,i-\hat{y}}^\dagger U_{x,i-\hat{y}}U_{y,i+\hat{x}-\hat{y}}U_{x,i}^\dagger - \frac{1}{N_c}\,\mathrm{trace}\Bigg)\left(U_{x,i}\phi_{i+\hat{x}}U_{x,i}^\dagger - \phi_i\right) \\
& + \Bigg(U_{x,i+\hat{y}}U_{y,i+\hat{x}}^\dagger U_{x,i}^\dagger U_{y,i} - U_{y,i}^\dagger U_{x,i}U_{y,i+\hat{x}}U_{x,i+\hat{y}}^\dagger - \frac{1}{N_c}\,\mathrm{trace} \\
& + U_{y,i+\hat{y}}U_{x,i+2\hat{y}}U_{y,i+\hat{x}+\hat{y}}^\dagger U_{x,i+\hat{y}}^\dagger - U_{x,i+\hat{y}}U_{y,i+\hat{x}+\hat{y}}U_{x,i+2\hat{y}}^\dagger U_{y,i+\hat{y}}^\dagger - \frac{1}{N_c}\,\mathrm{trace}\Bigg) \\
& \left(U_{x,i+\hat{y}}\phi_{i+\hat{x}+\hat{y}}U_{x,i+\hat{y}}^\dagger - \phi_{i+\hat{y}}\right) \qquad \Big\}
\end{aligned}
\tag{B.6}
$$

B.2 SU(3)

SU(3) stands for the group of 3×3 special unitary matrices generated by

$$
\left[T^a, T^b\right] = if^{abc}T^c \tag{B.7}
$$

where T^a are group elements of SU(3) and f^{abc} are SU(3) structure constants. The generators are normalized to obey

$$
\mathrm{Tr}\left[T^aT^b\right] = \tfrac{1}{2}\delta_{ab} \tag{B.8}
$$

The number of generators for SU(3) is $3^2 - 1 = 8$, which, in physics corresponds to the 3 distinct colour charges. The SU(3) in nuclear physics are sometimes called the Gell-Mann matrices, and their normalization condition is

$$
\mathrm{Tr}\left[t^at^b\right] = 2\delta_{ab} \tag{B.9}
$$

B.3 GAMMA MATRICES

The gamma matrices γ^μ act on spinors and come in a variety of representations. Their defining feature is the Clifford algebra that they obey, namely the anti-commutation relation

$$\{\gamma^\mu, \gamma^\nu\} = 2\eta^{\mu\nu} \tag{B.10}$$

where $\mu, \nu = 0, 1, 2, 3$. The simplest representation of the gamma (Dirac) matrices are 4×4 matrices, meaning there is no such representation in 3×3 or smaller matrices. We generally use

$$\gamma^0 = \begin{pmatrix} 0 & 1 \\ 1 & 0 \end{pmatrix} \tag{B.11}$$

$$\gamma^0 = \begin{pmatrix} 0 & \sigma^i \\ -\sigma^i & 0 \end{pmatrix} \tag{B.12}$$

where σ^i are the Pauli matrices.

BIBLIOGRAPHY

[1] Henri Kowalski and Derek Teaney. "Impact parameter dipole saturation model." In: *Physical Review D* 68.11 (2003). ISSN: 1089-4918. DOI: 10.1103/physrevd.68.114005. URL: http://dx.doi.org/10.1103/PhysRevD.68.114005.

[2] Bjrn Schenke, Prithwish Tribedy, and Raju Venugopalan. "Initial-state geometry and fluctuations in Au + Au, Cu + Au, and U + U collisions at energies available at the BNL Relativistic Heavy Ion Collider." In: *Phys. Rev. C* 89 (6 2014), p. 064908. DOI: 10.1103/PhysRevC.89.064908. URL: https://link.aps.org/doi/10.1103/PhysRevC.89.064908.

[3] L. Adamczyk, J.K. Adkins, G. Agakishiev, M.M. Aggarwal, Z. Ahammed, I. Alekseev, J. Alford, A. Aparin, D. Arkhipkin, and E.C. et al. Aschenauer. "Azimuthal Anisotropy inU+U and Au+AuCollisions at RHIC." In: *Physical Review Letters* 115.22 (2015). ISSN: 1079-7114. DOI: 10.1103/physrevlett.115.222301. URL: http://dx.doi.org/10.1103/PhysRevLett.115.222301.

[4] V. Khachatryan et al. "Measurement of the inclusive 3-jet production differential cross section in proton–proton collisions at 7 TeV and determination of the strong coupling constant in the TeV range." In: *The European Physical Journal C* 75.5 (2015), p. 186.

[5] Débora P. Menezes. "Modelling Hadronic Matter." In: *Journal of Physics: Conference Series* 706.3 (2016), p. 032001.

[6] Jonah Bernhard, J. Moreland, and Steffen Bass. "Bayesian estimation of the specific shear and bulk viscosity of quark?gluon plasma." In: *Nature Physics* 15 (Nov. 2019). DOI: 10.1038/s41567-019-0611-8.

[7] Raimond Snellings. "Elliptic flow: a brief review." In: *New Journal of Physics* 13.5 (2011), p. 055008. ISSN: 1367-2630. DOI: 10.1088/1367-2630/13/5/055008. URL: http://dx.doi.org/10.1088/1367-2630/13/5/055008.

[8] Bjrn Schenke, Sangyong Jeon, and Charles Gale. "(3+1)D hydrodynamic simulation of relativistic heavy-ion collisions." In: *Physical Review C* 82.1 (2010). ISSN: 1089-490X. DOI: 10.1103/physrevc.82.014903. URL: http://dx.doi.org/10.1103/PhysRevC.82.014903.

[9] S Bass. "Microscopic models for ultrarelativistic heavy ion collisions." In: *Progress in Particle and Nuclear Physics* 41 (1998), 255?369. ISSN: 0146-6410. DOI: 10.1016/s0146-6410(98)00058-1. URL: http://dx.doi.org/10.1016/S0146-6410(98)00058-1.

[10] Frans Gelis. "COLOR GLASS CONDENSATE AND GLASMA." In: *International Journal of Modern Physics A* 28.01 (2013), p. 1330001. ISSN: 1793-656X. DOI: 10.1142/s0217751x13300019. URL: http://dx.doi.org/10.1142/S0217751X13300019.

[11] Maciej Rybczy?ski and Wojciech Broniowski. "Wounded-nucleon model with realistic nucleon-nucleon collision profile and observables in relativistic heavy-ion collisions." In: *Physical Review C* 84.6 (2011). ISSN: 1089-490X. DOI: 10.1103/physrevc.84.064913. URL: http://dx.doi.org/10.1103/PhysRevC.84.064913.

[12] Larry McLerran and Raju Venugopalan. "Computing quark and gluon distribution functions for very large nuclei." In: *Physical Review D* 49.5 (1994), 2233?2241. ISSN: 0556-2821. DOI: 10.1103/physrevd.49.2233. URL: http://dx.doi.org/10.1103/PhysRevD.49.2233.

[13] Bjrn Schenke, Prithwish Tribedy, and Raju Venugopalan. "Fluctuating Glasma Initial Conditions and Flow in Heavy Ion Collisions." In: *Physical Review Letters* 108.25 (2012). ISSN: 1079-7114. DOI: 10.1103/physrevlett.108.252301. URL: http://dx.doi.org/10.1103/PhysRevLett.108.252301.

[14] Bjrn Schenke, Prithwish Tribedy, and Raju Venugopalan. "Event-by-event gluon multiplicity, energy density, and eccentricities in ultrarelativistic heavy-ion collisions." In: *Physical Review C* 86.3 (2012). ISSN: 1089-490X. DOI: 10.1103/physrevc.86.034908. URL: http://dx.doi.org/10.1103/PhysRevC.86.034908.

[15] Francois Gelis, Edmond Iancu, Jamal Jalilian-Marian, and Raju Venugopalan. "The Color Glass Condensate." In: *Annual Review of Nuclear and Particle Science* 60.1

(2010), 463?489. ISSN: 1545-4134. DOI: 10.1146/annurev.nucl.010909.083629. URL: http://dx.doi.org/10.1146/annurev.nucl.010909.083629.

[16] Edmond Iancu and Raju Venugopalan. "THE COLOR GLASS CONDENSATE AND HIGH ENERGY SCATTERING IN QCD." In: *Quark?Gluon Plasma 3* (2004), 249?363. DOI: 10.1142/9789812795533_0005. URL: http://dx.doi.org/10.1142/9789812795533_0005.

[17] Edmond Iancu, Andrei Leonidov, and Larry McLerran. "The Colour Glass Condensate: An Introduction." In: *QCD Perspectives on Hot and Dense Matter* (2002), 73?145. DOI: 10.1007/978-94-010-0267-7_3. URL: http://dx.doi.org/10.1007/978-94-010-0267-7_3.

[18] Alex Krasnitz, Yasushi Nara, and Raju Venugopalan. "Gluon production in the Color Glass Condensate model of collisions of ultrarelativistic finite nuclei." In: *Nuclear Physics A* 717.3-4 (2003), 268?290. ISSN: 0375-9474. DOI: 10.1016/s0375-9474(03)00636-5. URL: http://dx.doi.org/10.1016/S0375-9474(03)00636-5.

[19] Jamal Jalilian-Marian, Alex Kovner, Larry McLerran, and Heribert Weigert. "Intrinsic glue distribution at very smallx." In: *Physical Review D* 55.9 (1997), 5414?5428. ISSN: 1089-4918. DOI: 10.1103/physrevd.55.5414. URL: http://dx.doi.org/10.1103/PhysRevD.55.5414.

[20] Alex Kovner, Larry McLerran, and Heribert Weigert. "Gluon production from non-Abelian Weizser-Williams fields in nucleus-nucleus collisions." In: *Physical Review D* 52.11 (1995), 6231?6237. ISSN: 0556-2821. DOI: 10.1103/physrevd.52.6231. URL: http://dx.doi.org/10.1103/PhysRevD.52.6231.

[21] Paul Romatschke and Raju Venugopalan. "The unstable glasma." In: *Physical Review D* 74.4 (2006). ISSN: 1550-2368. DOI: 10.1103/physrevd.74.045011. URL: http://dx.doi.org/10.1103/PhysRevD.74.045011.

[22] Daniel N. Blaschke, Frans Gieres, Ml Reboud, and Manfred Schweda. "The energy?momentum tensor(s) in classical gauge theories." In: *Nuclear Physics B* 912 (2016), 192?223. ISSN: 0550-3213. DOI: 10.1016/j.nuclphysb.2016.07.001. URL: http://dx.doi.org/10.1016/j.nuclphysb.2016.07.001.

[23] Alex Krasnitz and Raju Venugopalan. "Non-perturbative computation of gluon mini-jet production in nuclear collisions at very high energies." In: *Nuclear Physics B* 557.1-2 (1999), 237?270. ISSN: 0550-3213. DOI: 10.1016/s0550-3213(99)00366-1. URL: http://dx.doi.org/10.1016/S0550-3213(99)00366-1.

[24] Kenji Fukushima and Frans Gelis. "The evolving Glasma." In: *Nuclear Physics A* 874 (2012), 108?129. ISSN: 0375-9474. DOI: 10.1016/j.nuclphysa.2011.11.003. URL: http://dx.doi.org/10.1016/j.nuclphysa.2011.11.003.

[25] T. Lappi. "Production of gluons in the classical field model for heavy ion collisions." In: *Physical Review C* 67.5 (2003). ISSN: 1089-490X. DOI: 10.1103/physrevc.67.054903. URL: http://dx.doi.org/10.1103/PhysRevC.67.054903.

[26] T. Lappi. "Energy density of the glasma." In: *Physics Letters B* 643.1 (2006), 11?16. ISSN: 0370-2693. DOI: 10.1016/j.physletb.2006.10.017. URL: http://dx.doi.org/10.1016/j.physletb.2006.10.017.

[27] M. Cautun. *Photon production in the Color Glass Condensate formalism*. MSc. Thesis, McGill University. 2009.

[28] V. Khachatryan et al. "Transverse-Momentum and Pseudorapidity Distributions of Charged Hadrons inppCollisions ats=7??TeV." In: *Physical Review Letters* 105.2 (2010). ISSN: 1079-7114. DOI: 10.1103/physrevlett.105.022002. URL: http://dx.doi.org/10.1103/PhysRevLett.105.022002.

[29] Guido Altarelli and G. Parisi. "Asymptotic Freedom in Parton Language." In: *Nucl. Phys. B* 126 (1977), pp. 298–318. DOI: 10.1016/0550-3213(77)90384-4.

[30] Yuri L. Dokshitzer. "Calculation of the Structure Functions for Deep Inelastic Scattering and e+ e- Annihilation by Perturbation Theory in Quantum Chromodynamics." In: *Sov. Phys. JETP* 46 (1977), pp. 641–653.

[31] Bjrn Schenke, Prithwish Tribedy, and Raju Venugopalan. "Multiplicity distributions inp+p,p+A, andA+Acollisions from Yang-Mills dynamics." In: *Physical Review C* 89.2 (2014). ISSN: 1089-490X. DOI: 10.1103/physrevc.89.024901. URL: http://dx.doi.org/10.1103/PhysRevC.89.024901.

[32] J. L. Nagle and W. A. Zajc. "Assessing saturation physics explanations of collectivity in small collision systems with the ip-jazma model." In: *Physical Review C* 99.5 (2019). ISSN: 2469-9993. DOI: 10.1103/physrevc.99.054908. URL: http://dx.doi.org/10.1103/PhysRevC.99.054908.

[33] Paul Romatschke and Ulrike Romatschke. *Relativistic Fluid Dynamics In and Out of Equilibrium – Ten Years of Progress in Theory and Numerical Simulations of Nuclear Collisions*. 2017. arXiv: 1712.05815 [nucl-th].

[34] Scott McDonald. *The Initial State of Heavy Ion Collisions in the IP-Glasma Framework*. MSc. Thesis, McGill University. 2016.

[35] M. Alvioli, H.J. Drescher, and M. Strikman. "A Monte Carlo generator of nucleon configurations in complex nuclei including nucleon–nucleon correlations." In: *Physics Letters B* 680.3 (2009), pp. 225 –230. ISSN: 0370-2693. DOI: https://doi.org/10.1016/j.physletb.2009.08.067. URL: http://www.sciencedirect.com/science/article/pii/S0370269309010442.

[36] H De Vries, C W De Jager, and C De Vries. "Nuclear charge-density-distribution parameters from elastic electron scattering." In: *At. Data Nucl. Data Tables; (United States)* (). DOI: 10.1016/0092-640X(87)90013-1.

[37] J. Noronha-Hostler, N. Paladino, S. Rao, Matthew D. Sievert, and Douglas E. Wertepny. *Ultracentral Collisions of Small and Deformed Systems at RHIC: UU, dAu, ^{9}BeAu, ^{9}Be^{9}Be, ^{3}He^{3}He, and ^{3}HeAu Collisions*. 2019. arXiv: 1905.13323 [hep-ph].

[38] C. Adler et al. "Elliptic flow from two- and four-particle correlations in Au+Au collisions atsNN=130GeV." In: *Physical Review C* 66.3 (2002). ISSN: 1089-490X. DOI: 10.1103/physrevc.66.034904. URL: http://dx.doi.org/10.1103/PhysRevC.66.034904.

[39] J.J. Sakurai and J. Napolitano. *Modern Quantum Mechanics*. Addison-Wesley, 2011.

[40] L.D. Landau and E.M. Lifshitz. *Fluid Mechanics*. v. 6. Elsevier Science, 2013.

[41] J. I. Kapusta and Charles Gale. *Finite-temperature field theory: Principles and applications*. Cambridge University Press, 2011.

[42] Sangyong Jeon. *Personal communications*.

[43] Michael E Peskin and Daniel V Schroeder. *An introduction to quantum field theory*. Includes exercises. Boulder, CO: Westview, 1995.

[44] Aleksey Cherman, Thomas D. Cohen, and Paul M. Hohler. "A sticky business: the status of the conjectured viscosity/entropy density bound." In: *Journal of High Energy Physics* 2008.02 (2008), p. 026.

[45] Charles Gale, Sangyong Jeon, Bjrn Schenke, Prithwish Tribedy, and Raju Venugopalan. "Initial state fluctuations and higher harmonic flow in heavy-ion collisions." In: *Nuclear Physics A* 904-905 (2013), 409c?412c. ISSN: 0375-9474. DOI: 10.1016/j.nuclphysa.2013.02.037. URL: http://dx.doi.org/10.1016/j.nuclphysa.2013.02.037.

[46] In: *Special Relativity and Its Experimental Foundation* (1997), 21?49. ISSN: 1793-1495. DOI: 10.1142/9789814261036_0002. URL: http://dx.doi.org/10.1142/9789814261036_0002.

[47] Michael L. Miller, Klaus Reygers, Stephen J. Sanders, and Peter Steinberg. "Glauber Modeling in High-Energy Nuclear Collisions." In: *Annual Review of Nuclear and Particle Science* 57.1 (2007), 205?243. ISSN: 1545-4134. DOI: 10.1146/annurev.nucl.57.090506.123020. URL: http://dx.doi.org/10.1146/annurev.nucl.57.090506.123020.

[48] F. Antinori and U.A. Wiedemann. "Heavy-ion collisions—Selected topics." In: *Proc. Int. Sch. Phys. Fermi* 178 (2011). Ed. by A. Bracco and E. Nappi, pp. 229–277. DOI: 10.3254/978-1-60750-974-5-229.

[49] Wit Busza, Krishna Rajagopal, and Wilke van der Schee. "Heavy Ion Collisions: The Big Picture and the Big Questions." In: *Annual Review of Nuclear and Particle Science* 68.1 (2018), 339?376. ISSN: 1545-4134. DOI: 10.1146/annurev-nucl-101917-020852. URL: http://dx.doi.org/10.1146/annurev-nucl-101917-020852.

[50] A Chaudhuri. "A Short Course on Relativistic Heavy Ion Collisions." In: (2014). DOI: 10.1088/978-0-750-31060-4. URL: http://dx.doi.org/10.1088/978-0-750-31060-4.

[51] Sangyong Jeon and Ulrich Heinz. "Introduction to hydrodynamics." In: *International Journal of Modern Physics E* 24.10 (2015), p. 1530010. ISSN: 1793-6608. DOI: 10.1142/s0218301315300106. URL: http://dx.doi.org/10.1142/S0218301315300106.

[52] S. Ryu, J.-F. Paquet, C. Shen, G.?S. Denicol, B. Schenke, S. Jeon, and C. Gale. "Importance of the Bulk Viscosity of QCD in Ultrarelativistic Heavy-Ion Collisions." In: *Physical Review Letters* 115.13 (2015). ISSN: 1079-7114. DOI: 10.1103/physrevlett.115.132301. URL: http://dx.doi.org/10.1103/PhysRevLett.115.132301.